DEVELOPMENT OF INEXPENSIVE HIGH TEMPERATURE NITI-BASED SHAPE MEMORY ALLOYS FOR POWDER BED ADDITIVE MANUFACTURING

A Dissertation

by

TAYLER WADE SUNDERMANN

Submitted to the Graduate and Professional School of
Texas A&M University
in fulfillment of the requirements for the degree of

DOCTOR OF PHILOSOPHY

Chair of Committee,	Ibrahim Karaman
Committee Members,	Raymundo Arroyave
	Alaa Elwany
	Kelvin Xie
Head of Department,	Ibrahim Karaman

August 2025

Major Subject: Materials Science and Engineering

UUR 11/2025 NSC-614-7507

ABSTRACT

NiTi and NiTi-based Shape Memory Alloys (SMA) exhibit a reversible solid-state phase transformation from martensite to austenite driven by thermal energy. High temperature (M_f>100°C) SMAs are martensite at room temperature and can be fabricated into solid-state actuators that return to a pre-programmed shape against a designed load after heating to transformation threshold. Reactive as-fabricated additively manufactured parts (4-D printing) is the current state of the art in manufacturing of SMAs but requires compositions compliant to rapid solidification. Existing actuator designs are developed from commercially available, highly investigated material compositions. However, existing high temperature high performance (high actuation strain, low thermal hysteresis) shape memory alloys contain significant (>10% at.) portions of high-cost Platinum Group Metals (PGMs). It is of significant scientific interest to investigate material compositions that are peer performing or superior to PGMs whose constituent elements represent a significant cost savings. Shape memory alloy properties vary significantly with small (0.1% at.) compositional changes making robust investigative sample sets very large. Computational material design can be deployed to shrink the compositional space of possible alloy combinations and reduce the experimental load in material discovery. Investigating shape memory effect (SME) and validating process additive process parameters for a single novel composition is cost intensive in both time and consumed materials. Additionally, sub-optimal processing, oxygen, or solidification rate sensitivity could render additively manufacturing specimens without micro, macro cracks, or significant chemical variance impossible. Unfortunately, such failure susceptibility cannot be simulated. Therefore, a research pathway to validate novel shape memory alloy compositions for powder bed fusion additive

manufacturing without the need for powdered feedstock is also proposed. This research investigates novel high temperature shape memory alloys for actuators without platinum group alloying elements to discover one that could be commercially viable as an additive manufacturing feedstock.

CONTRIBUTORS AND FUNDING SOURCES

Contributors

This work was supervised by a dissertation committee consisting of Professor Ibrahim Karaman as advisor, Professor Raymundo Arroyave of the Department of Materials Science and Engineering, Professor Kelvin Xie of the Department of Materials Science and Engineering, and Professor Alaa Elwany of the Department of Industrial Engineering with appointment in the Department of Materials Science and Engineering.

The shape memory alloy database used to develop a machine learning model for this investigation is the property of Dr. Ibrahim Karaman's research group initially developed by previous student Dr. William Trehern, PhD with data collection and maintenance currently performed by current PhD student John Broucek. The neural network-based machine learning model utilized for investigation was modified from Dr. William Trehern's AIMS model and coded by John Broucek. Iteration 1 materials were also fabricated with significant assistance from John Broucek while the authoring student was learning the experimental processes.

Splat quenching was completed by Dr. Jacob Williamson, PhD at the University of Alabama and the resulting splat quench sample analysis as analog for additive manufacturing is heavily informed from his and Dr. Luke Brewer's group's published work.

The work on L-PBF printability maps of shape memory alloys was completed by Sofia Sheikh, aspiring PhD student from Dr. Raymundo Arroyave's group in the department of materials engineering.

Mechanical processing was assisted by Mike Elverud, Robert Barber, and Adam Long.

UUR 11/2025 NSC-614-7507

All other work conducted for the dissertation was completed by the student independently.

Funding Sources

This work is funded by the Department of Energy's Kansas City National Security Campus, operated by Honeywell Federal Manufacturing & Technologies, LLC, under contract number DE-NA0002839. Its contents are solely the responsibility of the authors and do not represent the official views of the Kansas City National Security Campus. Graduate study was supported by research and teaching assistantship appointments from Texas A&M University as part of Dr. Ibrahim Karaman's MESAM Research Group.

NOMENCLATURE

Acronym	Description
AM	Additive Manufacturing
EDS	Energy-dispersive Spectroscopy
EDM	Electo-Discharge Machining, here, wire EDM for machining
DSC	Differential Scanning Calorimetry
A_s	Martensite to Austenite Transformation Start Temperature
A_f	Martensite to Austenite Transformation Finish Temperature
M_s	Austenite to Martensite Transformation Start Temperature
M_f	Austenite to Martensite Transformation Finish Temperature
ΔT	Transformation Temperature Thermal Hysteresis (A_f - M_s)
ΔH	Transformation Enthalpy
L-PBF	Laser Powder Bed Fusion
EB-PBF	Electron Beam Powder Bed Fusion
SMA	Shape Memory Alloy
SME	Shape Memory Effect
PGM	Platinum Group Metal
HTSMA	High Temperature Shape Memory Alloy
ML	Machine Learning
DNN	Deep Neural Network
e_{LCT}	Strain at Lower Cycle Temperature Strain, $M_f - 50°C$
e_{UCT}	Strain at Upper Cycle Temperature, $A_f + 100°C$

ε_{irr}	Irrecoverable strain
ε_{rec}	Recovered transformation strain
ε_{tot}	Total strain
SHT	Secondary Heat Treat/Solution Heat Treat (context)
WQ	Water Quenched (23°C)
IQ	Ice (water) Quenched (0°C)
SEM	Scanning Electron Microscope
SE	Secondary Electron analysis
BSE	Backscattered Electron analysis
XRD	X-ray Diffraction

TABLE OF CONTENTS

Page

LIST OF FIGURES

Page

LIST OF TABLES

Page

CHAPTER I

INTRODUCTION

This section includes the story of how this research was formulated, speaking to the specific fiscal year deliverables from the sponsors, the expected challenges to overcome, and the evolution of research direction as cost became an impediment to the original research pathways. The motivation and objectives are laid out as they exist at the time of writing of this dissertation followed by a literature review to clarify the state of the art of relevant technical disciplines. All discussion of application or future direction is purely speculation and does not represent any ideas, expressions, or research interests of the Kansas City National Security Campus.

Motivation and Objectives

SMA actuators represent an extremely lightweight solution to passive actuation, however, their application is limited by the ability to design to leverage the shape memory effect, and the temperature range during which the transformation occurs [6, 12]. Currently, commercial applications of SMA systems are mechanically designed around a known material with known transformation temperatures. While the sponsors do not have an application for such a device currently, if a process could be developed to create tailored SMA compositions for a specific temperature range which could also be fabricated via additive manufacturing, tailored lightweight actuators could be manufactured on-demand for a range of application uses. This would open the possibility for any of the shape memory effects leveraged in design now to be used at any arbitrary

temperature: control surfaces [13, 14], psuedoelastic wires[15, 16], single use couplers [17], compression textiles [18], or interlocking metasurfaces [19]. For KCNSC, an arbitrary high temperature transformation range of 200°C to 300°C was set with an interest in maximizing the shape memory effect within range. Historically SMAs have been restricted in their application design by the relatively limited ways to fabricate the material for useful work, e.g. drawing as wire or extruding into tubes, foils, or honeycombs[12, 18, 20-23]. Relatively high work output, low irrecoverable stain, and low hysteresis above 200°C has only been shown in materials with a high chemical fraction of high-cost platinum group metals (PGM) Pt, Pd, Au, etc. Given the previous as motivation, and constrained to not use PGMs, answering the following questions were the original goals of this investigation:

∴ Can novel shape memory alloy compositions that transform within a pre-specified range (200°C-300°C) be investigated rapidly, with a high degree of confidence, and repeatably?

∴ Do compositions that transform within that temperature range have desirable functional and mechanical properties?

∴ Can a developed composition with high useful work, that transforms within a specific temperature range, that also has a usefully low hysteresis be fabricated by additive manufacturing?

∴ How does an additively manufactured shape memory alloy actuator compare to one conventionally fabricated?

During the second year of the research investigation while determining a powder atomization supplier it was discovered that cost would be a significant obstacle in the development process. Outside of multiple near equiatomic NiTi compositions, shape memory alloy compositions are not available as commercial off the powders for additive manufacturing. One exception may be the highly investigated $Ni_{50.3}Ti_{29.7}Hf_{20}$ however it transforms below the area of interest for this work. Powders can be manufactured via gas atomization but require an initial high purity (<100ppm O_2) SMA ingot (vacuum induction or vacuum arc melted) with a mass large enough to accept the ~50 wt.% process loss while retaining enough material to test for HSE compliance and then complete a sweep of experimentation. The single composition estimated 10kg of powder needed for an investigation was quoted at $110k-$130k USD and the funding call was rejected by the sponsor. The significant cost was unfeasible for the sponsoring organization and the investigation was altered to instead validate multiple high performing alloys via rapid solidification analogs.

The refined research objectives are as follows:

1. Predict the shape memory effect of a compositional space and pre-select high potential alloys to reduce the experimental load.
2. Fabricate modeled alloys and test mechanical performance.
3. Down-select alloys of interest based on pareto front of hysteresis and recoverable strain, constrained by transformation range (loosened to 175°C-325°C).
4. Determine viability of down-selected alloys for additive manufacturing without the need for atomized powder due to excessive cost.

Background

SMA Fundamentals

Shape memory alloys (SMA) represent a subset of shape memory materials, that is, materials that react to certain stimuli to return to a previous form; different than heating a pipe under thermal expansion, an SMA spring would re-coil itself, even against a downward load, while being heated [6]. The most commercially viable SMAs have been developed from NiTi or Nitinol (NiTi Naval Ordanance Laboratory) which does not suffer from the same instability and brittleness that plagues other shape memory materials like Fe-Mn-Si, Cu-Zn-Al, or Cu-Al-Ni systems [24, 25]. In the most basic sense, the unique properties of SMAs are due to their solid-state transformation between crystal structures. NiTi SMAs can exist in monoclinic martensite (detwinned or twinned) and cubic austenite phases. They can transform between phases with combinations of thermal and mechanical energy. Figure 1 shows progression of an SMA that is in martensite at room temperature and one possible progress of shape memory effect. Starting at 0,0,0, a mechanical load is applied the twinned/self-accommodated martensite phase. The mechanical energy drives a structural change from twinned martensite to detwinned martensite. If the load is released, it will stay strained as a detwinned martensite. However, upon heating, the detwinned martensite will transform to austenite above Austenite Start temperature (As) and be completely transformed above the Austenite Finish temperature (Af). Start and finish temperatures are functions of the

overheating or undercooling required to overcome the transformational barrier of the phase change. If the thermal energy is removed, the material will revert to the originally

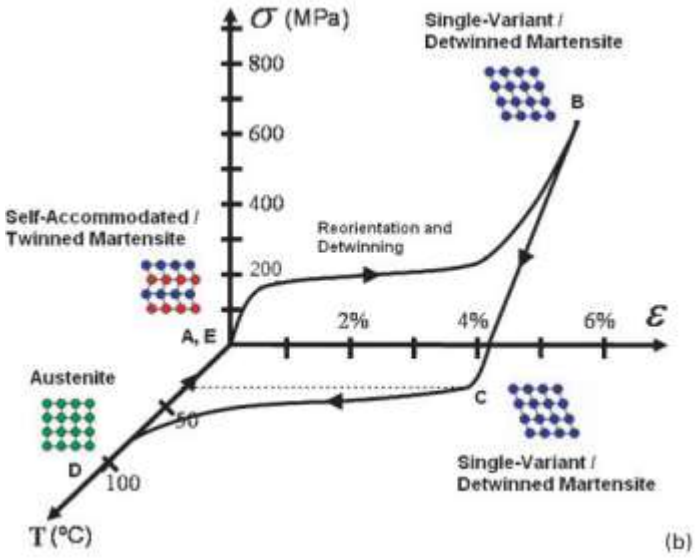

Figure 1: Shape memory effect of mechanically manipulated twinned martensite from [1]

self-accommodated/twinned martensite, fully recovering all strain from the load. This recovery is called one-way shape memory effect.

If an SMA started in the austenite phase, that is, room temperature (or testing temperature) was above A_f then the mechanical load can cause the austenite to transform into self-accommodating martensite before detwinning the martensite. The mechanical load causing transformation enables recovery of large amounts of strain, this is called pseudoplasticity. Nearly all commercially viable products designed with SMAs in mind take advantage of one or of these shape memory effects.

One highly investigated use case for shape memory alloys are actuator systems by utilizing the one-way shape memory effect. When a martensite part is stressed to a certain level, heating it past transformation will cause the SMA to recover some or all

the resulting strain, even against a constantly held stress. SMA actuator systems are extremely lightweight and simple compared to electronic or hydraulic systems, though do not have a high cycle to failure rate, and thermal activation is slower than electronic or fluid actuation. Table 1 compares some actuator systems.

Table 1: Various actuator systems compared to SMA actuator [24]

Actuator Type	Stress (MPa)	Strain (%)	Efficiency (%)	Bandwidth (Hz)	Work per Volume (J/cm^3)	Power per Volume (W/cm^3)
NiTi SMA	200	10	3	3	10	30
Piezoceramic	35	0.2	50	5000	0.035	175
Single crystal piezoelectric	300	1.7	90	5800	2.55	15,000
Human muscle	.007-0.8	1-100	35	2-173	0.035	0.35
Hydraulic	20	50	80	4	5	20
Pneumatic	0.7	50	90	20	0.175	3.5

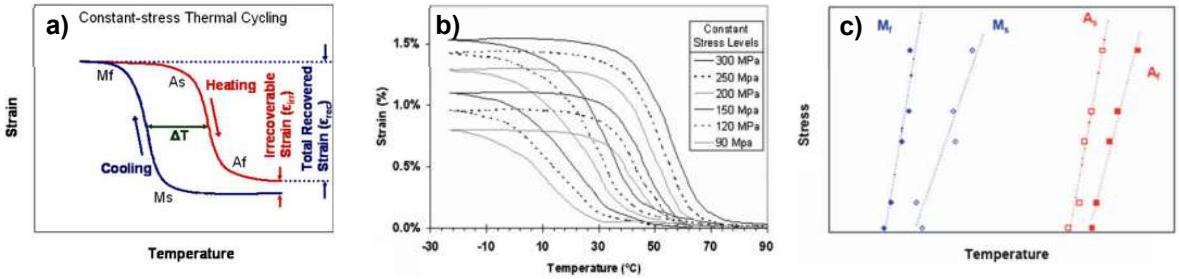

Figure 2: a) Single thermal cycle load noting recoverable and irrecoverable strains, **b)** an IBHC, and **c)** resulting temperature transformation dependence diagram [1, 5]

Measurement of shape memory effects depends heavily on the shape memory effect that is of interest in the part design. For actuation scenarios, the most important values are transformation temperatures and thermal cycling testing. In thermal cycling, ΔT or hysteresis (As-Mf), is a measurement of the distance between activation cycles, for an actuator it represents cycle efficiency and should be minimized as shown in **Fig. 2a.** along with a multiple cycle constant stress load, **Fig. 2b.** which can be used to determine work capacity or temperature transformation curves, **Fig. 2c.** While transformation temperatures can be determined by multiple testing methods them most common is Differential Scanning Calorimetry (DSC) where the thermodynamic energy required used to drive the solid-state phase transformations can be measured and analyzed as heat flow. Transformation temperatures are frequently reported simply as martensitic start (Ms) and finish (Mf) as well as austenite start (As) and finish (Af) temperatures, assuming there are no additional phases. Other values of interest may be the enthalpies

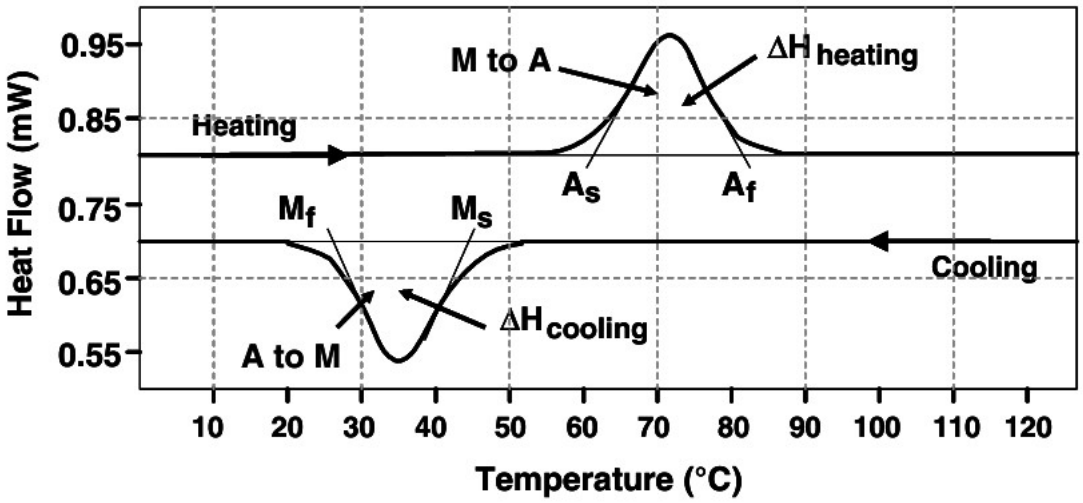

Figure 3: Schematic of a DSC curve for a low temperature SMA showing the transformation temperatures and the associated latent heat of transformation during heating and cooling, from [6].

of transformation, intermediate phase transformations, or peak temperatures of phases. A DSC curve like the one visible in Figure 3 and has become ubiquitous in SMAs for its speed and accuracy compared to other test methodologies.

For a continued fundamental understanding of SMA systems readers are referred to Ma et. al. for high temperature SMAs, Jani et. al. for a broad overview, Otsuka et. al. for mechanisms, and Lagoudas for applications [1, 6, 24, 26].

NiTi(+) Mechanical Performance

NiTi Transformation Mechanism

For a single grain within a polycrystalline material, shear distortion occurs along the habit plane, which is the specific plane that is the interface of the martensite and austenite phases. The habit plane is invariant to motion during the transformation. The transformation from austenite to martensite (lattice invariant shear) occurs via slip or by twinning. Atomically, slip occurs when one atom moves one or more atomic space, and twinning occurs by moving a fractional space. Recalling the macro-material does not change size, the strain occurred by cooperative movement is called lattice invariant strain. Twinning is the dominant mechanism in SMAs, and because initial atomic bonds are maintained in twinning, upon heating to austenite the strain can be recovered, resulting in the shape memory effect. However, atomic slip or generated defects result in shifts which cannot be realigned upon re-transformation. In equiatomic or near-equiatomic NiTi the austenite phase has a (B2) cubic structure and martensite a (B19’) monoclinic structure.

In polycrystalline materials, which macro-scale SMA systems would be, multiple twin planes exit because of the available orientation of martensite variants to the cubic parent phase. With 12 twin planes available and mirror martensite variants on each plane, 24 martensitic variants exist and 'self-accommodate' to minimize strain energy and under zero stress conform to the original macro shape. Under load, which will resolve as a shear stress on the twin plane, the self-accommodated twinned martensite will begin to de-twin starting with the variant most aligned with the orientation of the stress and therefore the lowest critically resolved shear stress. Theoretically twinned martensite variants will continue to de-twin to respond to ever increasing amounts of stress and remain fully recoverable. In-practice, in certain variants the stress will cause martensite slip in favor of detwinning resulting in a macroscopically observable plastic strain that cannot be fully recovered. In cycling operation of SMAs this is the origin of irrecoverable strain or 'open loop strain' which can reduce dimensional stability, predictability, or component lifespan [27-33].

By tailoring microstructure, it is possible to the control the slip/twin pathways. Mechanical work (drawing, rolling, extruding) cause dislocations which act as barriers to slip improving the SME of NiTi. Working does not cause severe localized plastic deformation by the same mechanism as subtractive machining, resulting in nearly all off-the-shelf NiTi materials being drawn wire or extruded rod stock. Precipitation of an alloying phase can also be used to tailor microstructure. extremely common in ternary systems to be discussed later, aging above 400°C grows Ti_3Ni_4 (Ni_4Ti_3 depending on source) lenticular precipitates which can improve mechanical performance. Specifically,

in NiTi the stress fields from the precipitates can cause an additional intermediate phase to form, ‘R-phase’ so called for its rhombohedral intermediate structure [34]. Microstructural training can also be done which cycles an SMA to an upper training load, mechanically cycling the slip out of the system to a final uniform and predictable strain, resulting in a final set point for the martensite as well and creating two-way shape memory. This strain can be fully recovered so long as the load does not exceed the training load [35].

Cyclic stability before or after training is an extremely critical area for understanding and continued development of SMA actuator systems. Detrimental microstructural development during cycling is known as ‘functional fatigue’ (or mischaracterized as creep) within SMAs and while it does appear like creep as irrecoverable deformation from external loads below yield strength it is a function of transformation-cycle, not stress-cycle or time [36, 37]. Gao et. al. demonstrated that during transformation cycling defects including dislocations and special grain boundaries generate because of symmetry breaking along symmetry-dictated non-phase-transformation pathways (SDNPTP) that are activated easily by internal or external stresses. Additionally, as a trend, SDNPTPs are easier to activate if the crystallographic orientation of martensite is close in orientation to a high symmetry structure like HCP [38].

Practical applications of SMA actuators need to be resilient to a lifetime of thermomechanical cycles and have stability in the shape memory response [39]. While are several phenomenological complexities which have yet to be fully addressed,

common loading conditions have been modeled effectively enough to develop an engineering toolbox to allow practical design of such materials [40-45]. There have been many commercial products that have taken advantage of NiTi's near 8% recoverable strain and its wide availability. However, actuators perform sub-optimally in situations where unstable transformation cycles and instabilities occur from functional fatigue or martensite slip, both are recorded with increased regularity observed in HTMSAs in association with elevated temperatures. NiTi systems represent the most explored SMAs and there have been specific attempts to systematically correlate thermodynamics, microstructure, and mechanics of NiTi SMAs [39]. Unfortunately, composition variance and heat treatment only enable NiTi to operate to a maximum of 120°C, above that, ternary additions are required. Unfortunately, much of the microstructural control noted previously gains novel complexity when adding alloying elements that must be addressed for each individual compositional system.

Ternary HTMSA Microstructure Variation

Ternary (quaternary, quinary, etc.) NiTi-based SMAs are often designed to improve a perceived weakness in the binary NiTi. Additions can replace either nickel or titanium within the underlying lattice, though the amount of misfit can cause stress fields inducing an intermediate transformation phase from NiTi's B2 → B19' where the martensite phase instead becomes B19 orthorhombic as is the case for Pd, Pt, and high concentrate Cu substitution systems. Some elemental additions directly substitute in the matrix phase at concentrations even higher than the base Ni or Ti, e.g. $Ni_{20}Ti_{50}Pd_{30}$ but others like Ag or Nb fall out of matrix suspension at even mild concentrations (<5 at.%),

the latter being detrimental to mechanical shape memory response since the maximum recoverable strain response is bound by the transformation fraction of the matrix. This is a known effect with carbon residuals in graphite melting crucibles causing large carbide formations which are deleterious to hysteresis and mechanical performance of fabricated alloys. Comparable alloy compositions in literature melted in graphite crucibles should not be trusted for accurate hysteresis measurements.

Alloying elements which would not serve the objectives of this study are not mentioned here, the reader is referred to the NASA Shape Memory Alloy Database for further information [46]. Cu improves ductility and lowers hysteresis in NiTi without significant impact on transformation temperatures at up to 5% Cu, however, with increasing concentration to a critical point the additional copper causes a secondary transformation to occur, now B2→ B19→B19'. Continued alloying generates another unique transformation above ~>13 at.% Cu where the transformation is B2→ B19 exclusively. At high Cu concentrations hysteresis is minimized but has significantly lower work output and lower load resistance in SME configurations [47]. Pt, Pd, Au alloying have been shown to increase, to varying levels, transformation temperatures while retaining very low hysteresis. Frenzel et. al. showed $Ni_{20}Ti_{50}Pd_{30}$ with Ms temperatures above 250°C with a near 30J/g ΔH indicating a strong candidate for HTSMA use. High ΔH is a signal for the high orientation mismatch between martensite and austenite phases requiring additional thermal energy (and if slip can be mitigated) high actuation strain potential. Hysteresis width, ΔT is related to the energy barriers at the martensite, austenite interface consisting of interfacial twin boundary energy, elastic

energy in transition layer, and bulk free energy difference between the phases [48]. Minimization of hysteresis occurs at the optimization of compatibility between parent austenite and twinned martensite phases, as $\lambda_2 \rightarrow 1$ in B2→ B19 transformations [49].

The challenge with Pt and Pd in large concentration is their cost as precious metals. At a lower cost, Hf and Zr have both been shown to significantly increase transformation temperatures especially in high concentrations. Though these have significantly lower work output than binary NiTi and increased (lower performance) hysteresis than NiTiPt or NiTiPd. The lower strain is associated with increased temperatures promoting slip or defects over reorientation when compared to binary NiTi, but high concentrations of Hf or Zr show improved hysteresis to binary NiTi systems. The mismatch of phases in NiTiHf/Zr compositions also results in a λ_2 with a large deviation from 1, however even though none of the martensite variants are individually compatible with the parent austenite phase a 'martensite mosaic' can be formed which approximates compatibility and results in a wider range of compatibility for B2→ B19' transformations [50]. Though the trend indicates its theoretically possible optimized orientation of the mosaic has not to date shown ΔT below 20°C [51]. Precipitates, grain orientation, nucleation sites, and chemistry and other characteristics collectively impact the performance of SMAs making a thorough investigation of even one chemical system a significant challenge, and exponentially more complicated as additional alloying elements are added to the matrix.

H-Phase Precipitation

To optimize an SMA for mechanical output the aim should be to maximize work output, specifically, a large (>3%) recoverable strain at high tensile load (>300MPa) with insignificant irrecoverable strain (<0.01%) while minimizing hysteresis and operating in the temperature regime of interest [52]. To allow for high loading conditions SMAs need to undergo mechanical working to preferentially orient and normalize grain structure as the as cast or melted structure is not microstructurally uniform. Often, SMAs are then heat treated above solutionization temperature (>900°C) to ensure a single-phase alloy. After, via lower temp heat treatment (450°C-700°C), nickel rich high Hf/Zr containing alloys can microstructural improvement occur via precipitation of a nanoscale Hf/Zr rich secondary phase occur. This precipitation, known as h-phase deviates in structure and action to conventional Ni_4Ti_3 precipitates in NiTi. H-phase is fully coherent in the B2 austenitic phase. In addition, in small sizes (lenticular growth <20nm) during martensitic transformation the martensitic variants can grow and consume the h-phase with little to no interference. This means little impact on thermal hysteresis or in cases where the resulting crystallographic accommodation improves symmetry with austenite, improves ΔT. However, where h-phase is most notable is in cases where the small h-phase particles act as barriers to slip and plastic deformation through the material. In these cases, h-phase causes an increase in cyclic stability, strain at a given load, and reduction in irrecoverable strain.

Though there is a large body of work dedicated to H-phase precipitation, a direct relationship between h-phase parameters (size, stratification, volume fraction) and

mechanical performance is still lacking. Though one proposed idealized size for h-phase in $Ni_{50.3}Ti_{34.7}Hf_{15}$ is coherent 4nm spindle shaped precipitates which reduces hysteresis and maximizes matrix strength, it is unknown whether this is exclusive to this material or a broad trend (evirgen 2012 effects of aging). Most literature reports generalize for very small (<5 nm), small (7-20nm), medium (20-50nm), and large (>50 nm) precipitation effects. Desired precipitation effects are application specific, for example, high cycle fatigue optimized h-phase properties do not necessarily align with high work output [53]. In general, small coherent precipitates do not appear to hinder actuation strain even at high volume fractions, though at some coarsening size, precipitates are no longer coherent and in addition to causing a decrease in the availability of transformable martensite cause lattice mismatch which is detrimental to mechanical performance.

While they are used interchangeably here it is important to note the precipitating kinetics and compositions of NiTiHf h-phase and NiTiZr h-phase will differ, as will the size and location of the precipitates under various heat treatments, dependent on chemistry. Yang et. al. found H-phase in a $Ni_{50.3}Ti_{29.7}Hf_{20}$ alloy to be $Ni_{\frac{1}{2}}Ti_{\frac{1}{6}}Hf_{\frac{1}{3}}$ but specifically noted the capability for h-phase to accommodate an extreme variation of compositons on account of anti-site, APB, or additional mechanisms [54]. The rate limiting factor in coarsening kinetics is driven by solute diffusion [55, 56]. For identical temperature, Zr-based H-phase growth can be 16x faster than that of Hf-containing H-phase. Additionally complex systems where a single solute may dominate, i.e. NiTiHfZr have not even been investigated.

Very short duration low-temperature aging results in formation of dense localized distribution of small precipitates with limited interparticle spacing which increases resistance to martensite nucleation, decreasing transformation temperatures. However, longer-duration low temperature aging increases stratification of small precipitates promoting martensitic nucleation. In both long duration low temperature aging and high temperature h-phase precipitation depletes the matrix Ni-content causing an increase in transformation temperatures [56]. For an SMA actuation, there is a balancing act between particles large enough in volume fraction to improve mechanical strain and decrease irrecoverable strain, but not so much as to deplete the matrix to cause transformation temperatures to fall out of desired envelope and optimize size for phase compatibility minimizing hysteresis. Accurately encompassing the performance is only further hindered by the need for TEM to analyze the resulting precipitates and prediction of nucleation and coarsening is extremely variable according to chemistry as well as heat treatment temperature and duration. Santamarta et. al. showed for a given fixed starting alloy, say $Ni_{50.3}Ti_{29.7}Hf_{20}$ increasing Ni content increases growth of the precipitate and for fixed Ni, coarsening is accelerated by increased Hf [57]. Additionally, Shuitcev showed for the same base alloy an of 100°C in aging temperature can increase coarsening rate by 50x. For any composition it is theoretically possible to minimize hysteresis and maximize mechanical performance with an idealized temperature range via microstructural control leveraging the mechanical and chemical effects from h-phase precipitation.

L-PBF of NiTi

Nitinol Alloys are shape memory alloy systems consisting of some combination of Nickel and Titanium, though they are often limited to Nickel contents between 46 at.% and 54 at.% to ensure shape memory properties. While chemical modification has been an active area of study for decades, additive manufacturing, here specifically L-PBF is a growing method for fabrication of shape memory alloys. This is primarily due to the difficult to machine nature of NiTi, which carries over to multi-element NiTi based systems [58, 59]. L-PBF technology can join conventionally non-weldable materials (not specifically NiTi-based alloys [60, 61]) and enables fabrication geometries that are not possible in conventional machining [22, 62]. The possibilities of leveraging this technology to fabricate and develop shape memory materials, which are classically averse to machining, is extremely promising, though not without challenges.

NiTi systems are extremely susceptible to small variations in chemistry (<.1 at.% Ni Content) and the most accurate chemical analyzers (ICP based system) have a greater than one percent relative tolerance rate which means when analyzing a composition with 50% Ni, a valid, and accurate chemical assessment can range from 49% at. Ni to 51% at. Ni. Accurate, while also being inadequate to the level of detail required for tuning SMAs [63]. Unfortunately, NiTi systems are also sensitive to small impurity changes, which are common in L-PBF processes [64]. L-PBF systems also have extremely high cooling rates, which can affect both grain structure, grain orientation, and cracking in the matrix due to residual stresses [65-67]. Though by the same token it is possible to manipulate grain structure and orientation and potentially control the same defects [68].

Research groups from all over the world have successfully fabricated near equiatomic NiTi materials across a range of energy densities NiTi. Unique to the material is changing parameters including speed, power, part orientation, and raster strategy have all been shown to affect transformation temperatures, a fundamental feature of shape memory materials [69-71]. The most cited explanation for change in the shape memory effect as a function of printing parameters is the lower vapor pressure of nickel along with its lower vaporization point and lower vapor pressure head causes preferential evaporation of the nickel in high energy regimes which decreases the availability of nickel in the final SMA matrix causing an increase in transformation temperatures. It would follow, and has been observed, that at higher energy densities transformation temperatures would increase as is seen in Figure 4**;** however, why there appears to be a lower limit of nickel richness in near equiatomic NiTi or Ni lean NiTi compositions has not yet been well explained.

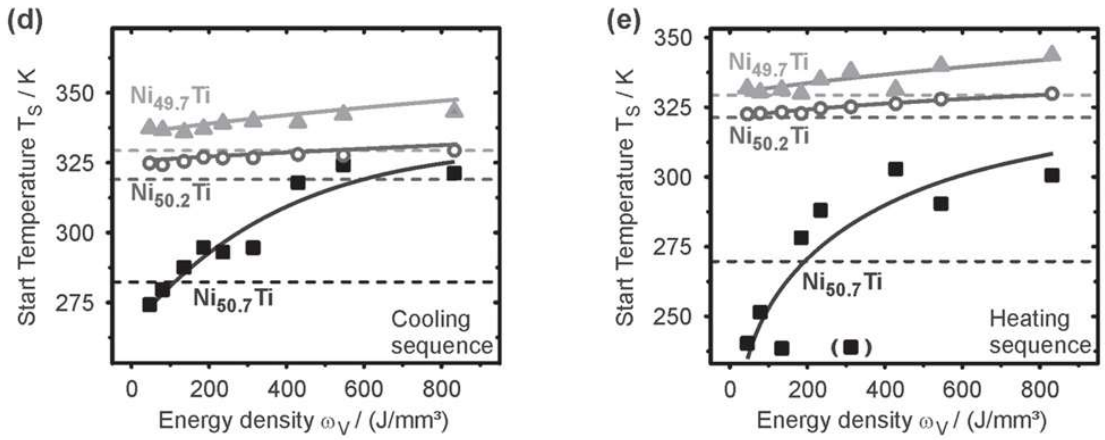

Figure 4: Energy density dependence on temperature of transformation for both **a)** martensite start and **b)** austenite start for various compositions [3]

Mechanically, AM developed NiTi has been shown to perform similarly to traditionally fabricated parts in terms of shape memory response, but the limiting factor is process control. Factors that heavily influence failure or sub-optimal results are impurities which form Ti or Ni oxides as well as porosity. This is specifically noticeable in a gap in peak tensile strength between traditionally fabricated NiTi and AM NiTi. Like other AM materials, there is an energy density floor below which significant lack of fusion porosity prevails and only above which highly dense parts have been shown to be successfully fabricated [3]. However, because of Ni evaporation fully dense parts tend to have at least a slight shift in increased transformation temperatures. Therefore, developing an alloy to transform in a specific range, then printing fully dense parts that transform identically is not trivial.

It has been recently shown that NiTi can be fabricated into interfacing mechanisms that take advantage of the shape memory effect in as-built condition [19]. While this demonstrator piece requires mechanical deflection after fabrication process parameters which cause preferential heating to induce or control shape memory effect along specific geometry locations to tailor a devices SME in-situ are likely to enter the literature in the near future.

L-PBF of NiTiX(Y,etc.)

Ternary, quaternary, quinary, etc. nitinol materials primarily consist of Ni and Ti but alloy atomically similar materials as matrix replacements for either Ni or Ti. Nickel replacers like Au, Pd, and Pt have been alloyed for up to ultra-high temperature (>400°C) shape memory response [3]. However, because of their expense, there is

significant research interest to find lower cost alloying elements which still allow tailored high temperature (>100C) shape memory response (Hf,Zr)[28-30], bio-capability(Ag) [31], or minimization of hysteresis(Cu) [32].

Development timeline

A timeline of NiTiX development is key to understanding during process of novel material development, which is not dissimilar to the research conducted here, what challenges other researchers met and how they resolved the issues and what new information would be directly attributed to the widening of scope. The earliest ternary NiTi-based shape memory alloy, $Ni_{49.8}Ti_{30.2}Hf_{20}$ was a Ni-lean NiTiHF blend produced in 2018 and the majority of the AM NiTiHf literature has been dominated by the Elahinia group which is also responsible for the highest cited NiTi AM review and is conveniently located for significant cooperation to NASA Glenn [20]. NiTiHf enables high temperature shape memory effect at a lower cost than other materials which have also shown to increase transformation temperatures like Au, Pt, or Pd, in addition it can be strengthened by aging while maintaining work output and dimensional stability [33]. Three years after the initial publication of NiTiHf in AM the Elahinia's group published in-situ synchrotron evaluation of compression tests on the same composition AM materials [34]. Here they investigated the dynamic microstructure reaction of H-phase, the precipitation hardened nanophase found in NiTiHf and NiTiZr.

Nematollahi et. al. was the first to perform L-PBF fabrication on a Ni rich composition $Ni_{50.4}Ti_{29.6}Hf_{20}$, possibly to respond to the findings of their earlier work with NiTiHf [8]. While one driver of this composition selection may be due to H-phase

precipitation, it resulted in the first study to show the large impact of machine parameter variation on transformation temperatures “NiTiHf samples show a very broad range of TTs starting with Af from 100 to 400°C”. Additionally, this followed with the first proposal of a secondary mechanism causing the level off in transformational change. VED appears correlated with TTs up to a point, Nematollahi et. al. estimate this is from Ti-rich TT sensitivity, but the author believes it could be due to melt pool mechanics and steady state vapor pressure and temperature preferentially nickel under certain conditions and vaporizing both nickel and titanium under others. The latter being supported by Nematollahi’s note that “where certain points have identical energy densities and different transformation temperatures Ev alone cannot explain the transformation behavior”. Nematollahi ran a large design of experiments (not model informed) to determine printing parameters. Less than a year later, from the large sets of data, two points were chosen and analyzed in detail with relation to thermomechanical properties in Toker et. al. [35]. The interest was specifically the mechanical variation that would occur in two similarly dense materials but one that was fabricated with significantly higher energy input.

2020 marked the first departure from just developing process parameters for NiTiHf materials. Elaninia’s group via Dabbaghi became concerned with and published on the oxygen susceptibility of traditionally and AM systems for both NiTiHf and NiTi, it should be noted their reported chamber oxygen was between 700 and 800ppm O_2 when it was reported by the group [36]. At the same time (2020) Wang et. al. published a paper with dramatically improved mechanical ductility of NiTi in tension which was

rationalized as a function of the ultra low O_2 content (<25ppm) [37]. Simultaneously, other researchers started to either improve on the NiTiHf systems via microstructural control [34], or developments of novel materials like NiTiNb, NiTiZr, or HEAs, and where the materials were not off the shelf, mechanical powder doping was used to develop the feedstocks [5, 38-40]. The field for ternary or additionally more complicated SMA compositions is only growing.

Novel Developments

Microstructure control is critical to NiTiX materials as even compared to NiTi systems they are more brittle [41]. Even at low power inputs Elahinia et. al. developed microcracks in NiTiHf, though the author noted Ti-rich systems suffer decreased ductility, strength, resistance to slip, and enlarged hysteresis (A_f-M_s). Additionally, Shen et. al. showed AM NiTiX systems strengthened by precipitation hardened nano-H-phase has even more anisotropy in AM than in conventionally fabricated systems, here being extrusion. While not wholly understood, it is possible to forecast an AM fabrication process that would allow microstructure tailoring to increase work output, loading resistance, or other texture-based properties in SMA systems. “Thermomechanical behavior of NiTi-based shape memory alloys is greatly dependent on its microstructure characteristics” and controllable if tailoring can be achieved as it has with other materials [42, 43].

One development worth noting is the interesting methodology that groups came up with to develop novel feedstocks when compositions used in experiments are not commercial off the shelf. Liu et. al. used high purity binary NiTi powder within range of

L-PBF systems and mechanically alloyed the material with significantly smaller Nb particles, aiming to produce a $Ni_{44}Ti_{44}Nb_{12}$ eutectic point alloy as described by the pseudo-binary diagram in Figure 5 a). While the mechanical alloying did develop a homogeneous powder system with particles of Nb impregnated onto the surface when

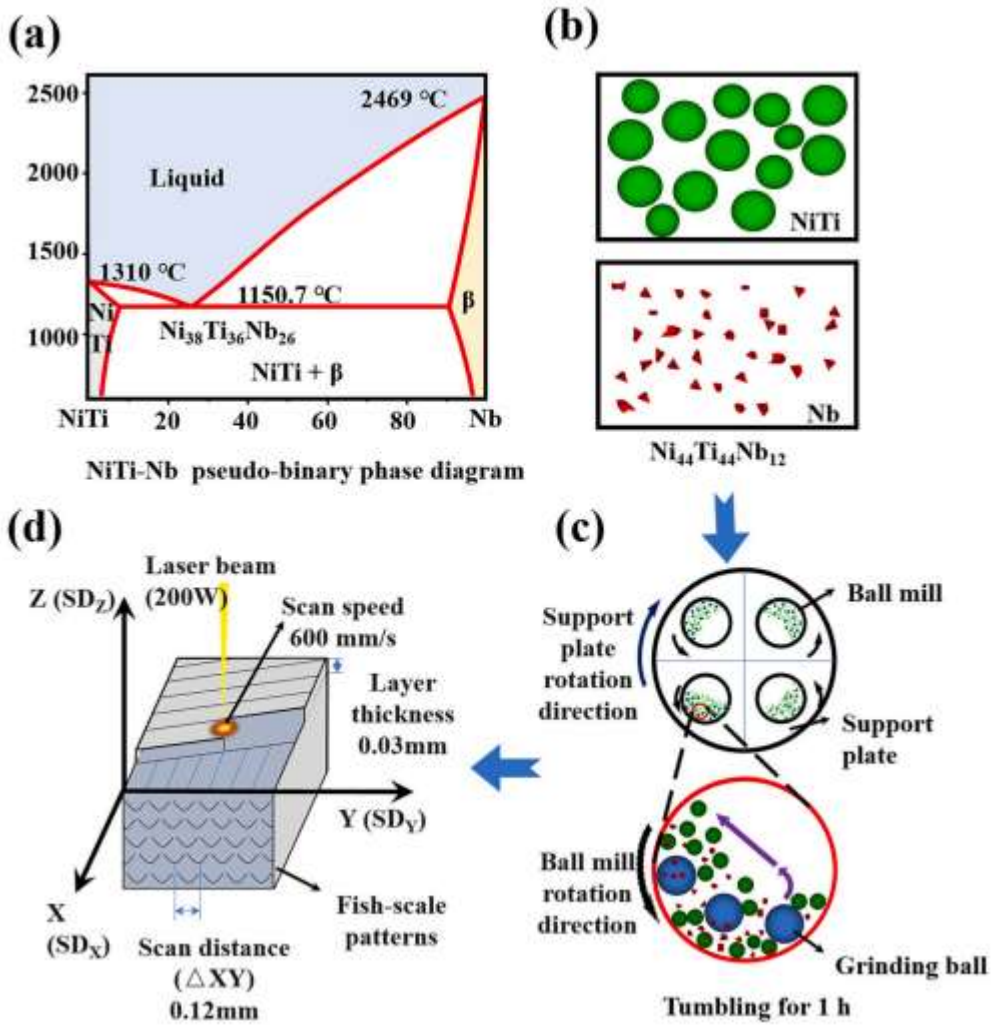

Figure 5: a) Development of L-PBF feedstock by thermodynamic analysis, b-c) powder mixing via mechanical alloying of dissimilar powders, d) L-PBF fabrication from [2]

observed through SEM, the mixing forces in the melt pool did not effectively mix the particles and large Nb concentrations existed in the final part. Similarly, Chen et. al.

'decorated' their NiTi feedstock with HfH_2 particles, though the dispersed, non-matrix homogenized, nature of the final product seemed to be in line with their goal of spreading hafnium to improve critical stress of martensitic transformation [44]. Finally, Razumov et. al. used ball milling to pre-alloy a high entropy $Ti_{25}Zr_{25}Ni_{25}Co_{10}Cu_{15}$ prior to atomization which resulted in a homogeneous feedstock, though the group did not observe shape memory effect in either conventional or AM fabricated parts of that alloy.

Transformation control

Nematollahi et. al. from Elahinia's University of Toledo group was specifically designed to be a large parameter set to both analyze the variances in settings that would allow high density fabrication, but also inform transformation variances as they relate to speed, power, hatch spacing, and volumetric energy density (VED) for $Ni_{50.4}Ti_{29.6}Hf_{20}$

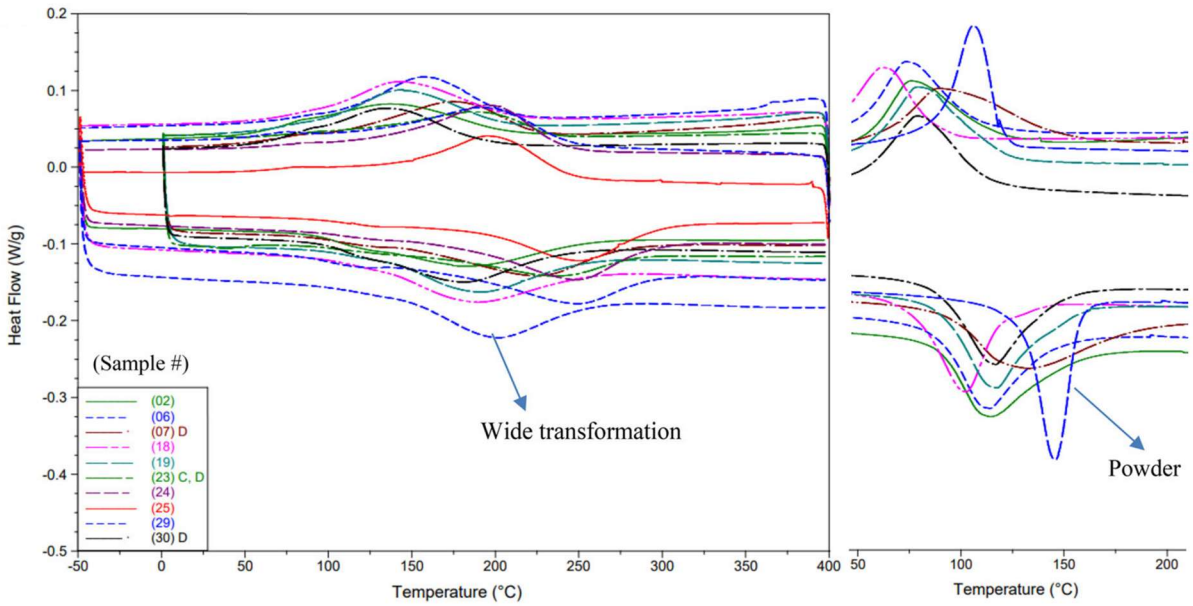

Figure 6: Variation of Af temperature for Ni50.4Ti29.6Hf20 from [9]

[8]. While they were able to show a transformation variance in A_f from 100°C to 400°C,

only a third of the materials did not have delamination, cracks, or gas entrapped porosity and the lowest A_f of a successful build occurred at 254°C. The range of interest for this research (200° - 300°C transformation range) is included in Figure 6; note the change in width compared to the powdered sample which could be an artifact of non-homogeneity in as-built parts.

Zhang et. al. also observed a significant variance across parameter space in their research with Ms ranging from 160°C to above 300°C but with a significantly higher density which could be an artifact of the printability map development over basic guess and check [72]. While both groups noted VED via power and speed were largely responsible for transformation temperature variance, Nematollahi specifically claimed hatch spacing did not, which runs counter to intuition and other literature. Finally, Xi et. al. showed one of the most interesting transformation curves in literature to date whereby alloying 3% Nb to $Ni_{50.6}Ti$ transformation temperatures became agnostic to machine parameters as is visible in Figure 7 [2]. That is, the transformation did not change significantly at any speed between 500mm/s and 1100mm/s, and similarly varying from 120W to 240W laser power. Opposite to tailored transformation temperatures, if a similar resistance to parameter changes could be chemically

programed into other species the repeatability and industrial applicability of an AM shape memory would rapidly expand its production application.

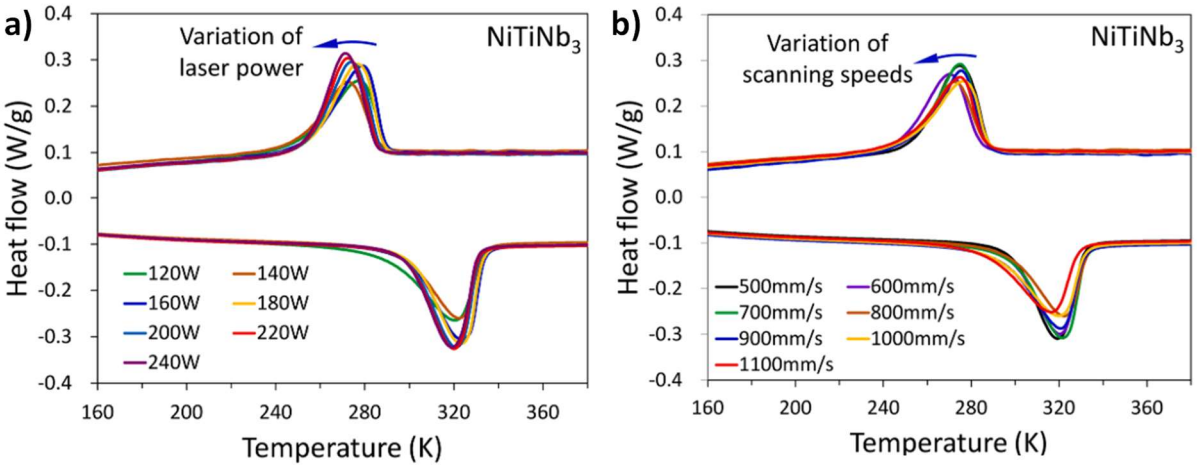

Figure 7: M_s temperature for Nb doped $Ni_{50.6}Ti$ when varied by a) laser power and b) scanning speed [2]

Imperfections

NiTiX materials appear to suffer from brittle failure at a very high rate, whether at the interface, the bulk, micro-cracking, or non-uniform solidification. Nematollahi notes one tradeoff with Ni-rich systems allowing transformation control is that they are innately more brittle than Ti-rich systems. However, it could also be associated with oxygen pickup, Dabbaghi et. al. studies oxidation effects and layer development for NiTi and NiTiHf AM systems. While oxidation kinetics are not observed for a built sample below 500°C the melt pool is considerably hotter, and solidification of oxides in the outermost region of the melt pool could cause instability and drive brittle microcracks. What is interesting is the oxygen pickup from long term exposure in AM samples is lower than in traditionally fabricated samples; though if that's because AM samples already have oxides and hit saturation limit sooner was not given as a rationale.

Zhang et. al. were the first to analyze L-PBF NiTiZr and through 25 high power and 16 low power systems did not determine a single system without some level of crack propagation[11]. As if the material is innately brittle. Notably cracking was connected to the directionality of solidification; where cracks develop at the center of a melt pool in a profile view, as if to say the slower solidifying material at the center of a melt pool is unable to cope with the faster solidification near the edges of a melt pool. Interestingly the researchers also concluded the solidifying microstructures were entirely different at the center of a melt pool and areas of rapid solidification at the edge in NiTiZr, indicating the fracturing may not be a function of NiTiZr being more brittle than say NiTiHf but that processing must be better tuned to the NiTiZr system. Zhang's description of crack propagation is shown in Figure 8. In response the team attempted to heat the powder bed at varying intervals but ran into inhomogeneity, excess oxidation, poor formability, and other challenges, which mirror Sun et. al.'s attempt at fabricating samples for tensile testing [73].

Mechanical testing is often developed to resist failing in associated with the imperfections in AM parts. SME is dominantly tested by compression specimens which are significantly less effected by internal porosity, stress concentrations, or brittle behavior. Additionally, rapid failure propagation tests like Charpy impact would be good to find large imperfections as the rapid strain would propagate from a weak point, however it would not be informative for bulk mechanical properties. Elahinia's group has recently tested the first printed torsion specimens (NiTi) for actuation testing, which if it is stable, marks a notable milestone.

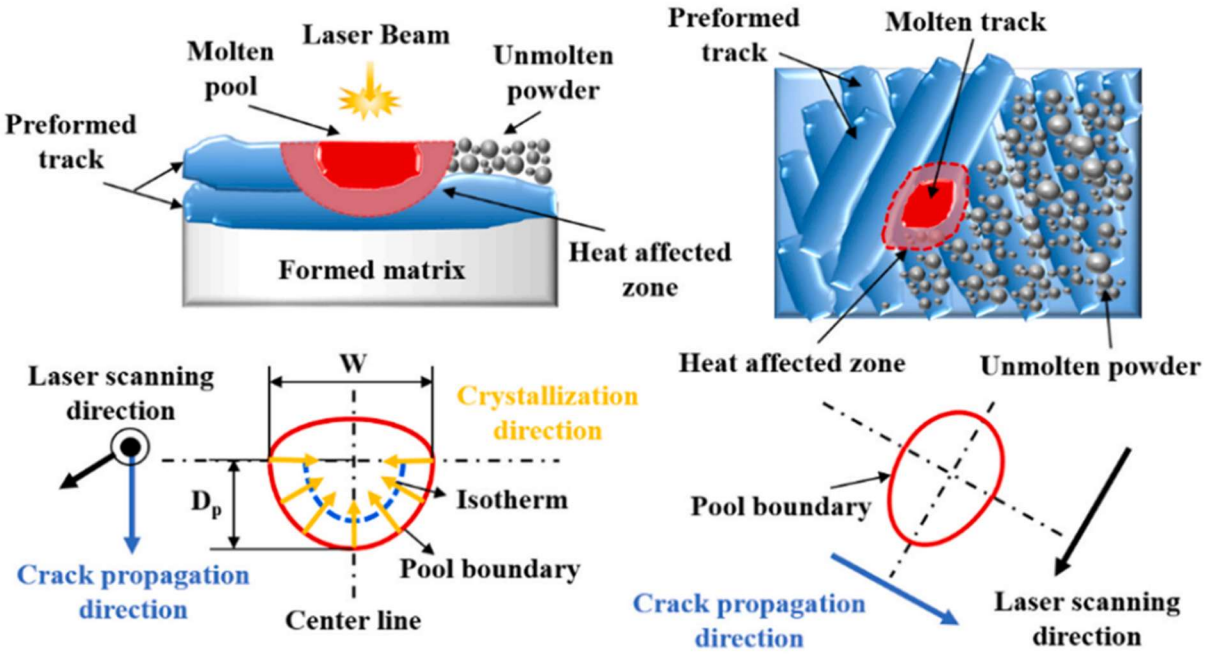

Figure 8: Microcrack formation and propagation direction for inter-melt pool and interlayer cracking as reported by Zhang et. al. in NiTiZr [11]

Successfully Fabricated Compositions

If successful fabrication is marked by stable testing, near zero porosity, and no microfracturing; the only material successfully fabricated in high temperature NiTi based SMA space are ternary NiTiHf alloys. To date NiTiZr has not been fabricated without microfractures, both through and across the melt pool track. NiTiNb does not depress the onset of martensitic transformation above 100°C, and quaternary and quinary systems have not yet appeared in literature.

AM of Other SMA Systems

While the most popular alloy system for shape memory effect in terms of research and economic use is NiTi, other systems exist and have been successfully fabricated in L-PBF systems. Though many lack stability, work output, high temperature actuation, or combination there-of that are available in NiTi systems.

Specifically in the case of Cu-based SMA systems, they present a lower cost and a similar processing window than NiTi based systems, but lack ductility and fatigue life [74]. However, Silva et. al. also notes the ability of SLM fabrication systems to control microstructure can improve mechanical response. In Alagha et. al.'s 2021 review paper on L-PBF SMA systems the ability to achieve greater than 99% density is achievable in Cu-based systems. However, increased energy density results in preferential composition vaporization causing a non-monotonic relationship between energy density and part density [64]. In addition, since the review was published multiple other Cu-based AM systems fabricated by L-PBF have observed trace element change across process parameters, even if transformation temperatures remain relatively similar [75, 76]. This

could represent a challenge in industrial fabrication of Cu-based systems as the only way to confirm property variation would be to check microstructure, which has a strong effect on final mechanical properties as noted by Reyes, Gargarella, and Tian et. al.[77-79]. Though on the other hand, the L-BPF also enables individually designed superelastic parts in the case of Babacan et. al. or doping of precipitation strengthening phases as in Abolhasani et. al. [80, 81].

Iron (Fe-Mn-Si) based SMAs have also gained significant recent reseeach especially due to their high cyclic stability, albeit over a much lower strain amplitude than NiTi based systems [82]. have also been fabricated by AM systems, there is a significant interest in them in large scale construction systems where AM would not only be beneficial in tailoring microstructure but also geometries [83]. In the first instance of successful fabrication via L-PBF high strength, elongation, and ductility were observed after heat treatment, even exceeding conventionally fabricated materials [84]. However, like other materials made by L-PBF the materials were directionally dependent, anisotropic, have non-uniform composition vaporization, and are highly dependent on process parameters [4, 5, 85-88]. Though without the oxygen affinity of materials like Ti, Fe based systems may be more resistant to chamber oxygen. One unique application was the 4-D flowers developed by Ferretto et. al. and shown in Figure 9 in addition to mechanical test objects like dogbones or compression specimens.

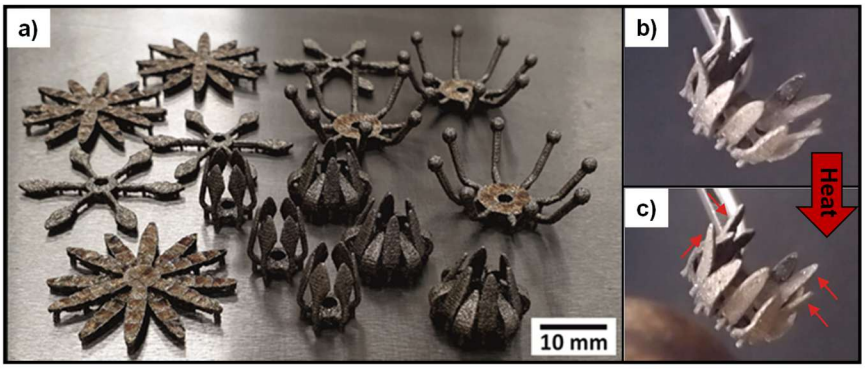

Figure 9: 4-D metal parts made from Fe-based SMA, **a)** as printed, **b)** deformed in martensitic phase, **c)** recovery of shape via heated transformation to austenite [4]

Ni-Mn-Ga SMAs are magnetic instead of thermal materials which are brittle in polycrystalline form and present significant macro-fabrication challenges [64]. Uniquely, many different AM systems have been utilized to develop Ni-Mn-Ga SMAs including SLS and binder jetting [89-94]. The as-sintered samples have been observed to be paramagnetic but also suffer from significantly reduced density as compared to other methods, as high as 24.08% porosity [89]. However, sintering of the green parts has been able to achieve in excess of 99% dense parts with tight control of the multi-regime sintering that occurs in Ni-Mn-Ga [94]. It should be noted sintering time does not just change the densification of the material but can also affect transformation as is the case with L-PBF. Laitinena et. al. has extensively investigated Ni-Mn-Ga SMAs in L-PBF and have characterized large magnetic field induced strains, effects of alloying additions, and response to heat treatment among many other conclusions [92, 95-101]. Given time, it is likely L-PBF and AM technology will enable wide exploration into existing and new SMA space.

Modeling of AM of SMAs

Modeling of interest in additive manufacturing and computational material science can be broken down into 3 distinct categories researchers are aiming to predict or analyze; material compositions/performance, process optimizations, and melt pool/solidification dynamics.

Material Development

In the process of developing continuously more advanced materials for engineering applications a process needed to be developed that allowed for rapid iteration with a more refined problem bounds than the historic guess-and-check, or happy mistake, method. Materials informatics, rapid discovery enabled by machine learning and computational power, aims to fill the gaps in both and has had significant success across materials systems and industries [102-108]. There is even literature to support stand-up of the process anywhere via open-source code, akin to mathematics or modeling than traditional materials science [109].

Specifically in the case of SMAs, physics models and materials parameters allow neural networks to bound problems and make linkages through complicated interconnections beyond intuition, especially where complicated behavior is concerned. This is enabled by ML's ability to compute high dimensional linear and non-linear interconnected properties [110]. Though the complicated behaviors of SMAs do invite continuous improvement such as Ozen Engineering's update of the ANSYS SMA model behavior [111].

The novel material creation process via ML developed SMAs can most easily be visualized in Figure 10 from Liu et. al. where using data collection, the existing material development state can be established (pareto front) and compared to the goal material process window [10]. Once defined, physics informed materials modeling can be used to propose material compositions, which after experimental validation, can result in novel materials with highly desirable properties, such as a near zero hysteresis for actuator type applications or high transformation temperatures [112-117]. In addition, teams such as Zadeh et. al. have built models specifically to predict the unique transformation temperature phenomena unique to SMAs [118]. This approximates the process the current work seeks to create AM materials for KCNSC.

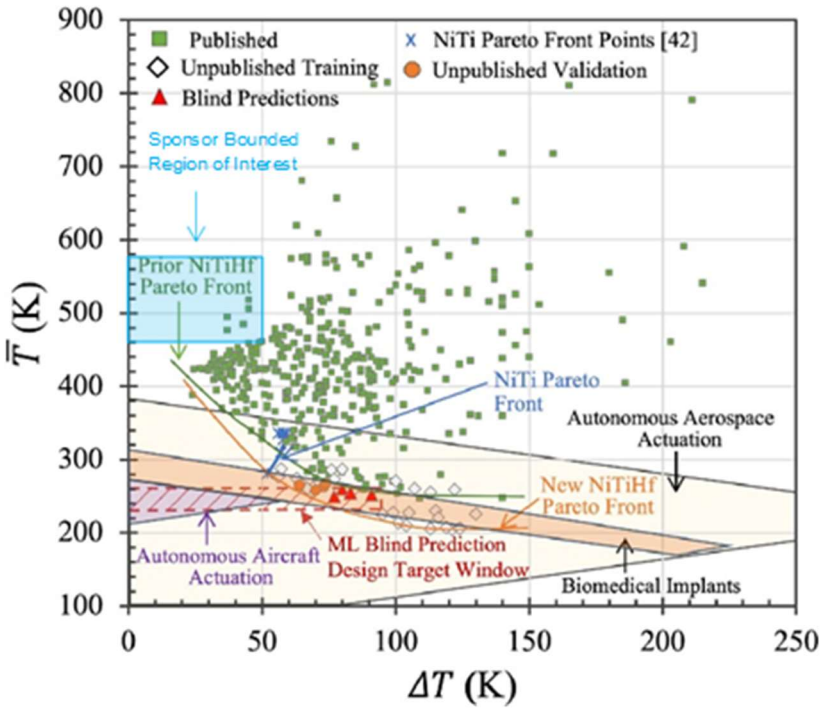

Figure 10: Modeled mean transformation temperature ($\overline{\boldsymbol{T}} = \frac{\mathbf{A}_f+\mathbf{M}_f}{2}$) vs transformation range ($\Delta \boldsymbol{T} = \mathbf{A}_f - \mathbf{M}_f$) including actuator overlays from [10] and overlayed area of interest

Process Optimization

ML for process optimization takes a similar approach albeit with a different aim, leveraging materials database, thermo-physics properties, and estimations of melt pool dynamics can be combined to estimate L-PBF process parameters that will create fully dense (or another quality metric) outcomes. There has been significant documentation associated with NiTi systems as detailed in the review by Mohamed et. al. [119]. As is the case with all SMA L-PBF literature on process parameters, beyond the interest of identifying regions of quality parts, there is significant interest, often aided by ML frameworks, in understanding the relationship of process parameters to transformation temperatures and residual stresses. ML is extremely broad; both modeling heavy simulation down to the near atomistic level in Li et. al. to optimizing simulations of direct experimental work as in Xue et. al. [120, 121].

To date the only ternary ML developed system is from Dr. Elahinia's group in Mehrpouya et. al. [122]. SMAs are also highly susceptible to variations in microstructure. Recalling literature in section 2, Zhang et. al. showed in experiments microcracking, and microstructure of highly dense parts directly correlated with melt pool propagation [11]. Therefore, accurate modeling of the melt pool in SMAs goes beyond understanding dynamics of keyholing phenomena, but may also hold the key to microstructure, residual stresses, and 4-D as-built structures [123, 124]. Modeling, and the digital factory at large, lends itself to significantly reducing the amount of time and cost associated with developing material recipes, or taken to the logical research goal, will enable development of AM optimized compositions which are resistant to inherent

processing challenges such as high rate of cooling, non-equilibrium material vaporization, or high residual part stresses.

Rapid Solidification and Splat Quenching

Fusion techniques such as EB-PBF and L-PBF rely on melting feedstock material into successive layers onto a substrate to build up geometries. The point heat nature of these processes results in extremely rapid cooling ($>10^5$ °K/s) of liquid material away from the heat point. The rapid solidification gives melting metal AM processes their distinct microstructures and the successful manipulation of heat flow in and out of the final part geometry can allow for control of microstructural evolution [125]. However the rapid solidification fronts and non-uniform phase growth is also the cause of micro and macro-fractures in certain material compositions, like conventionally castable Al 6061 unless specific control mechanisms are implemented [126]. For this reason, additive does not lend itself to all material compositions equally, especially not with detrimental phases that appear in rapid solidification regimes that cause stress cracking or cannot be heat treated out of the matrix. The presence of such phases, especially in complex conjugations of materials (ternary, quaternary, quinary, etc.) often require experimental fabrication to discover. With the expense of atomized powder, it would be of high scientific value to have a fabrication process with solidification rates controllable and comparable to additive manufacturing to determine instability of novel materials.

The Brewer group at University of Alabama, also in conjunction with KCNSC, developed a two-piston splat quench system to rapidly cool metal specimens across a range of temperature gradients. The system, illustrated in Figure 11 superheats a small

metal sample above melting point via induction then drops the metal where it is rapidly impacted by twin plates of large mass, rapidly removing heat from the sample and solidifying it near instantly. The solidification front varies from centerline and

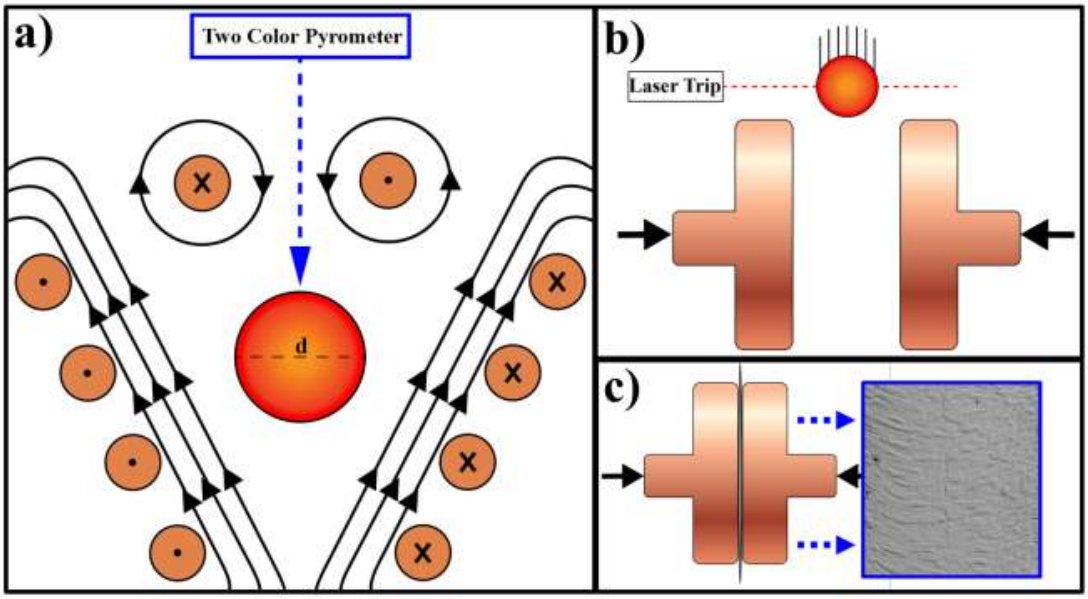

Figure 11: Representation of splat quenching processing **a)** levitation and superheating, **b)** falling and activation of sensor, **c)** platen collision **[8]**

depending on location can be used as a cooling rate equivalent to a range of additive manufacturing techniques as is in Figure 12 d). Brewers group has demonstrated success in relating grain size, composition segregation, and solidification structures from additive to splat quenched samples in stainless steels, nickel superalloys, and beta stabilized titanium, with a prediction the analog will hold for other materials [127-131]. The splats are also solidified in high purity inert gas environments so they could also be used as verification of oxygen sensitivity compared to solidification rate sensitivity in cases where literature has been unsuccessful at fabrication but chamber O_2 content is not known.

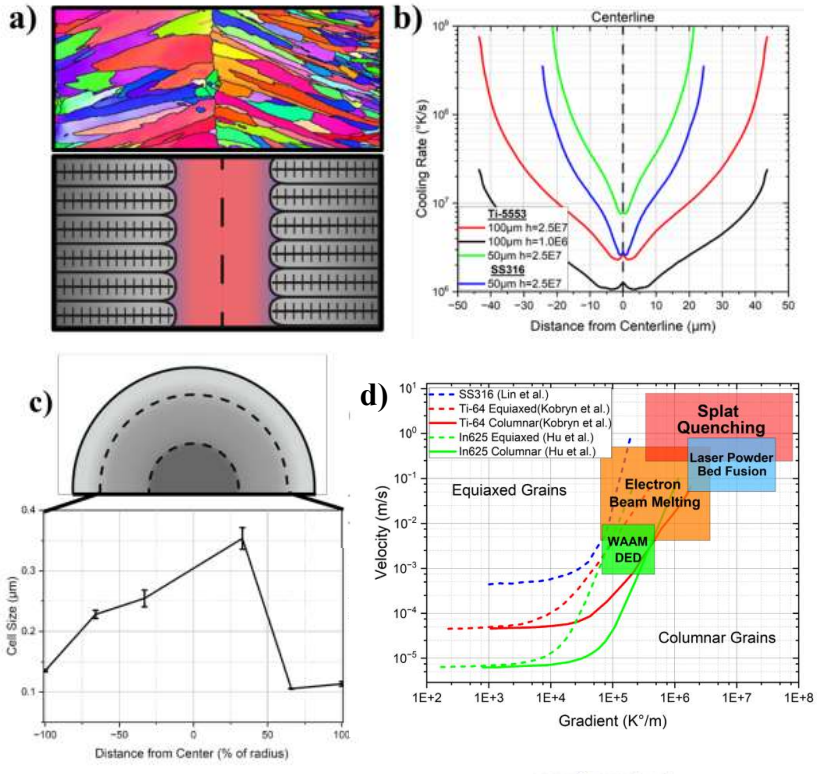

Figure 12: a) inverse pole figure and orientation of solidification into centerline of splat, **b)** cooling rate variance as a function of centerline, **c)** representation of the location of splat analysis to microstructural variance, and **d)** solidification gradient as it compares from splat quenching to various AM processes.

CHAPTER II

METHODOLOGY

The methodology used in this work effectively breaks down into the engineering solutions for the following three processes steps. To develop novel materials in a time-efficient manner a constrained machine learning model was developed that could predict measurable SME quantities like transformation temperature and be re-trained as the project iterated through sample sets. The pure accuracy of the model is not directly of interest, rather its ability to indicate trends and alloy compositions that may result in meeting requirements; therefore, predictions were compared with group domain expertise to determine compositions for fabrication. Selected compositions are fabricated into samples which can be tested for SME characteristics of interest and compared to existing literature data to determine optimal compositions to further investigate. The down selected compositions will be the focus of rapid solidification analysis and, in future work, atomization.

Model development and Predictions

The machine learning model utilized in this research was built from Dr. William Trehern's AIMS paper model to discover low hysteresis alloys [112]. The model was informed by the shape memory materials database controlled by PhD student John Broucek owned by Dr. Karaman's MESAM lab. The database included internal unpublished data as well as scrubbed literature data. It includes over 12,000 discrete transformation points for SMAs. Data is cleaned for duplicates or errors such as $\Delta T < 0$

or sum of composition ≠ 100%. In a step away from Dr. Trehern's AIMS paper the generated model was a deep neural network with feature engineering but without hyperparameter tuning. The dataset was then split 80/20 (percent training, testing, respectively) and n=2 models were independently trained to predict transformation temperatures M_s, M_f, and A_f, from which transformation range ($A_f - M_f$) and hysteresis ($A_f - M_s$) can be calculated.

The compositional systems searched by the developed model were NiTiHf, NiTiZr, NiTiHfZr, NiTiCuHf, NiTiCuHfZr. Elements like Ag, Rh, Al, and others were either eliminated for lack of datapoints, cost, or unknown mechanical formability. Though high temperature SMAs can be achieved through additions of Pd, Pt, and Au, the confidence interval the model had with such materials was not high enough to justify the cost associated with using these materials for specimens larger than button (4.5g) samples. In addition, such materials would result in significantly higher cost to create an ingot to be atomized, especially considering the yield of the process is not above 60% based on experience in the research group. Available elemental additions were chosen by those that cost less than 50% of Pd, per gram, and have been shown in literature to decrease hysteresis and/or increase martensite start temperature while eliminating elements that significantly reduced ductility, were not heavily investigated, or did not form a single phase with NiTi after homogenizing heat treatment. Resulting alloying elements of interest were Cu, Hf, Zr, and Co, though after I1, Co was abandoned. The computational load was decrease by bounding the prediction space by nickel content (48 at%. min., 52 at%. max) and single alloying elements (ex. Hf 0-30 at%.). Alloying

elements were grid searched in ternary scheme by 0.1% at. and 1% for quaternary and quinary alloys. Ti bal. was grid searched in 0.1% at. increments. The resulting grid searched predictions were sorted by a combination of highest model confidence, lowest predicted hysteresis, and transformation temperatures then selected for predicted performance and informing un-searched areas of the parameter space.

Fabrication

Samples are fabricated from high purity ingots (minimum 99.95% pure, <100ppm O_2) and weighed to the 0.1mg. Samples masses are determined from an internal atomic percentage to mass calculator and are not used if fractional composition deviates by more than 0.05%, that is a $Ni_{50.1}Ti_{30.5}Hf_{19.4}$ will deviate beyond point of use if the actual atomic composition is $Ni_{50.15}Ti_{30.50}Hf_{19.35}$. Ingot pieces are then mixed and placed in the water-cooled copper crucible for arc melting. A mixing process was determined on experimental success. NiTiHfZr, NiTiHf, or NiTiZr compositions are mixed completely then loaded into the crucible as 2 separate operations. Cu containing compositions are mixed except for the copper which is loaded in a final operation.

Samples are crucible arc melted in an Edmund Buehler arc melter with a 400-amp capacity in a near atmospheric pressure (60 kPa) argon environment, argon purity is 1ppm/vol. Chamber is vacuumed and purge filled with argon a minim of 5 times to 3E-3 torr and a final vacuum to 5E-5 torr prior to melting. Arc melter crucible hole dimensions for the button (5g), 35g scale-up, and 60g scale-up samples are 12mm dia., 40mm x 15mm, and 42mm x 18mm respectfully. Button (5g) samples are melted, flipped, and remelted 1x before loading additional material, and flipped and remelted a

minimum of 5x after all material has been loaded. Large (>30g) samples are similarly mixed but are flipped and remelted 4x after initial loading and melting before additional material is loaded. Ni, Ti, Hf, and Zr can all be mixed with no homogeneity challenges, but it has been observed copper ingots do not fully melt and instead are shielded by the low melting nickel and cannot be completely melted without significant Ni vaporization. Here the copper is melted in a separate crucible hole, flipped and remelted, then added to the larger crucible hole on top to be melted first and homogenize to the larger melt. After the final flip and remelt, large samples set to undergo mechanical processing are resurfaced using a low power arc (< 75 amps) to uniformize the surface. Samples are examined for coloration (indication of oxide) and weighed after removal from the crucible, if the samples are more than 0.1% mass variant from pre-weight, they are deemed invalid for compositional uniformity. This is of upmost importance as the analytical chemistry required to validate a sample to the accuracy needed for transformation temperature variation (0.01% at., <0.05% at. error) does not exist for non-trace alloys in a bulk sample.

Samples accepted after arc melting are cleaned and heat treated for homogenization under argon in quartz allowing heat treatment to occur in a non-vacuum furnace. Homogenization temperature was chosen based on internal processes or literature for similar material groups. Duration for small samples is 24hr, large samples 72hrs. If a sample experienced melting or diffusion, homogenizing temperature was reduced by 50°C and reattempted until successful. In high Zr content and nickel lean compositions it was also found homogenizing at increased duration (96hrs) but in a

vacuum environment in the quarts was effective where argon caused failure. In general, large samples were heat treated 50°C lower than their 5g counterparts, which may affect SME testing but was required to avoid destroyed samples. Heat treatment was followed by an agitated water quench of varying temperatures as an attempt to keep quench rate similar across mass/sample sizes. 5g samples were water (~22°C) quenched, and 35g or larger samples were quenched in ice water (0°C).

After homogenizing button samples were machined via EDM to produce Ø3mm x 1mm discs which can be tested in DSC for transformation temperatures. To avoid diffusion or surface effects, DSC discs are taken a minimum of 0.1mm from an edge surface. After DSC slices are removed, the remaining button sample is the feedstock for splat quenched samples, ~3.5g. The process from mixing, melting, sealing, and heat treating can be followed as a diagram in Figure 13.

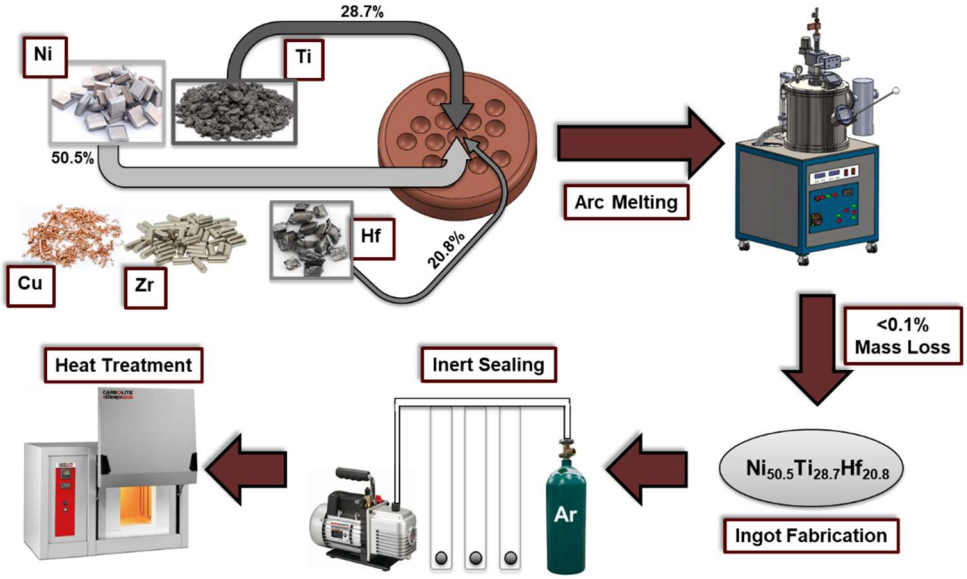

Figure 13: Melting, confirmation and heat treatment processing of SMA materials via crucible arc melting.

After large samples are machined for DSC testing and validated in range (<75°C difference in M_f against 5g sample) they are prepared for canning. Initial scale up testing occurred on compositions from Dr. Umale's unpublished work and were hot forged at homogenization temperature in a 304 stainless steel can made from capping a 1" tube and using 304 plates as shims above and below the sample. Samples were sealed under atmospheric conditions. A disoriented grain structure is prevalent after homogenization, to be suitable for tension testing or for use as actuators shape memory alloys require mechanical grain refinement. In industry this is frequently completed by wire drawing or extrusion to high are reduction factors (90+%) for mechanical performance. Unfortunately, the substantial mass requirements (min. additional order of magnitude) of these processes make these processes for discovery scale fabrication sub-optimal. Based on the size of crucible available in Dr. Karaman's research group and the standard use 26mm x 7.5mm x 1mm tension dogbone (gauge section 8mm), I1 and I2 scaled compositions were melted as either 35g or 60g samples, based on available crucible size. 60g samples were sealed in 1" tube with shims and 35g samples were sealed in 0.75" tube which didn't require shimming. All samples were cleaned and wrapped in a non-diffusing foil, then encased in a powdered getter material to avoid oxygen contamination. It was hypothesized and validated that the furnace heating of the sample would cause the getter to heat first, bonding to any excess oxygen and reducing oxygen contamination during mechanical processing.

The forging process uses a high force plunger to work the sample to a shimmed limit point. Because the force of the plunger eventually breaks down the shim there was

low confidence in uniform directional strain/processing across multiple samples which would ultimately be mechanically compared to one another for performance. Therefore, I1 and I2 selected compositions were processed to 50% sample area reduction by hot rolling.

Hot rolling occurred on a dual driven 6” drum roller. The lower roller was heated with a 1300W heat gun and were also pre-heated by sample temperature stainless-steel blocks passed through the rollers before the sample. The roller temperature increased the by as much as 200°C above ambient. This process significantly reduced undercooling the canned SMA would experience. Furnace temperature was set to the highest temperature (in 50°C increments) that did not result in liquid phases in each alloy. This is experimentally determined in conjunction with CALPHAD and ranged from 100°-200°C below homogenization temperature. In many cases this was above the solutionization temperature for the alloy in an attempt to avoid growth of additional phases.

Processing began with a 30-minute heat soak, after removal from the furnace cans were passed through the rollers after and reduced by 0.5mm or 3.5%, whichever was smaller. The goal being a uniform 3.5% reduction per step. These were experimentally optimized values to allow hot working of even brittle HTSMAs. Cans were measured via caliper after each rolling step and re-heated for 10 minutes before reducing the roller distance and repeating the process. If significant sample curling occurred, samples were passed through the previous die distance a second time, at a 45° angle. After final thickness was achieved, samples were soaked for 5 minutes in the

furnace and ice quenched with agitation. Sample thickness cannot be directly measured until processing is complete. It was experimentally determined to achieve a sample reduction of 50%, a 70% can reduction was needed. The stepwise rolling schedule for a $Ni_{50.3}Ti_{29.2}Hf_{20.5}$ is viewable in Table 2.

Table 2: $Ni_{50.3}Ti_{29.2}Hf_{20.5}$ Hot Rolling Schedule

Cycle	Initial (in)	Final (in)	Step(in)	R-est. (%)	Part T(in)	Redux. (in)	Redux (mm)	R (%)
0	1.001	0.981	0.020	2.00%	0.971	0.030	0.762	3.00%
1	0.981	0.961	0.020	2.04%	0.951	0.020	0.508	2.06%
2	0.961	0.941	0.020	2.08%	0.933	0.018	0.457	1.89%
3	0.941	0.921	0.020	2.13%	0.915	0.018	0.457	1.93%
4	0.921	0.901	0.020	2.17%	0.893	0.022	0.559	2.40%
5	0.901	0.881	0.020	2.22%	0.874	0.019	0.483	2.13%
6	0.881	0.861	0.020	2.27%	0.851	0.023	0.584	2.63%
7	0.861	0.841	0.020	2.32%	0.834	0.017	0.432	2.00%
8	0.841	0.821	0.020	2.38%	0.814	0.020	0.508	2.40%
9	0.821	0.801	0.020	2.44%	0.799	0.015	0.381	1.84%
10	0.801	0.781	0.020	2.50%	0.777	0.022	0.559	2.75%
11	0.781	0.761	0.020	2.56%	0.759	0.018	0.457	2.32%
12	0.761	0.741	0.020	2.63%	0.740	0.019	0.483	2.50%
13	0.741	0.721	0.020	2.70%	0.722	0.018	0.457	2.43%
14	0.721	0.701	0.020	2.77%	0.700	0.022	0.559	3.05%
15	0.701	0.681	0.020	2.85%	0.682	0.018	0.457	2.57%
16	0.681	0.661	0.020	2.94%	0.654	0.028	0.711	4.11%
17	0.661	0.641	0.020	3.03%	0.635	0.019	0.483	2.91%
18	0.641	0.621	0.020	3.12%	0.614	0.021	0.533	3.31%
19	0.621	0.601	0.020	3.22%	0.603	0.011	0.279	1.79%
20	0.601	0.581	0.020	3.33%	0.579	0.024	0.610	3.98%
21	0.581	0.561	0.020	3.44%	0.555	0.024	0.610	4.15%
22	0.561	0.542	0.019	3.39%	0.535	0.020	0.508	3.60%
23	0.542	0.523	0.019	3.51%	0.512	0.023	0.584	4.30%
24	0.523	0.505	0.018	3.44%	0.496	0.016	0.406	3.13%
25	0.505	0.488	0.017	3.37%	0.479	0.017	0.432	3.43%
26	0.488	0.471	0.017	3.48%	0.461	0.018	0.457	3.76%
27	0.471	0.455	0.016	3.40%	0.442	0.019	0.483	4.12%
28	0.455	0.439	0.016	3.52%	0.423	0.019	0.483	4.30%
29	0.439	0.424	0.015	3.42%	0.410	0.013	0.330	3.07%
30	0.424	0.409	0.015	3.54%	0.395	0.015	0.381	3.66%
31	0.409	0.395	0.014	3.42%	0.382	0.013	0.330	3.29%

Continued: Table 3: $Ni_{50.3}Ti_{29.2}Hf_{20.5}$ Hot Rolling Schedule

Cycle	Initial (in)	Final (in)	Step(in)	R-est. (%)	Part T(in)	Redux. (in)	Redux (mm)	R (%)
32	0.395	0.382	0.013	3.29%	0.369	0.013	0.330	3.40%
33	0.382	0.369	0.013	3.40%	0.354	0.015	0.381	4.07%
34	0.369	0.356	0.013	3.52%	0.348	0.006	0.152	1.69%
35	0.356	0.344	0.012	3.37%	0.335	0.013	0.330	3.74%
36	0.344	0.332	0.012	3.49%	0.323	0.012	0.305	3.58%
37	0.332	0.321	0.011	3.31%	0.311	0.012	0.305	3.72%
38	0.321	0.310	0.011	3.43%	0.304	0.007	0.178	2.25%
39	0.310	0.300	0.010	3.23%	0.298	0.006	0.152	1.97%

Columns left of ‘R (in)’ are calculated estimations for designing the rolling schedule, whereas all columns to the right are the actual stepwise reduction of the sample can. In the shimmed 1” tubes there is a single step 0 to solidify the getter material and force complete material flow. Before the getter solidified the SMA will not feel enough force to overcome shear. In ¾” tubes where the getter occupied space is larger, 3 steps initial steps are used to solidify where the 3.5% reduction percentage is ignored.

Rolled samples were removed from the can with Dremel cutoff wheels allowing separation of the can without overheating the sample inside to transformation. Depending on rolling temperature the powdered getter material will have sintered together or solidified completely. It is either cut with a Dremel cutoff wheel or a mechanical saw to free the HTSMA from inside. Cutoff wheels, especially on a 4" die grinder, create a significant amount of heat and may cause transformation in a sample if the cutting is not completed with patience and care. The foil wrap prevents the material from becoming a monolith where diffusion would invalidate the samples chemistry.

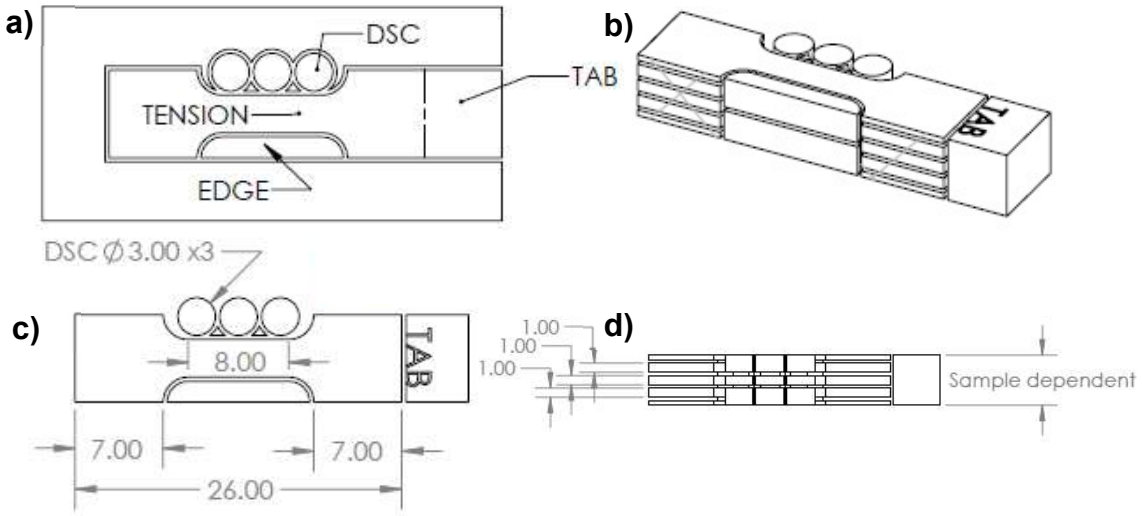

Figure 14: Hot rolled HTSMA Cut plan, **a)** EDM operation 1 for arbitrary sample size, **b)** reconstruction after all cutting including cross hatching to ensure sample locating is possible, **c)** post OP1 sample dimensions, **d)** tension sample thickness, maximize samples based on rolled thickness

Rolled samples are then inspected, measured, and machined by EDM for DSC samples, tension specimens, and SEM samples to observe the cross section and top view nearest the tensile samples' gauge section. Other cutting patters have been made to gather XRD or compression samples. The current 35g DSC cutting pathways shown in Figure 14 which results in a minimum of 3 tension samples, ideally 4, with the ability to

reconstruct as-rolled geometry to inform SEM imaged or DSC to location variant results. 60g samples resulted in 2 tension sample stacks, butted lengthwise resulting in 2 sets of 3 tension profiles, though the possibility of variation between the two tension stacks and speed drove the research team to process two separate 35g samples if 6 tension specimens were needed.

Shape Memory Effect Testing

All samples successfully fabricated and heat treated; mechanically worked, or secondary heat treated, underwent DSC testing in accordance with ASTM F2004 to measure transformation temperatures [132]. Button samples that did not have existing transformation data were tested from -50°C to 400°C to ensure effective undercooling to fully transform the martensitic phase but to avoid higher temperature soaking which may promote h-phase formation during testing. Samples were run at the Soft Matter Facility at Texas A&M University on a TA DSC2500 with a flange temperature of -80°C and a 50ml gas purge rate at a temperature cycle rate of 10°C/min on heating and cooling with 1 minute held isothermally at the end of each cycle. Cycles were performed twice per sample, with the second ‘stable’ cycle being the one reported in all data here unless otherwise stated. A complete dataset of interest will be included with any published works and is available in Appendix C, specifically to encourage and enable ML based future investigations.

Uniaxial constant force thermal cycling (UCFTC) tests were completed as near as possible to ASTM 3097 on 1mm thick tensile samples with an 8mm gauge section and a 3mm waist width. A standard cycle and values of quantities of interest are visible

in Figure 15, copied from the standard. Specimens were loaded into pin grips in an MTS hydraulic tension machine with a 10kN load cell. Strain was measured by a ½" MTS extensometer with alumina contact tips which measure -10% to +20% strain and at test start fully encapsulated the transforming gauge section. Sample temperature was taken by a mechanically attached thermocouple in the center of the gauge section. Grip temperatures were measured by thermocouple and controlled by PID communicating

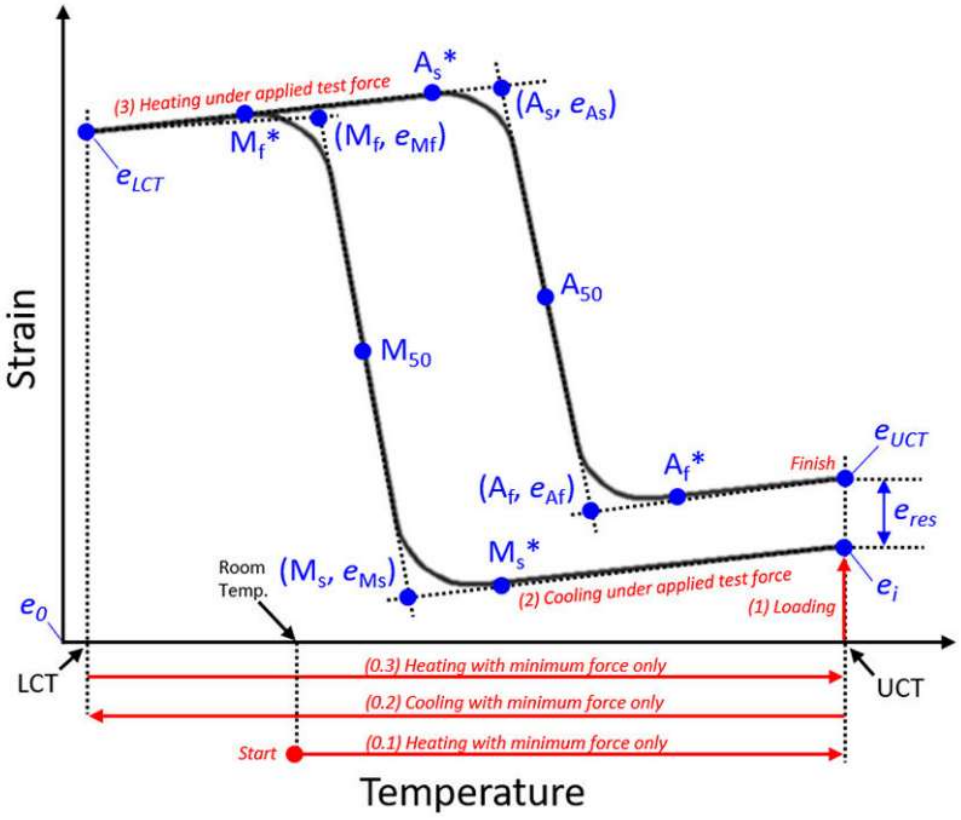

Figure 15: Reference UCFTC cycle at a static arbitrary load for testing mechanical response of shape memory alloys, from [7]

with MTS testing software. The PID controllers were tuned to optimization at 400°C based on the thermocouple at the intersection between grip base and shaft. The experimental setup was wrapped in ceramic insulation to decrease the influence of the

ambient (~22°C) environment. Heating occurred via 300W induction heating collars over copper tubing wrapped tightly around the tension grip between the sample and cylinder/load cell on the bottom/top respectively. The original setup was capable of 400°C sample testing, in contributions the author will discuss an update to the heating elements, grips, and cooling jacket to allow for safe operation to above 600°C, though it has no influence on the testing process.

Testing deviated from ASTM 3097 in control rate. It was found operating the system at 10°C/min violated the requirement that the gauge section have no larger than 3°C gradient. Therefore, the tested heating rate here was 4°C/min and cooled at 7°C/min. Loads tested were 5MPa (normalization), 50MPa, 100MPa, 150MPa, 200MPa, 300MPa, 400MPa, 500MPa, and 600MPA. Tests were reduced in scope if transformation did not fully occur between LCT and UCT as noted in ASTM 3097. $LCT = M_f - 50°C$ and $UCT = A_f + 100°C$ as determined by DSC for as hot rolled samples. For samples with secondary heat treatment, $LCT = M_f - 30°C$ and $UCT = A_f + 150°C$ or $400°C$, whichever was lower. If transformation did not fully occur between upper and lower cycle temperatures the cycle was considered invalid. In accordance with ASTM 3097 this experimentation will report calculated transformation temperatures, actuation strain, cooling transformation strain, heating transformation strain, thermal transformation span, and hysteresis width. Top performing alloys to validate for additive manufacturing will be chosen based on the pareto front of minimum hysteresis and maximum actuation strain. Additional considerations are transformation temperatures at load, irrecoverable strain at load, and cost of material.

Powderless Validation for PBF AM

The cost of one novel atomized powder composition forces a creative approach to further reduce the highest performing materials by how compliant they are to additive manufacturing. Compliance to additive can be broken down broadly to mean a material can be rapidly solidified, i.e. no micro or macro cracks caused from residual stress or uneven solidification fronts, lack of dendritic wetting, or intermetallic phases which would cause failure. While parts fabricated by additive can be heat treated to eliminate sub-optimal phases or precipitate strengthening phases, these often require significant additional processing and should be considered detractors to a materials viability. Finally, and this is novel to SMAs, the preferential vaporization of nickel in the melt pool should not cause it to fall out of the operating window of the shape memory effect. Specifically, nickel matrix reduction due to vaporization should not raise the transformation temperatures beyond the temperature range of interest. Based on literature it is also apparent that all NiTi based SMAs are extremely susceptible to oxygen, and what fraction of successful but sub-optimal SME response or failed builds in additive are a fault of poor environmental control is unknown. Therefore, it is proposed that testing solidification speed (ideally $> 1E6$°C/s) in a highly pure environment can act as a no-go gauge for additive development if the microstructure across solidification speeds proves undesirable. This was achieved with splat quenching. After eliminating high performing systems considered unacceptable, physics informed simulations can be used to find a single final composition to scale up and laser or electron-beam weld into a substrate of known composition.

Splat Quenching

Splat quenching was completed by The Brewer group at University of Alabama. The samples sent were the remainder of the 5g button samples from successfully UCFTC tested materials at the time. This did not include the second group of I2-L samples. The process of splat quenching requires a goal overheat temperature, estimated via CALPHAD, which is achieved by induction melting. The molten droplet is impacted by two room temperature (or undercooled) plates which rapidly pull temperature away. The impact process results in distinct sections of cooling-rate dependent microstructure which can be examined by qualitative SEM performed on the cross section of the splat.

Splats received by UA must have the highest care paid to avoid mechanical deformation which would twin, and therefore change, the microstructure of the samples. Splats were mounted in epoxy, cross sectioned along a centerline crossing as close as possible to the center of the spalt to allow variation in solidification rate to be examined under SEM. $Ni_{51.2}Ti$ was used as a test composition. After charging issues were discovered in SEM the remaining splats were mounted in slow cure epoxy impregnated with equal weight conductive particles and mounted in a holder designed to allow epoxy to touch and solidify against the splat without deforming the sample.

In SEM BSE microstructures were compared to L-PBF SMA literature to determine grain size correlated to solidification morphology of AM. Additional items of interest are cracking, non-uniform solidification, deleterious phases, strengthening phases, and any apparent matches to L-PBF fabricated microstructures. The SEM used was an FEI Quanta in conjunction with Texas A&M's image and microscopy center.

The selected area will undergo FIB lift-out and prep for TEM investigation. TEM will be performed on the splat quenched samples to learn more about the structure of multi-component shape memory alloys. Specifically, if they are a uniform B19' monoclinic martensite or if in solidification there is fractions of retained austenite (B2) or if B19 orthorhombic phase occurs.

Physics Informed L-PBF Modeling

To further reduce the number of high performing materials to one for final substrate fabrication, physics informed printability map modeling may be utilized. Performed by Sofia Sheikh in Dr. Arroyave's group if she has an interest in collaborating, such maps could indicate an improvement in printability with additional alloying elements or the impact of a particular alloy richness on 'good' build region.

Energy Source to Substrate

In both L-PBF and EB-PBF a printability map can be explored by depositing energy directly into a substrate which has tight compositional control over. EB-PBF not having the same reflectivity index as L-PBF rendering physics informed printability maps far from 1:1, though there have already been some analog studies on comparing printability maps across the machine spaces. In addition, EB-PBF is completely free from oxygen, which would allow investigation into materials that in literature may have failed but could have done so not because of poor process parameter control but because of poor environmental control. Additionally, with a comparable L-PBF substrate and process parameter setting, line WDS could be performed from the substrate into the melt pool indicating differences in elemental vaporization between the processes. It is

hypothesized that without a gas atmosphere the vaporization effects seen in L-PBF of NiTi would be even more pronounced if it is associated with vaporization and not the development of very small nickel rich phases as a function of rapid solidification.

By examining chemical variation between the substrate and the melt pool for L-PBF and EB-PBF single or hatch cross sections the vaporization of individual elements may be assessable. This would allow for an overlap of a printability map with estimated composition and therefore transformation temperatures (if known). A Frenzel curve [133] could then be constructed whereby varying vaporized elements the transformation temperatures across the printability map could be assessed.

Experimentation will be limited based on machine availability and time, EB-PBF would be performed on the Freemelt One in the MSEN department whereas L-PBF requires the IPG at KCSNC. The IPG has extremely tight environmental control (<10ppm O_2 indicated) enabling SMA investigation.

At the time of writing, only simulation has been completed with any on-machine operation or Ni-richness curve development to occur after defense of this thesis.

CHAPTER III

RESULTS AND DISCUSSION

The objectives set by the sponsoring organization were to develop a composition to meet a specific transformation criterion and maximize actuation strain in line or above 3% near upper limit observed in non-PGM containing HTSMAs. After confirmation of performance high performance materials would be down selected for rapid solidification investigation. At the time of this thesis splat quenched samples were fabricated and investigated, however, bead-on-plate, hatch-on-plate, or nickel evaporation/richness transformation variation was not explored for any individual composition.

All compositions chosen and tested to the best of the authors and collaborators knowledge represent never published material compositions which are tested here to develop a performance pareto front in an under investigated compositional space of HTSMAs. The initial discovery phase whereby button samples (5g) were used to test transformation temperatures was extremely successful, with 10 compositions having transformation temperatures in the initial target range (200°C-300°C) and 28 compositions transforming in the relaxed range (175°C-325°C range)

Down-selected compositions were successfully enlarged to 35g (or larger) and successfully mechanically worked resulting in testable tension samples with small (<30°C) deviations in transformation temperature to their discovery counterparts. This represents a highly successful effort in mechanical processing of low ductility materials with high oxygen affinity. After heat treatment the pareto front of IBHC results show a

marked improvement from any existing data in literature for transformations above 200°C without PGMs, validating the global success of this work.

Modeling and Rapid Discovery

Prior to developing a model, 3 'backup' compositions were selected from unpublished compositions from Dr. Tejas Umale's NiTiHf experimental work. The alloys $Ni_{50.3}Ti_{28.9}Hf_{20.8}$, $Ni_{50.2}Ti_{29.1}Hf_{20.7}$, and $Ni_{50.1}Ti_{30.4}Hf_{19.5}$ transformed within the 200°C-300°C temperature range of interest at 5g sample size but did not have existing literature or tests on mechanical properties. They are included as stars in the pareto front as the 60g scale up of the material still represents independent work in association with this effort.

Iteration 1

John Broucek took lead in developing Dr. Trehern's DNN for the are of interest. The two models for each composition are then compared and the overall confidence of the model is output as a standard deviation on the prediction criterion. The model was trained for A_f, M_s, M_f, and calculated hysteresis. After iterating through data cleaning to increase accuracy of model but avoid overfitting the DNN was completed. One returned train validation including statistical significance for the values of interest is shown in Figure 16.

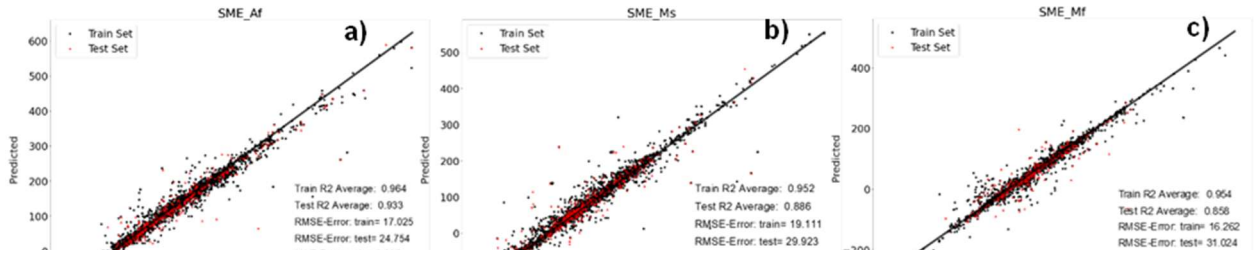

Figure 16: Test vs train transformation temperature correlation for modeled shape memory effect on materials containing any combination of Ni, Ti, Hf, or Zr; **a)** A_f, **b)** M_s, **c)** M_f,

The training set R^2 of the data is above .950 which indicates a tight ability to train to the model, which is a highlight of the DNN model type, however, they are also prone to overtraining. The resulting test R^2 of none of the predicted transformation temperatures reaching above 0.90 indicates either outlying data, which can be seen scattered through either graphs, or some other factor not fully captured by the model that influences transformation temperatures. There are several factors that could be at fault including uncaptured physics quantities, inaccurately reported data, incorrect database entries, or errant literature data that was not removed. Considering the research goal here is not to develop an ideal model but rather to engineer and test novel materials, a perfectly accurate model prediction was not a requirement. Rather it was used to inform searching in iteration 1.

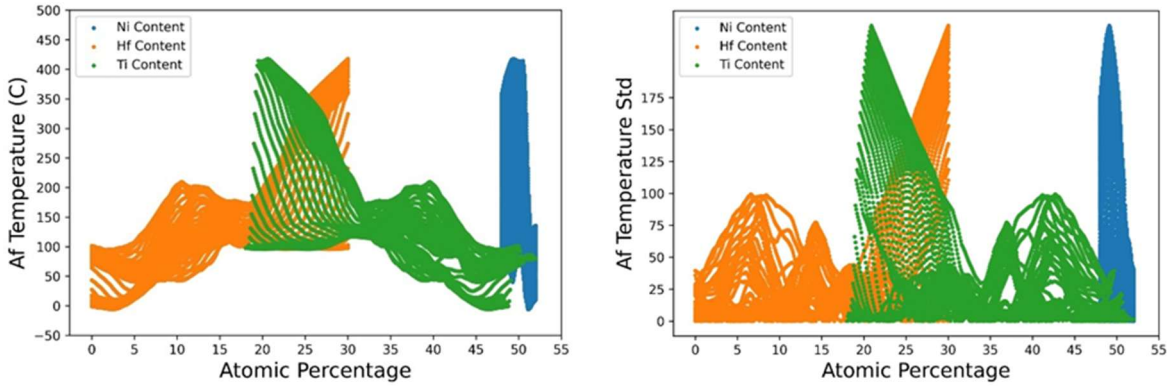

Figure 17: a) Model predicted A_f temperature, **b)** multi-model standard deviation (estimated confidence) vs atomic percentage of composition

In Figure 17 predicted A_f temperature and standard deviation (anticipated prediction accuracy) for the NiTiHf grid system are shown for the over 13,000 points of prediction. The stratification of data can look extremely busy however in the larger

quaternary and quinary datasets individual points are nearly indistinguishable. Analysis began by ensuring that the predicted outcomes followed intuitively with literature and known trends, i.e. increasing hafnium content results in increasing A_f temperature approaching or exceeding 400°C in nickel lean compositions. Interestingly there are also values of $Ni_xTi_yHf_{30}$ which appear to have an A_f of only 100°C. This is not out of the realm of possibility for very nickel rich compositions, however a result below 0°C would be a reason for pause. In the grid system the minimum predicted hysteresis was 0°C after removing negative hysteresis calculations which indicate the model is not capturing whatever feature physics or microstructure prevents HTSMAs from near zero hysteresis achieved by lower temperature SMAs like the NiTiCu system. These results are indicative of broader results when stepping through each grid search.

Considering Figure 17 b) the confidence level of the models, that is the agreement between n=2 model individual prediction is near zero for certain compositions and extremely large elsewhere. This indicates a large compositional space has not been explored in the literature and the predictions based on known composition transformation cannot be exploited to a high degree of confidence. The temperature data trends, current model confidence, and the first set of materials being able to retrain and increase model performance it was determined that iteration 1 would be a combination of stepwise searching the unexplored composition space (NiTiHfZr, NiTiZr, NiTiCuHf, NiTiCuHfZr, NiTiCo), with 18 5g model-based alloys which had high confidence and low predicted hysteresis and an additional 4 alloys that were predicted simultaneously by two models and would be produced under the DMREF 60g effort but report here in parallel.

The resulting I1 composition set is included in Table 4**.** An expanded Table including final transformation temperatures, durations, and tested transformation temperatures will be included in Appendix B.

Table 4: Determined alloys for Iteration 1 fabrication

Ni (%at.)	Ti (%at.)	Cu (%at.)	Hf (%at.)	Zr (%at.)	Co (%at.)	Model
50.3	26.3	-	23.4	-	-	1
50.6	22.9	-	26.5	-	-	1
50.4	24.9	-	24.7	-	-	1
50.5	23.8	-	25.7	-	-	1
50	28.8	-	21.2	-	-	1
49.9	29.4	-	20.7	-	-	1
49.9	29	-	21.1	-	-	1
50	28.5	-	21.5	-	-	1
48.9	31.1	-	20	-	-	1
48.9	31.1	-	-	20	-	1
49.7	27.6	0	0	22.7	-	1
49.9	28.9	0	0	21.2	-	1
41.7	25.6	8.5	24.2	0	-	1
48.2	29.2	0.7	0	21.9	-	1
48.8	30.9	1.2	0	19.1	-	1
45.4	27.7	5.1	10.9	10.9	-	1
45.1	26.5	5.6	11.4	11.4	-	1
46.9	27.7	3.6	10.9	10.9	-	1
39.2	22.8	11	27	-	-	1
33.7	21.3	16	29	-	-	1
35.9	22.1	14	28	-	-	1
36.1	21.9	14	28	-	-	1
50.3	29.7	-	0	20	-	0
50.3	28.7	-	0	21	-	0
50.3	27.7	-	0	22	-	0
50.3	26.7	-	0	23	-	0
50.6	29.4	-	0	20	-	0
50.6	28.4	-	0	21	-	0
50.6	27.4	-	0	22	-	0
50.6	26.4	-	0	23	-	0
50.8	27.2	-	0	22	-	0
50.8	26.2	-	0	23	-	0
50.8	25.2	-	0	24	-	0
50.3	29.7	-	10	10	-	0
50.3	28.7	-	10.5	10.5	-	0
50.3	27.7	-	11	11	-	0
50.6	28.4	-	10.5	10.5	-	0
50.6	27.4	-	11	11	-	0
50.6	26.4	-	11.5	11.5	-	0
50.8	27.2	-	11	11	-	0
50.8	26.2	-	11.5	11.5	-	0
50.8	25.2	-	12	12	-	0

Continued: Table 5: Determined alloys for Iteration 1 fabrication

Ni (%at.)	Ti (%at.)	Cu (%at.)	Hf (%at.)	Zr (%at.)	Co (%at.)	Model
50.8	24.2	-	12.5	12.5	-	0
45.3	29.7	-	10	10	-	0
45.3	28.7	-	10.5	10.5	-	0
45.3	27.7	-	11	11	-	0
40.3	29.7	-	10	10	-	0
40.3	28.7	-	10.5	10.5	-	0
40.3	27.7	-	11	11	-	0
45.6	28.4	-	10.5	10.5	-	0
45.6	27.4	-	11	11	-	0
45.6	26.4	-	11.5	11.5	-	0
40.6	28.4	-	10.5	10.5	-	0
40.6	27.4	10	11	11	-	0
40.6	26.4	10	11.5	11.5	-	0
45.8	27.2	5	11	11	-	0
45.8	26.2	5	11.5	11.5	-	0
45.8	25.2	5	12	12	-	0
45.8	24.2	5	12.5	12.5	-	0
40.8	27.2	10	11	11	-	0
40.8	26.2	10	11.5	11.5	-	0
40.8	25.2	10	12	12	-	0
40.8	24.2	10	12.5	12.5	-	0
49	50	-	-	-	1	0
48	50	-	-	-	2	0
47	50	-	-	-	3	0
46	50	-	-	-	4	0
45	50	-	-	-	5	0
44	50	-	-	-	6	0
50.3	28.9	-	20.8	-	-	U
50.1	30.4	-	19.5	-	-	U
50.2	29.1	-	20.7	-	-	U

After selection, iteration 1 materials were fabricated and tested via arc melting, heat treatment, EDM cutting and DSC as outlined previously. The stable transformations (DSC cycle 2) data is shown in Figure 18 as a scatterplot including the resulting transformation temperatures against the range of interest set by the sponsoring agency (200°C-300°C). Notable negative takeaways include a lack of very clear pareto front,

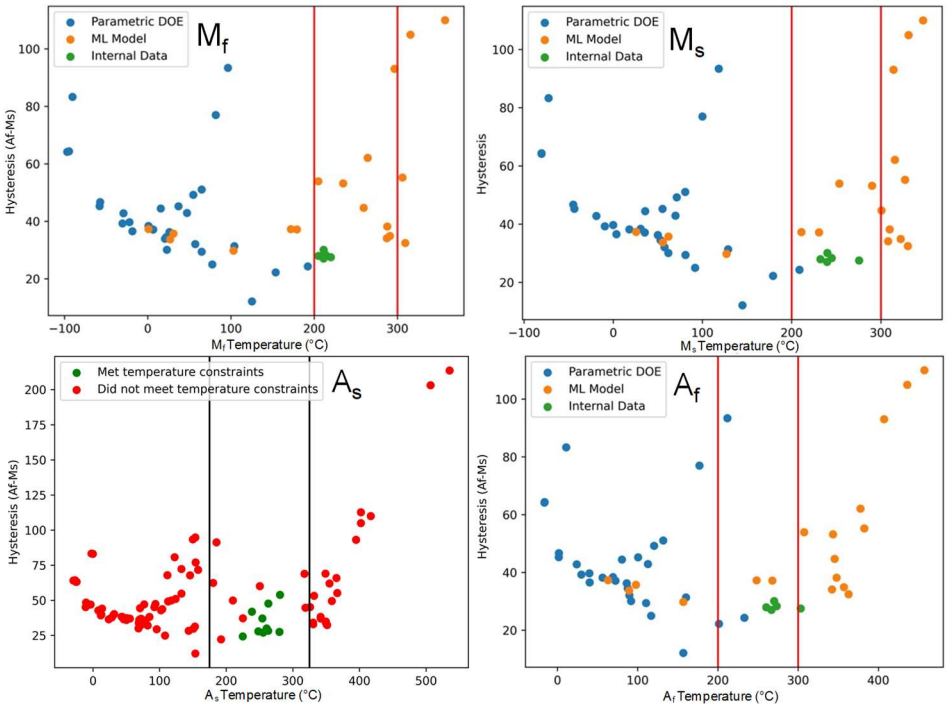

Figure 18: Recorded transformation temperatures with windows of interest for Iteration 1, M_f, M_s, A_f and A_s. A_s includes relaxed constraints (175° – 325°C range and is color coded for successful compositions

likely from stepwise processing rather than model reliance. Additionally, more than 50% of alloys had hysteresis values below 40°C which would mark a significant improvement if they were high temperature alloys, however where $A_f < 100$°C as is visible in the bottom right plot, there are hundreds of literature reported alloys which have hysteresis below the apparent curve. Taken together, the need for a second iteration is plain.

I1 was highly successful in informing areas that had not been previously investigated to improve the model for I2. Two NiTiHfZr alloys showcased <25°C hysteresis with one result being 12°C though was not repeatable even when refabricated. The alloys were out of transformation range of even the relaxed constraints however were chosen for scale up to explore mechanical variation in NiTiHfZr to NiTiHf alloys. Two of the 'backup' alloys scaled from Dr. Umale's exploratory hafnium work successfully transformed within constraints. The 4 points of data are from two alloys after homogenizing heat treatment, and $Ni_{50.3}Ti_{28.9}Hf_{20.8}$ in both the as forged and solution heat treated state. In the as forged condition, which was processed and prepared for tension, the alloys measured hysteresis by DSC was 27.02°C, the lowest hysteresis for a non-PGM containing HTSMA with $A_f > 200℃$.

Considering there were no developed alloys that met the original constraints, the sponsor provided relaxed constraints (±25°C) to extend transformation range to 175°C-325°C. Under this change, 4 developed compositions, 3 model predicted and 1 from the parametric DOE in iteration 1 met requirements: $Ni_{50.3}Ti_{28.7}(HfZr)_{21}$, $Ni_{49.9}Ti_{28.9}Hf_{21.2}$, $Ni_{48.9}Ti_{31}Hf_{20}$, and $Ni_{41.7}Cu_{8.5}Ti_{25.6}Hf_{24.2}$. Compositions of note were quaternary compositions $Ni_{50.3}Ti_{29.7}(HfZr)_{20}$, and $Ni_{50.3}Ti_{28.7}(HfZr)_{21}$, which had transformation temperatures below or on the very low end the KCNSC threshold however had improved and comparable hysteresis, respectively, when compared to as homogenized $Ni_{50.3}Ti_{28.9}Hf_{20}$. It has been shown in the AM literature high VED process parameters able to fuse with high density raise transformation temperatures in as-built composition compared to a traditionally fabricated alloy of the same composition as the

feedstock powder. This indicates bulk material below the transformational temperature threshold may be fabricated into KCSNC transformation range in L-PBF. However, that is more of a compromise than an engineered solution. Varying process parameters for transformational control would also need to be informed by investigating transformation temperature variation with nickel richness on a curve around an atomized powder composition to discreetly describe chemistry variation. It is also worth mentioning since Ni content is above 50.3 at.% these compositions would be readily form h-phase for optimized performance and likely see an increase in transformation temperatures as a result.

Other compositions within bounds, $Ni_{49.9}Ti_{28.9}Hf_{21.2}$ and $Ni_{48.9}Ti_{31.1}Hf_{20}$, were originally disfavored for atomization for low nickel contents since high rich compositions have been shown to be viable in L-PBF over a range of VED's it is not known whether a Ni-lean composition can be forced out of transformation conditions by laser power, though that is a hypothesized possibility. $Ni_{41.7}Cu_{8.5}Ti_{25.6}Hf_{24.2}$ represents an additional challenge in complexity since it adds an element (Cu) that has not been fabricated in L-PBF NiTi literature. After the transition from atomization to AM analogs all compositions were considered valid and considered for I3 scale up.

Other iteration 1 results include an interesting trend in the NiTiHf data shown in Figure 19. Where it appears the A_f temperature follows a linear trajectory with increasing Hf content even with an increase of atomic Ni in the system which in binary NiTi depresses transformation temperature. In addition, the hysteresis of the alloys in the system seem to decline nearing 22% at. Hf then increase, again, seemingly independent

of Ni richness. This warrants further consideration, especially if the Hf(at%) vs Af can be depressed to bring the transformation temperatures within range of the KCNSC requirements.

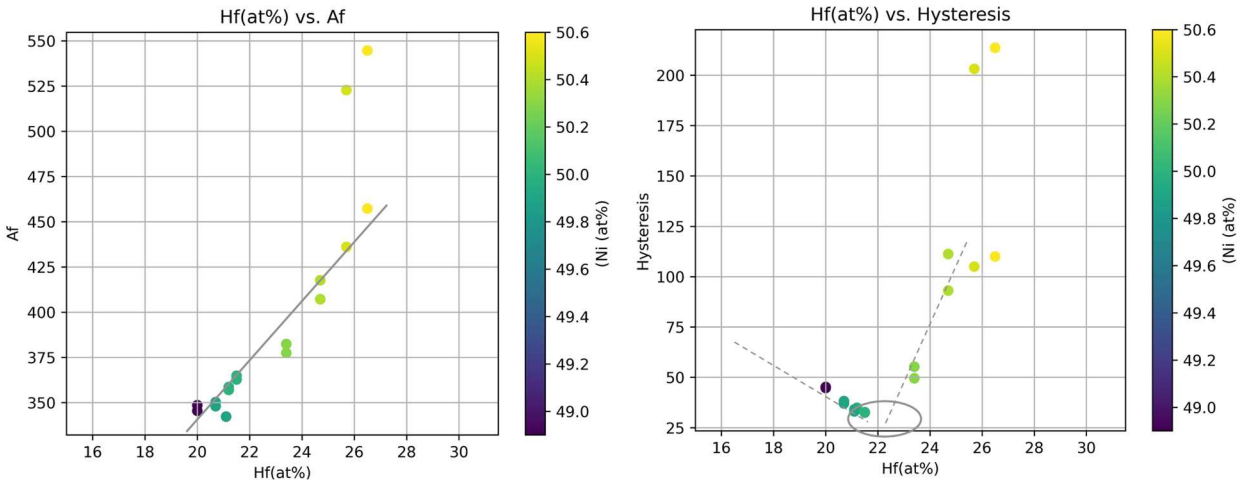

Figure 19: Visible trends from transformation temperatures in the NiTiHf system, specifically apparent indifference to Ni Content for transformation temperature and a minimization point in hysteresis when varied by Hf content

Iteration 2

Iteration 2 was also selected again based on a combination of estimated high performance materials from the DNN model and informed exploration. At the time of selection in I2, Cu was considered an additional challenge to the atomization and L-PBF process so was not explored further. In addition, the Hf trends where transformation temperatures appeared to increase independent of Ni-content was worth testing, so I2 increased Ni-content search with 50.6% at. and 50.8% Ni alloys. It was hoped that the literature indicates a decrease in hysteresis in Ni-rich materials and the possibility of H-phase precipitation would enable strengthening for mechanical testing. NiTiHfZr was

also checked stepwise in high Ni-content alloys searching for a combination that would hold the relatively low hysteresis noted in I1 while increasing transformation temperatures. The novel compositions (excluding I1 scale ups) are in Table 6. Again, full transformation data is included in the appendix section.

Table 6: I2 novel compositions

Ni (%at.)	Ti (%at.)	Hf (%at.)	Zr (%at.)	Model
50.4	27.2	22.4	-	1
50.2	28.7	21.1	-	1
50.4	26.8	22.8	-	1
50.3	27.4	22.3	-	1
50.2	27.7	22.1	-	1
50.4	26.5	23.1	-	1
50.2	27.6	22.2	-	1
49.9	28.1	22	-	1
49.9	28	22.1	-	1
50.4	26.2	23.4	-	1
50	27.4	11.3	11.3	1
50.1	28.7	10.6	10.6	1
50.1	28.3	10.8	10.8	1
50.1	27.9	11	11	1
50.1	27.5	11.2	11.2	1
50.1	26.9	11.5	11.5	1
50.1	25.9	12	12	1
50.2	27	11.4	11.4	1
50.3	29.2	20.5	-	1
50.3	28.7	21	-	0
50.3	28.2	21.5	-	0
50.3	27.7	22	-	0
50.3	27.2	22.5	-	0
50.3	26.7	23	-	0
50.6	28.9	20.5	-	0
50.6	28.4	21	-	0
50.6	27.9	21.5	-	0
50.6	27.4	22	-	0
50.6	26.9	22.5	-	0
50.6	26.4	23	-	0
50.8	28.7	20.5	-	0
50.8	28.2	21	-	0
50.8	27.7	21.5	-	0
50.8	27.2	22	-	0
50.8	26.7	22.5	-	0
50.8	26.2	23	-	0
50	30	-	20	0

Continued: Table 7: I2 novel compositions

Ni (%at.)	Ti (%at.)	Hf (%at.)	Zr (%at.)	Model
50	29	-	21	0
50	28	-	22	0
50	30	10	10	0
50	29	10.5	10.5	0
50	28	11	11	0
50	27	11.5	11.5	0
50.2	29.8	10	10	0
50.2	28.8	10.5	10.5	0
50.2	27.8	11	11	0
50.2	26.8	11.5	11.5	0
50.3	26.7	11.5	11.5	0
50.5	0	29.5	10	10
50.5	0	28.5	10.5	10.5
50.5	0	27.5	11	11
50.5	0	26.5	11.5	11.5

Iteration 2 also contained enlarged samples of 4 selected compositions from I1 which were prepared for UCFTC testing. All samples were processed similarly to iteration 1, arc melted, homogenized, and tested for 2 cycles in DSC. The results from iteration 2 are in Figure 20**.** There is a significant improvement in the lower hysteresis limit generated from the leading edge of the scatter data indicating an improvement in the pareto front. Iteration 2 resulted in 10 compositions that successfully transformed

within the original 200° – 300°C transformation range and brought the total tested alloys within the extended range to 28. Between both iterations the complete sample set is less than 140 alloys which, apart from Dr. Umale's, have never been fabricated with reported testing before. This represents a minimum of a 7.2% success rate for the original

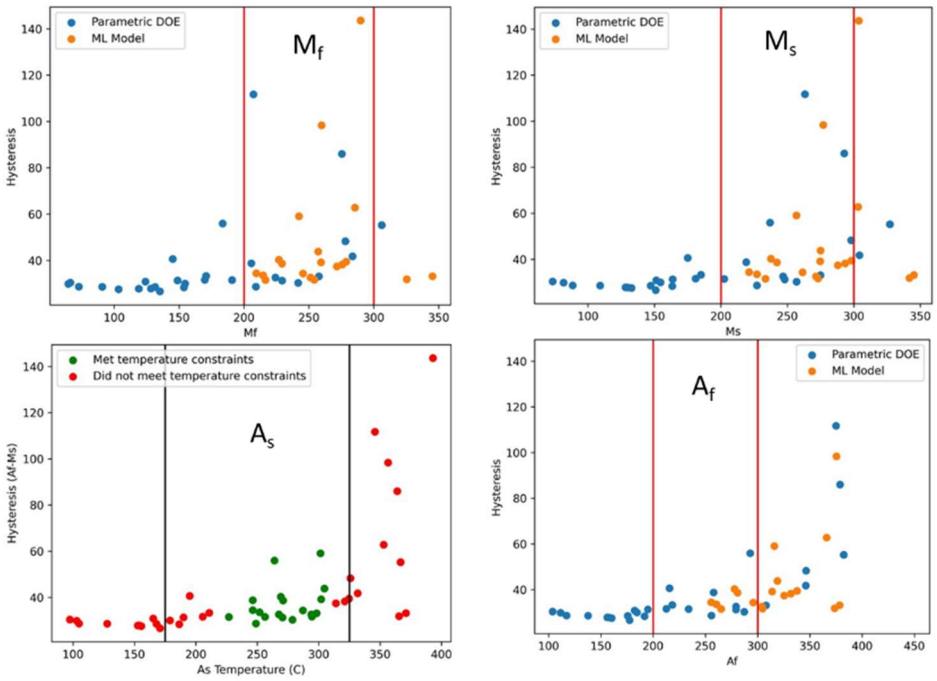

Figure 20: Transformation data collected for iteration 2 compositions

arbitrary 200° – 300°C transformation range, and a minimum 20% success rate for the relaxed range. All alloys that met the relaxed transformation range requirements (175° – 325°C) were considered for scale up in I3.

The combined pareto front through discovery iterations (I1/I2) is included in Figure 21 including showing which compositions were scaled by the end of I2 as marked

by a black circle at datapoint center. Note Figure 19 (a) includes a larger hysteresis range to capture the entire dataset whereas (b) focuses on low hysteresis differentiation.

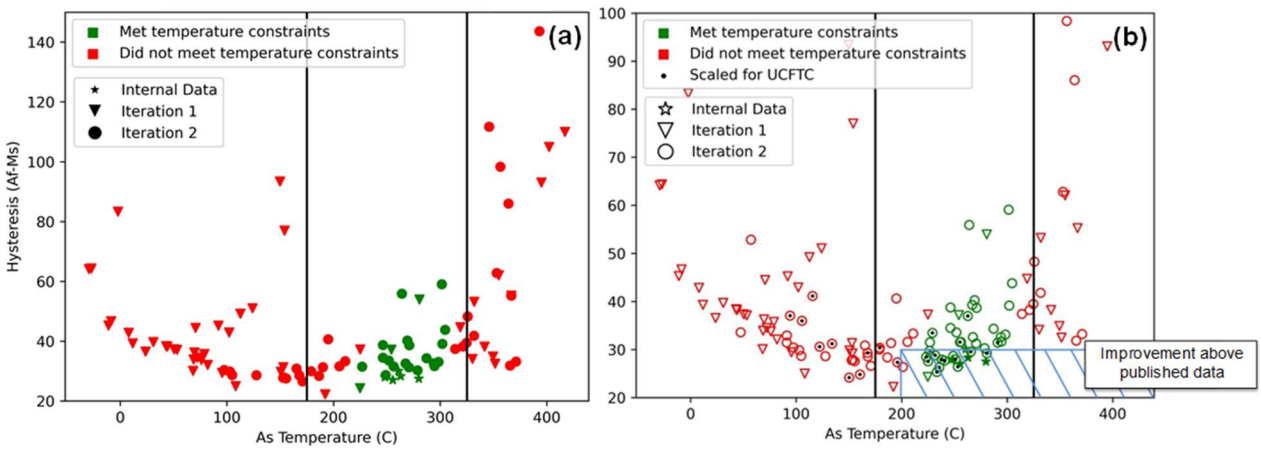

Figure 21: Performance pareto front of hysteresis vs A_s temperature through iteration 2, **(b)** sorted for scaled samples and improvement above published and internal data (as of 12/10/2024)

As of iteration 2 completion the pareto front form fabricated and tested samples has pushed the lower limit of hysteresis to nearly 20°C across multiple alloy compositions. If mechanical response can be shown to be in line with or improved over $Ni_{50.3}Ti_{29.7}Hf_{20}$ this research effort can be considered a large success. In addition, there seems to be a generalized trend of a local minima for hysteresis at A_f ~180°C which then increases with increasing transformation temperature. Though worth investigating is $A_f > 300$℃ where the hysteresis appears to begin trending down. Nearing ultra-high temperature SMAs without PGM inclusions that retain low hysteresis has not been shown in literature. It is possible the high temperature induced transformation fatigue, which appears like creep mechanically but with a different microstructural mechanism, may render them suboptimal as ultra-high temperature actuator compositions but it is a worthwhile consideration for future work.

Composition Scaling (I2-L/I3)

It became apparent by I2 where 4 alloys were scaled to 60g that an evolution occurs in the transformation temperatures after homogenization from 5g button samples to 60g. The backup Umale compositions (marked 'U') in I1 did not have full 5g characterization curves accessible as they were from a previous effort. The novel compositions initially developed at 5g and scaled to date are shown as overlayed DSC curves in Figure 22.

In general, the transformation temperatures of scaled up samples appear to be reduced in comparison to 5g button samples, with slightly reduced hysteresis. The standing hypothesis is the depression of temperature is related to speed of quenching post

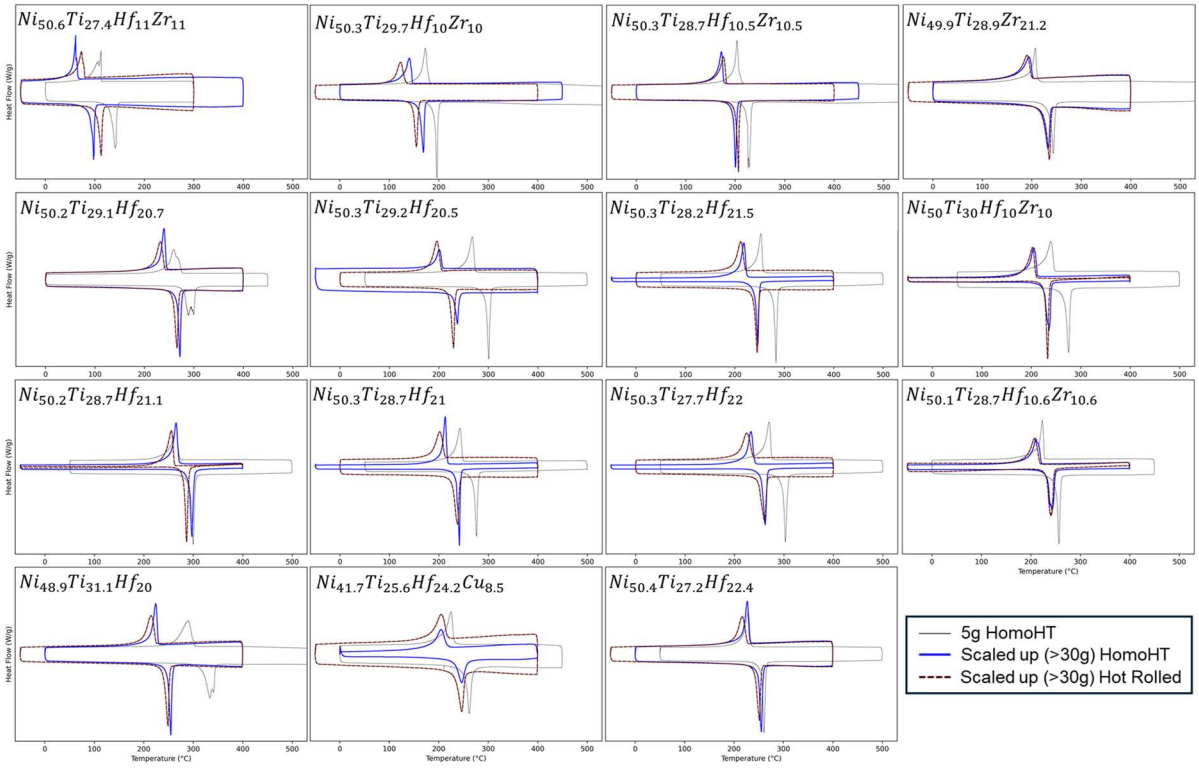

Figure 22: DSC transformation variation button (5g), scaled (35g/60g), and as hot-rolled

homogenizing heat treatment, which was implemented for I2 scale-ups, appearing as rows 2 and 3 in Appendix C I1/I2 data tables. A determination on hysteresis has not been made, but the low ($< 3℃$) disagreement does not pose a cause for concern, especially considering the large samples are likely more indicative of alloy hysteresis at device/feedstock scale.

After quench rate was increased for large homogenized and hot rolled via ice quenching the transformation temperature results more closely agree with their 5g progenitors. In addition, the I1 scale-up compositions were melted when the mixing procedure had not been optimized, resulting in $Ni_{49.9}Ti_{28.9}Zr_{21.2}$ mixing non-uniformly resulting in transformational differences across the rolled sample length and possibly different tension samples. Note in $Ni_{49.9}Ti_{28.9}Zr_{21.2}$ no transformation was observed in the 60g sample until after hot rolling. This composition was re-scaled and fabricated as part of I3, which appears as 35g samples in the figure. Generally significant transformation temperature departure in scale up appears to be resolved in I3, note the center 4 graphs where red and blue curves represent samples 30mm apart lengthwise in final rolled component. Where scaled transformation temperature (M_{peak}/A_{peak}) deviate by $> 75℃$ alloys were remelted.

Mechanical Performance

To accurately assess the actuation properties of the developed shape memory alloys they must be tested to a uniform process condition and as close to in accordance with ASTM 3097 as possible. Reportable metrics from the UCFTC test method include actuation strain, residual strain, hysteresis width, and temperature stress variations.

These will be the primary metrics to assess mechanical performance of investigated alloys. Specifically, the highest performing materials, regardless of heat treatment condition or load, will be the leading edge of actuation strain (maximize) vs hysteresis width (minimize). These compositions will then be compared for irrecoverable strain, material cost, or other secondary quantities of interest.

Specimen Processing

Mechanical Reduction

In I1, Dr. Umale's compositions were immediately scaled to 60g during I1. During forging 2 of the 3 specimens suffered catastrophic failure associated with embrittlement, though if this was inherent to the material or a result of processing was not possible to determine at time of failure. It was proposed that a combination of oxygen presence and unrestricted mechanical flow may be to blame. In canned extrusion reduction ratios of 9:1 is achievable in NiTiHf but the alloys are prepared in such a way that shear limit of grain flow must be overcome during extrusion. Notably, this was not a feature of the I1 forging cans. It is estimated that the getter material during hot rolling becomes a solid monolith in the initial steps forcing flow in the HTSMA in subsequent rolling steps.

There is also a yet-unexplainable seemingly random occurrence of diffusion of the encasing materials into the sample, though no samples with significant diffusion are processed into the next step. This occurred in both the sealing and heat-treating stage and after hot rolling. It has been demonstrated in Dr. Karaman's group the Ta diffusion is limited to near surface (<100μm) and is therefore counteracted by trimming a minimum of 0.1mm from sample edge to a test specimen face either for DSC or tension. In

addition, the actual rotating roller assembly is not heated to the same temperature as the sample, so the sample experiences significant undercooling as it is processed, it is currently unknown what effects it has on the final alloy.

Figure 23 shows the rolling progression of all I2 scaled alloys that utilize a 1" can. Figure 24 shows ¾" cans. I1 scaled alloys were attempted at 5% reduction before changing processes and did not transform in the window of interest so they are remitted

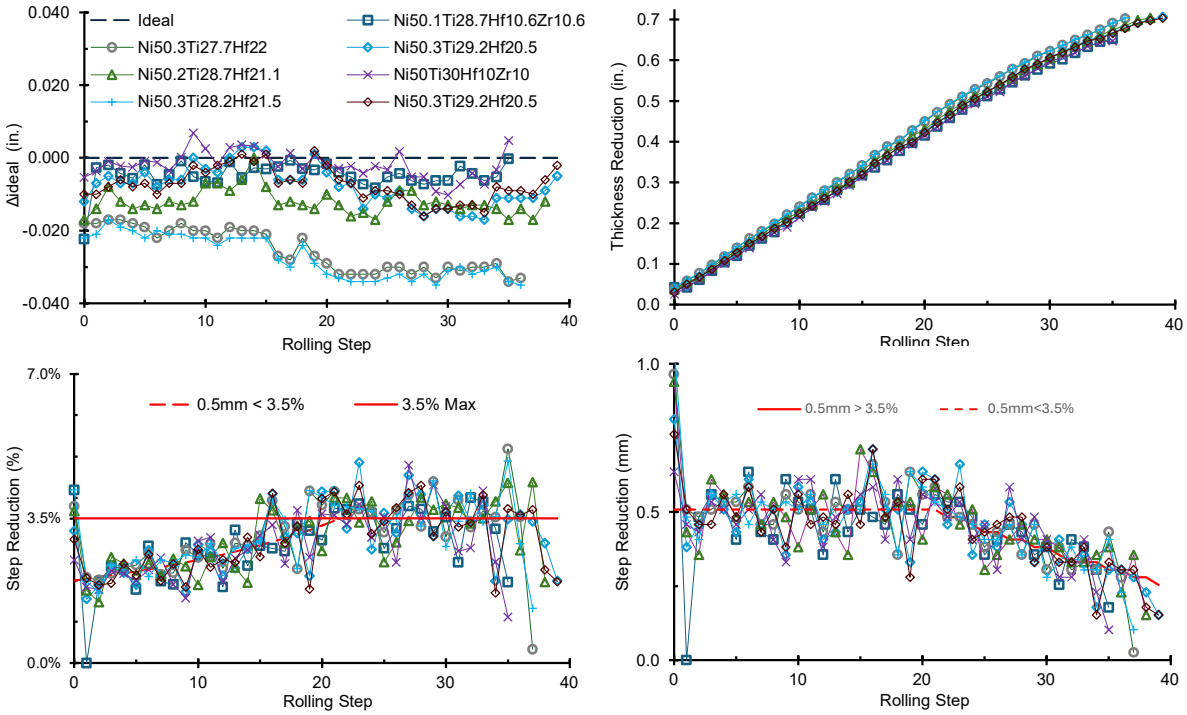

Figure 23: Rolling schedule results for I2 scaled up compositions (1" can), **a)** per step difference to idealized schedule **b)** thickness reduction compiled through steps **c)** individual step reduction as a percent after getter compression (step 0) **d)** stepwise reduction in mm

here for graph readability. 35g samples (canned in a ¾" tube) appear to follow a different reduction pathway when comparing b) figures which shows the thickness

reduction vs step but holds near 0 in variance from the schedule in a) measured as deviation from the ideal. It can also be seen that by rolling in ¾" cans the overall number of steps is reduced, resulting in multiple hours of saved rolling time per sample. The process aims to maintain 3.5% stepwise reduction (where it did not exceed 0.5mm) however since it is not possible to maintain a continuous 3.5% result, changing the rollers to more closely match the goal thickness resulted in oscillation around the 3.5% (or 0.5mm) but the samples were ultimately processed successfully. Successful processing indicates a lack of macro-fracturing, detrimental oxidation presence, or dimensionality unable to support tension samples.

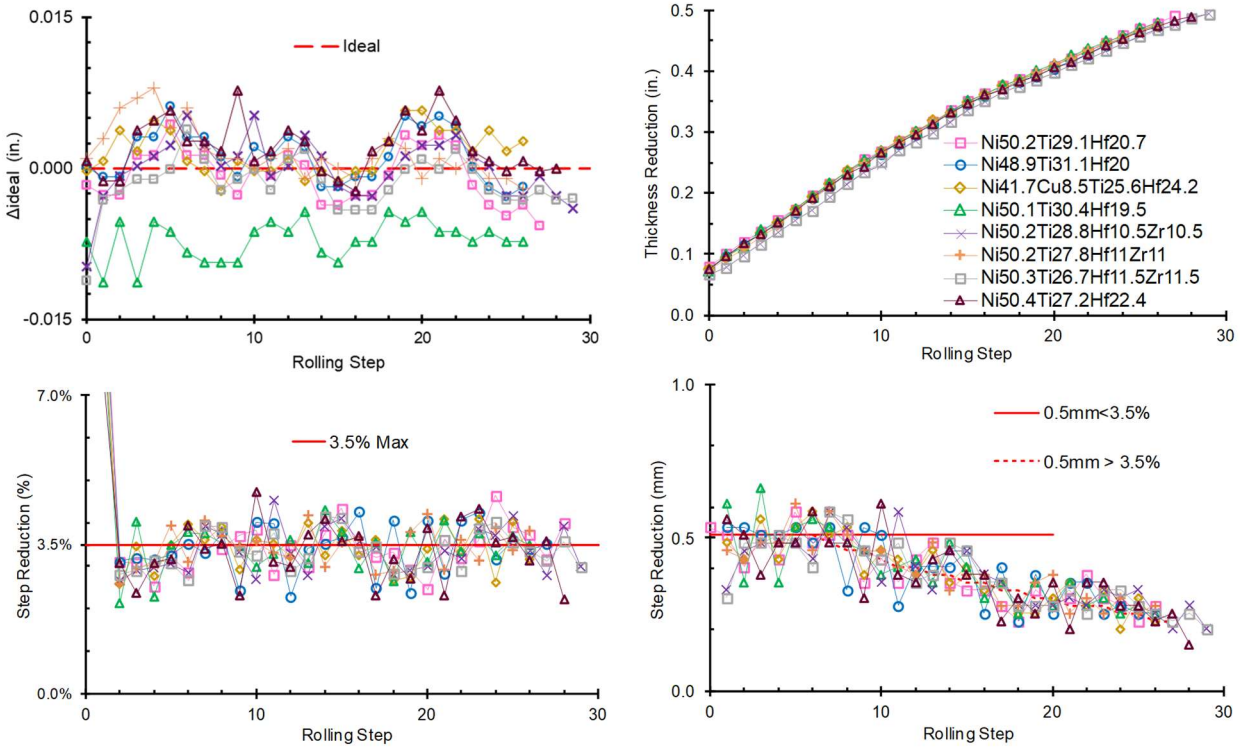

Figure 24: Rolling schedule results for I2 scaled up compositions (3/4" can), **a)** per step difference to idealized schedule **b)** thickness reduction compiled through steps **c)** individual step reduction as a percent after getter compression (step 0) **d)** stepwise reduction in mm

An additional challenge in maintaining uniformity is the hot rollers set to a specific height do not guarantee a sample of a specific height will emerge from the other end, rather a set height will transfer a specific load to the sample which will then reduce in association with ductility at temperature. During processing the ideal processing step is altered by as much as 0.002” to increase or reduce the resulting thickness to align with the schedule. Note I1 scale up materials were initially reduced at a 5% step ratio instead of 3.5% which was the result of failures in I1-L samples.

Ductility of individual compositions varied and even with a standard can dimension and refined process steps to maintain final thickness uniformity, individual samples deviate both from the idealized reduction percent (50%), and as much as 20% from the rolled thickness of their containers. The initial part thickness, container thickness, rolled thickness, final part thickness, and delta between are shown in Table 8.

Table 8: Hot Rolling Dimensional Variability I2-L

Specimen	Composition	$T_{Can,\ i}$ (in)	$T_{Can,\ f}$ (in)	R_{Can} (%)	$T_{Part,\ i}$ (in)	$T_{Part,\ f}$ (in)	R_{Part} (%)	ΔT (%)
1B	$Ni_{50.2}Ti_{29.1}Hf_{20.7}$	0.755	0.267	64.6%	0.456	0.234	49.85%	-14.9%
2	$Ni_{50.3}Ti_{29.2}Hf_{20.5}$	1.001	0.297	70.3%	0.463	0.232	49.84%	-20.5%
3	$Ni_{50.3}Ti_{28.2}Hf_{21.5}$	1.002	0.298	70.3%	0.470	0.236	46.00%	-20.4%
4	$Ni_{50}Ti_{30}Hf_{10}Zr_{10}$	1.002	0.355	64.6%	0.506	0.273	48.10%	-18.6%
5	$Ni_{50.2}Ti_{28.7}Hf_{21.1}$	1.004	0.307	69.4%	0.446	0.232	50.33%	-21.3%
6	$Ni_{50.3}Ti_{28.7}Hf_{21}$	1.001	0.295	70.5%	0.443	0.220	52.79%	-20.2%
7	$Ni_{50.3}Ti_{27.7}Hf_{22}$	1.002	0.299	70.2%	0.451	0.213	47.14%	-17.4%
8	$Ni_{50.1}Ti_{28.7}Hf_{10.6}Zr_{10.6}$	1.002	0.355	64.6%	0.505	0.267	49.72%	-17.4%
9A	$Ni_{48.9}Ti_{31.1}Hf_{20}$	0.751	0.277	63.1%	0.470	0.243	48.26%	-14.9%
10A	$Ni_{41.7}Cu_{8.5}Ti_{25.6}Hf_{24.2}$	0.751	0.280	62.8%	0.469	0.239	48.99%	-13.8%
11B	$Ni_{50.1}Ti_{30.4}Hf_{19.5}$	0.756	0.280	63.0%	0.487	0.246	49.95%	-13.5%
12A	$Ni_{50.2}Ti_{28.8}Hf_{10.5}Zr_{10.5}$	0.756	0.265	64.9%	0.507	0.233	54.09%	-10.9%
13A	$Ni_{50.2}Ti_{27.8}Hf_{11}Zr_{11}$	0.754	0.277	63.3%	0.508	0.239	52.94%	-10.3%
14B	$Ni_{50.3}Ti_{26.7}Hf_{11.5}Zr_{11.5}$	0.756	0.270	64.3%	0.510	0.232	54.53%	-9.8%
16B	$Ni_{50.4}Ti_{27.2}Hf_{22.4}$	0.752	0.269	64.2%	0.469	0.224	52.19%	-12.0%

It would be ideal to elucidate a trend from the data to indicate compositions with Zr or Cu in high fraction have increased ductility and should be reduced in container reduction, but there appeared to be significantly more at play than expected ductility of homogenized material. For example, specimens 2, 3, 6, and 7 were rolled in nearly identical conditions and began as approximately equal thickness dimensions (overall dimensions are increased for lower density materials) but resulted in final sample thicknesses from 46% to almost 53%. It was expected NiTiHf compositions, especially those that were nickel lean, would be expected to be more resistant to plastic flow than the quaternary alloys which was observed. Composition 10 which included a high copper elemental addition was expected to be comparatively more ductile, hence the addition of copper, but this was not found, perhaps as a function of the increased Hf to ensure proper transformation temperature. With the unpredictable nature of the samples continuous learning and small process modifications allowed for all samples to be rolled within 5% of a true 50% reduction in hot rolling.

Heat Treatment

After initial testing additional tension samples were heat treated to improve mechanical performance. In both NiTiHf and NiTiZr h-phase precipitating particles have been shown to stabilize and improve actuation behavior. The fundamental improvement in shape memory effect is a function of multiple crystallographic phenomena: the symmetry of austenite to martensite, the ability for martensite to mosaic twin, the amount of reorientation that must be overcome during transformation, the coherence of the precipitates to the parent phase, etc. The optimum parameters for an individual alloy

are only known to the limit of previous experimental testing, e.g. peak aged $Ni_{50.3}Ti_{29.7}Hf_{20}$ occurs at 550°C/3Hrs. However, minute changes in time, i.e. 550°C/2.5Hrs vs 550°C/3.5Hrs vs 515°C/3Hrs have not been validated beyond theory. In addition, this becomes even more convoluted when considering that precipitation and coarsening kinetics vary depending on small changes in composition, as well as the underlying matrix phase composition, and therefore transformation temperatures. In addition, validating macro- SME performance characteristics to precipitation sizes requires TEM examination.

Here the optimal h-phase precipitates are small enough to be fully coherent with B2 austenite phase and fully absorbed into the B19' phase upon transformation to martensite as well as uniformly distributed, from literature this is likely shorter than 20 nm in length and less than 6 nm in width. This theoretically will lead to increased mechanical shape memory performance. While an investigated heat treatment is unlikely to absolutely optimize performance, for similar reasons to commercial off-the-shelf HTSMAs, it will enable performance comparisons, both to pre-heat treat of a given alloy and other heat-treated alloys. Ideal performance will be an equivalent or reduction in hysteresis, with an increase in transformation temperatures. The latter condition is in combination of a desire to bring high performing low temperature compositions into the ideal operating window and the known trend of low volume fraction, non-coarsening, and non-uniformly distributed precipitates to depress transformation temperatures after short duration heat treatments.

Unfortunately, an exhaustive study of heat treatments on each novel alloy is not viable. To avoid simply using optimized characteristics for previously investigated alloys a reduced sample set study was implemented where DSC was examined for as-hot rolled condition alloys. In literature, nickel lean compositions below 50.3 at% tend to, or do not (Ni ≤ 50 at. %), precipitate h-phase and Zr containing alloys have lower thermodynamic thresholds for precipitation and coarsening in equivalent replacement

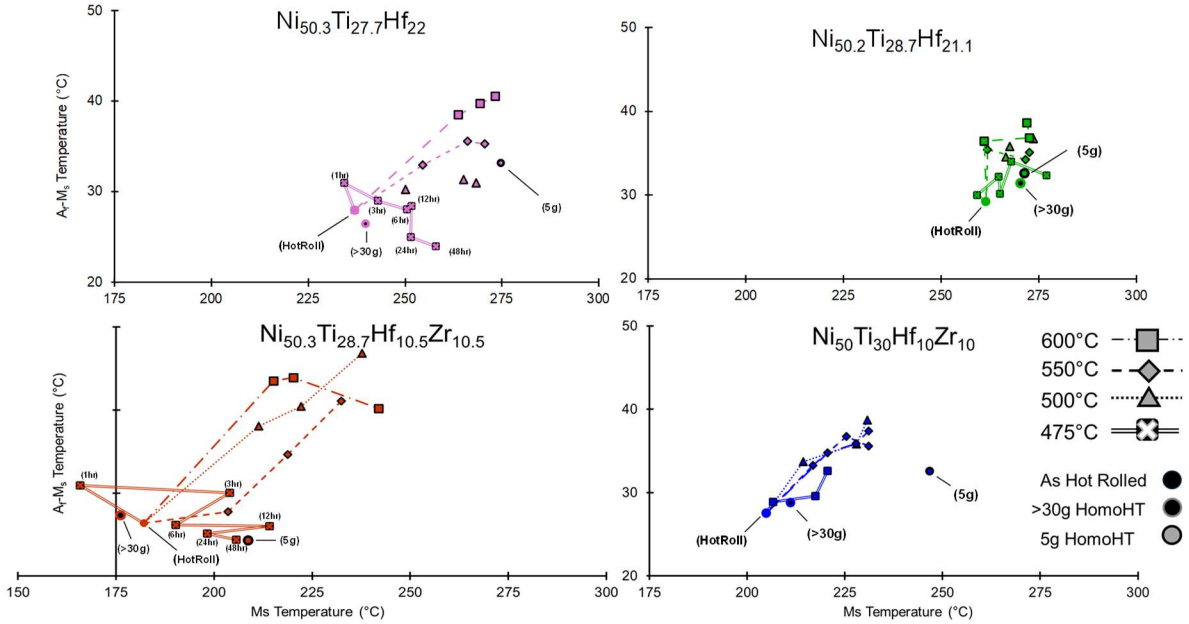

Figure 25: Secondary heat treatment Ms variation for selected compositions

ratios alloys. Alloy compositions scaled for tension were reduced into 4 groups, high (≥50.3 at.%) nickel content Hf ternary alloys, low (≤50.3 at.%) nickel content Hf ternary alloys, high (≥50.3 at.%) nickel content HfZr quaternary alloys, and low (≤50.3 at.%) nickel content HfZr quaternary alloys. Selected alloys $Ni_{50.3}Ti_{27.7}Hf_{22}$, $Ni_{50.2}Ti_{28.7}Hf_{21.2}$, $Ni_{50.3}Ti_{28.7}Hf_{10.5}Zr_{10.5}$, $Ni_{50}Ti_{30}Hf_{10}Zr_{10}$ were heat treated initially at 500°C, 550°C, and 600°C for 1, 3, and 6 hour durations at each temperature condition. Upon initial examination where no heat treatment resulted in a reduction of

hysteresis a 475°C heat treatment was added. The results of the initial investigation are in Figure 25. Individual graphs for all DSC values of interest are available in appendix B.

Starting with $Ni_{50.2}Ti_{28.7}Hf_{21.2}$, it appears as if the 500°C, 550°C, and 600°C heat treatments do not significantly vary from one another, with only minute changes in trend all durations and temperatures appear to increase the hysteresis width and only minutely change the transformation temperature. With nearly all transformations clustering around the 5g and >30g sample in the as melted condition with the hot roll condition having both lower transformation temperatures and hysteresis it is hypothesized that the heat treatment simply relaxed the mechanically developed grain boundaries rather than forming a secondary phase, or the formed secondary phase was less compatible with the matrix and only represented a small volume fraction. The first hypothesis could be due to the high energy barrier in Ni lean high Hf compositions and is supported by the general decrease in A→M enthalpy across heat treatment temperatures. The varying grain structures to each DSC location may be attributed to the observable randomness. If h-phase did precipitate but not improve the austenite to martensite compatibility resulting in increased hysteresis it would be reasonable to expect variations in the transformation temperatures and hysteresis as a function of coarsening. This is not observed.

Alloy $Ni_{50}Ti_{30}Hf_{10}Zr_{10}$ appears to increase transformation temperatures and hysteresis in a uniform pathway across all transformation temperatures except 475°C. If the previous hypothesis is true where nickel lean compositions are below the

thermodynamic threshold to precipitate Hf h-phase with the addition of Zr it is possible the thermodynamic threshold of Zr h-phase is preferentially met at every temperature and is simply limited by the diffusion of Zr out of the matrix and into the h-phase. Below 500°C the precipitation and growth may be thermodynamically rather than chemical species limited. In addition, the non-uniform removal of Zr from the matrix could lead to lattice strains which result in the increase of enthalpy across all temperatures except 600°C, where relaxation may be dominant and can be shown by the close approximation of change in enthalpy above 600°C for $Ni_{50}Ti_{30}Hf_{10}Zr_{10}$ and $Ni_{50.2}Ti_{28.7}Hf_{21.2}$. By the goals set out initially, neither of these compositions saw successful heat treatment.

$Ni_{50.3}Ti_{27.7}Hf_{22}$ is the closest of the selected compositions to highly investigated ternary materials for h-phase precipitation, only varying in Hf by 2 at. %. Based on literature it was expected this would cause increased coarsening at long durations since the diffusion out of the matrix is increased at higher Hf contents. Of the discussed materials thus far, it is the first which clearly seems to precipitate the h-phase as demonstrated by the striations in terms of lattice compatibility (hysteresis) and transformation temperature increase by matrix depletion. Notably, for similar time durations the transformation temperatures slow small deviation but the hysteresis deviations to other temperatures are large. It is likely this is caused by coarsening at various rates associated with available thermal energy since diffusion rate from a $Ni_{50.3}Ti_{27.7}Hf_{22}$ matrix to h-phase would be slower as continued Hf matrix richness nears the proposed $Ni_{52.5}Ti_{21.2}Hf_{26.3}$ composition. However, none of the observed transformation trends reduced hysteresis, in contrast to Evirgen's investigation on

$Ni_{50.3}Ti_{27.7}Hf_{15}$. A 475°C was then completed, while an initial increase in hysteresis was observed, the long-term trend counter to $Ni_{50.3}Ti_{27.7}Hf_{15}$ was an increase in transformation temperature and decrease in thermal hysteresis which continued after 9hrs through a 48hr heat treatment.

Alloy $Ni_{50.3}Ti_{28.7}Hf_{10.5}Zr_{10.5}$ was tested and was outside of the range of acceptable transformation temperatures, however, it also had one of the absolute lowest hysteresis values in the set. It was an extremely important test case for heat treatment as the increase in transformation temperatures would drive the alloy into to the 175°C-325°C range rather than alloys which could be driven out. Like $Ni_{50.3}Ti_{27.7}Hf_{22}$ 500°C, 550°C, and 600°C all resulted in increased hysteresis and transformation temperatures likely striated by coarsening. Noting that like $Ni_{50}Ti_{30}Hf_{10}Zr_{10}$ the Zr content appears to make the alloy more susceptible to heat treatment in terms of resulting increases in transformation temperature. In a nickel rich alloy this is likely a combined effect of what is occurring in $Ni_{50}Ti_{30}Hf_{10}Zr_{10}$ and a relatively increased rate of h-phase formation and precipitation noted by the largest deviation from as-hot rolled in both transformation temperatures and hysteresis. At 475°C a similar trend to $Ni_{50.3}Ti_{27.7}Hf_{22}$ is observed where the long duration trend is increased transformation temperatures and reduced hysteresis. The larger variance in $Ni_{50.3}Ti_{28.7}Hf_{10.5}Zr_{10.5}$ may be attributed to marginally different rates of Hf and Zr h-phase formation in individual samples, however the trend remains intact.

It may be attributed to the size of the h-phase formations, or the additional availability of Ni is the resulting matrix composition, or too low a temperature to relax

the mechanical work imparted structure, or a combination. Regardless, the precipitations that occur at 475°C in nickel-rich (≥50.3 at. %) alloys in long duration heat treatments are fully coherent and improve the properties of interest. After the results of the DSC heat treatment experiment, scaled alloys with Ni content above 50.3 at. % were heat treated at 475°C for 48 hours and tested in UCFTC.

Tensile Uniaxial Constant Force Thermal Cycling

ASTM 3097 sets a requirement of 3°C gradient across the gauge section during a complete test. The standard ramp speed is 10°C/min. Meeting this variance is a physical limitation of the conduction heat transfer open air test frame that exists at Texas A&M. Based on a secondary experiment the gradient can be maintained at maximum heating and cooling rates of 4°C/min and 7°C/min respectfully. In Appendix A the full heat cycle information will be given for one test to indicate the control methodology. With the mechanical attachment of a thermocouple to the center of the gauge section, it can be inferred that the absolute center will lag (up to the gradient) on both up and down cycle temperatures. Therefore, thermal hysteresis will appear narrower than the true average of the gauge section. The gauge section of the specimen significantly lags the instrumented hot ends of the tension system, by as much as 50℃ at 450℃. It has been attempted in the heating collar over liquid nitrogen design to change the location of the feedback thermocouples, but the PID delay proved unstable. One solution would be to use a combination of DIC and a thermal camera to simultaneously capture the strain effect of the system and the temperature gradient across the gauge section, however without camera shielding at high temperatures this is not practical. This represents significant

inefficiency and is in the process of being resolved by a design change as will be discussed in a later chapter.

Performance Evaluation

Each alloy was tested in the as-hot rolled state after EDM processing and hole drilling to enable mounting in tension. Adhering to ASTM 3097 for tensile UCFTC transformation temperatures, actuation strain, cooling transformation strain, heating transformation strain, thermal transformation span, and hysteresis width are all reported in Appendix A in both graphed and tabular format. Notably many materials will not appear to 'break-over' that is reach a point where they begin to experience plastic strain and transformational strain drop as a function of load, rather many of the materials begin to undergo what appears to be slip in preference of transformation at high temperatures as can be observed in Figure 26. It is hypothesized that the amount of mechanical work

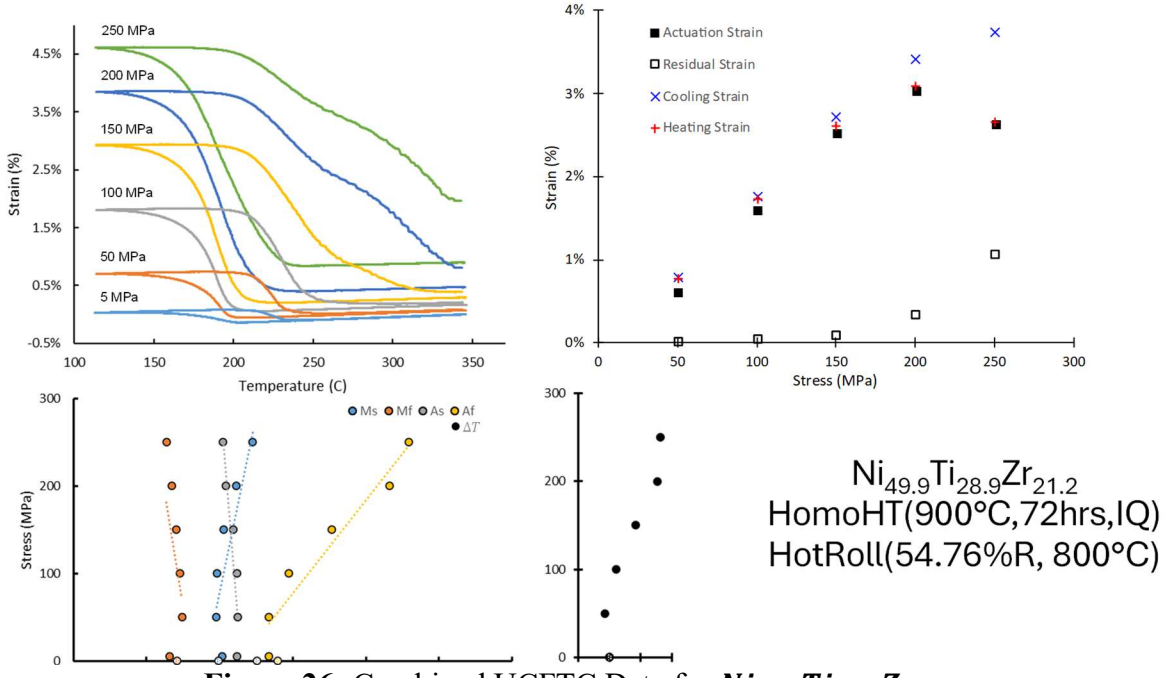

Figure 26: Combined UCFTC Data for $Ni_{49.9}Ti_{28.9}Zr_{21.2}$

from a 50% reduction did not maximize grain orientation against high temperature slip which appears as a change of transformational slope compared to the martensite transformation and a significant increase in austenite finish temperature. $\boldsymbol{Ni_{49.9}Ti_{28.9}Zr_{21.2}}$ in Figure 26 is used here as a demonstrator because high Zr experiences slip at a higher rate than an equivalent alloy Hf system. Here above 250°C and 100MPa plastic deformation appears to be favored over transformation orientation and at 250MPa a full transformation is not possible. It is arguable even at 200MPa a full transformation does not occur. In cases where this occurs, when load is increased to the next step the austenite may not have fully transformed during heating and results in significant plastic strain at the next step. Where slope changes significantly, slip is encountered, or transformation does not occur completely in accordance with ASTM 3097, the last fully valid step will be reported.

Performance of evaluated alloys will initially be measured by the pareto front given by graphing hysteresis width against actuation strain filtering for stress loads that transform within the 175°C–325°C extended range. Specifically transforming within M_f and A_f, measured as slope intersection estimates not M_f* and A_f* which are mechanically indicated complete transformation. The latter transformations will be used as further refinement since they indicate a much tighter window of complete transformation.

As-hot rolled performance in terms of hysteresis vs actuation strain (eACT) for tested samples is included in Figure 27. Note the dotted lines are compositions which were tested and operate outside the area of interest (below 175°C-325°C) but were

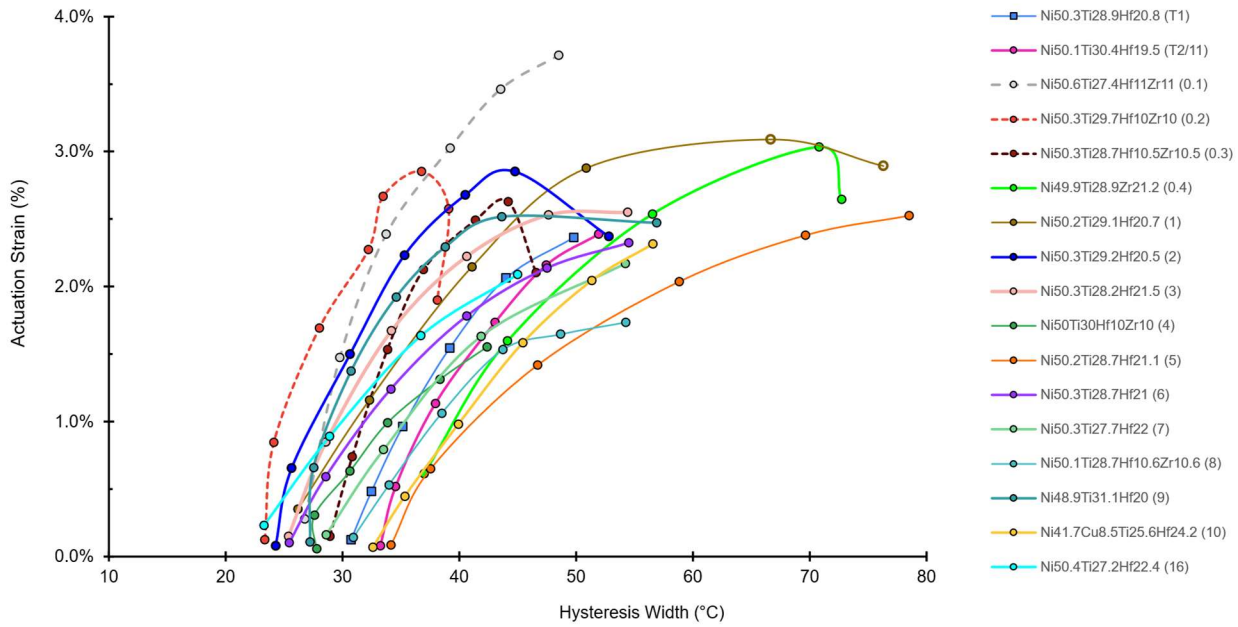

Figure 27: Hysteresis actuation pareto front for as-hot rolled compositions, compositions 12, 13, and 14 were not tested on account of time and transformation temperature below area of interest

included here for initial discussion. Prior to continuing discussion, it should be noted that all the compositions included in Figure 27 represent novel alloys and the first large scope tensile testing of materials above 200°C. Operating mechanically above 200°C in tensile with a usable (ΔT below 40°C) 2% strain without the use of PGMs across multiple alloys is a literature first to the author's knowledge.

As pointed out in Figure 26, if 200 MPa is chosen as the final stable measured load cycle for $\boldsymbol{Ni_{49.9}Ti_{28.9}Zr_{21.2}}$ it does not reach a peak actuation strain before rolling over. This is an indication that the sample is being limited by high temperature slip before experiencing plastic deformation because of defect formation or crystallographic compliance from the imparted stress. In Figure 27, if compositions below the region of interest are discounted (they will not experience >300°C temperatures) only 4 specimens

actually reach a breakover point, indicating minimization of hysteresis is not likely the greatest challenge within this alloy set but rather designing resistance to slip mechanisms in high temperature application. While the most common pathway in wire drawn SMA systems is simply to significantly increase the amount of work strengthening there is not an identical pathway for process manipulation of grain morphology for a part built in L-PBF or EB-PBF. High temperature HIP could be used to solutionize and increase densification, but directional refinement of the grain morphology post fabrication is not possible. There is a possibility of in-situ microstructural control as has been demonstrated in W in EB-PBF at ORNL but application as a reliable/repeatable technique has not been implemented at a tool level in the commercial space.

The alloys are further refined for UCFTC transformation temperatures within the bounds of this study, $M_f \geq 175℃$ && $A_f \leq 325℃$, and shown in Figure 28. Based on

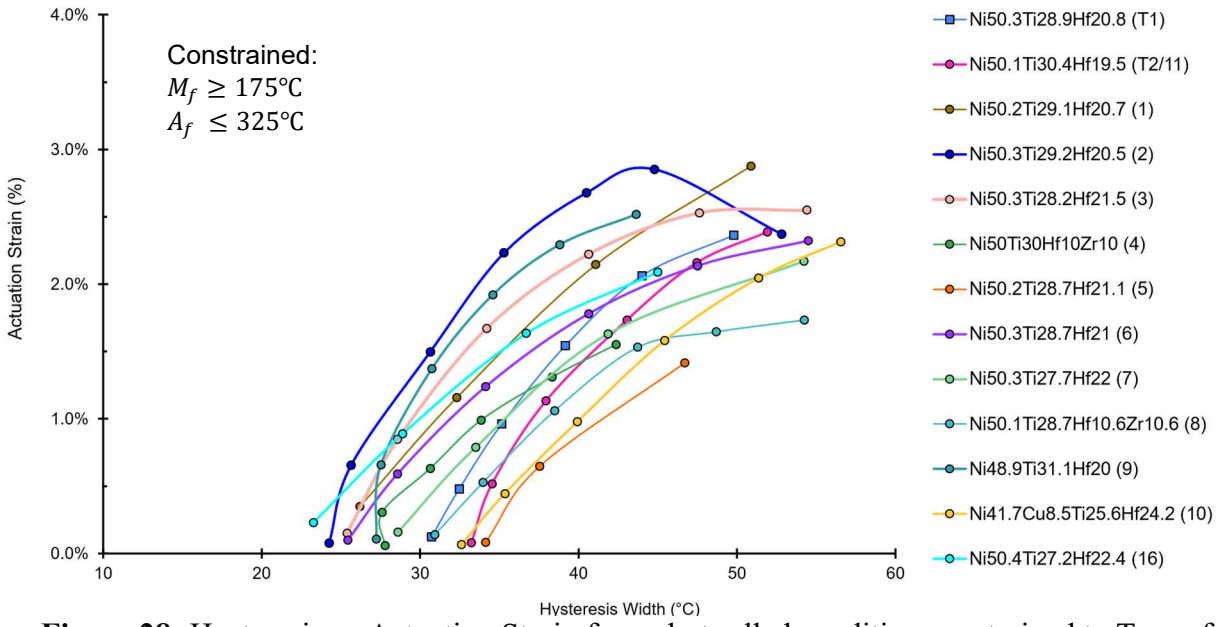

Figure 28: Hysteresis vs Actuation Strain for as-hot rolled condition constrained to T_{span} of interest

this figure it would be reasonable to infer that the optimized composition for the space of interest is $Ni_{50.3}Ti_{29.2}Hf_{20.5}$. From an outside perspective this seems like a simple case of taking a very well researched material $Ni_{50.3}Ti_{29.7}Hf_{20}$ and adding Hf until a desired transformation temperature is reached. However, there are 5 other compositions on this graph that are simply increases in Hf content to$Ni_{50.3}Ti_{29.7}Hf_{20}$ with varying results for minimization of hysteresis. In unloaded state the lowest mechanical hysteresis is actually $Ni_{50.4}Ti_{29.7}Hf_{22.4}$ (a model discovered alloy) which follows based on the high Ni content but it's hysteresis gain as load increases is greater than that of $Ni_{50.3}Ti_{29.2}Hf_{20.5}$, $Ni_{48.9}Ti_{31.1}Hf_{20}$, $Ni_{50.3}Ti_{28.2}Hf_{21.5}$, and $Ni_{50.2}Ti_{29.1}Hf_{20.7}$. While the test to test variability is unknown, if the results are taken as ground truth it would indicate that there is a complex relationship to performance moving from $Ni_{50.3}Ti_{29.7}Hf_{20}$ to $Ni_{50.3}Ti_{27.7}Hf_{22}$. The latter being the lowest performing of the set with Ni content above 50.3%.

Other items of note are the Ni-lean composition $Ni_{48.9}Ti_{31.1}Hf_{20}$ which performed nearly in line in the as-rolled state to $Ni_{50.3}Ti_{29.2}Hf_{20.5}$. Conventionally lean NiTiHf materials are stronger than rich NiTiHf materials prior to heat treatment but generally have poorer hysteresis performance. It would be interesting to consider such a lean composition as a candidate for atomization and fabrication by PBF. While Ni-rich compositions lend themselves to vaporization resilience because vaporized nickel can be used to tailor performance, such a low nickel content may be vaporization invariant, assuming a nearly flat transformation temperature nickel dependence curve on the lean end, which is the case for NiTi.

Aside from $Ni_{50.2}Ti_{28.1}Hf_{21.1}$ which is cut short because most of its transformation occurs above A_f = 325°C the lowest performing systems are quaternary systems of HfZr and CuHf. If the ternary NiTiHf materials have an intrinsic improved austenite martensite symmetry and stabilization to slip there may not be an obvious addition or substitution that allows for commensurate performance at a lower cost. With the significant rise in Hf cost over the last 5 years it is possible it may rapidly be associated with the PGMs this study aims to replace. This is all in the as-hot rolled condition, additional trends emerge after heat treatment.

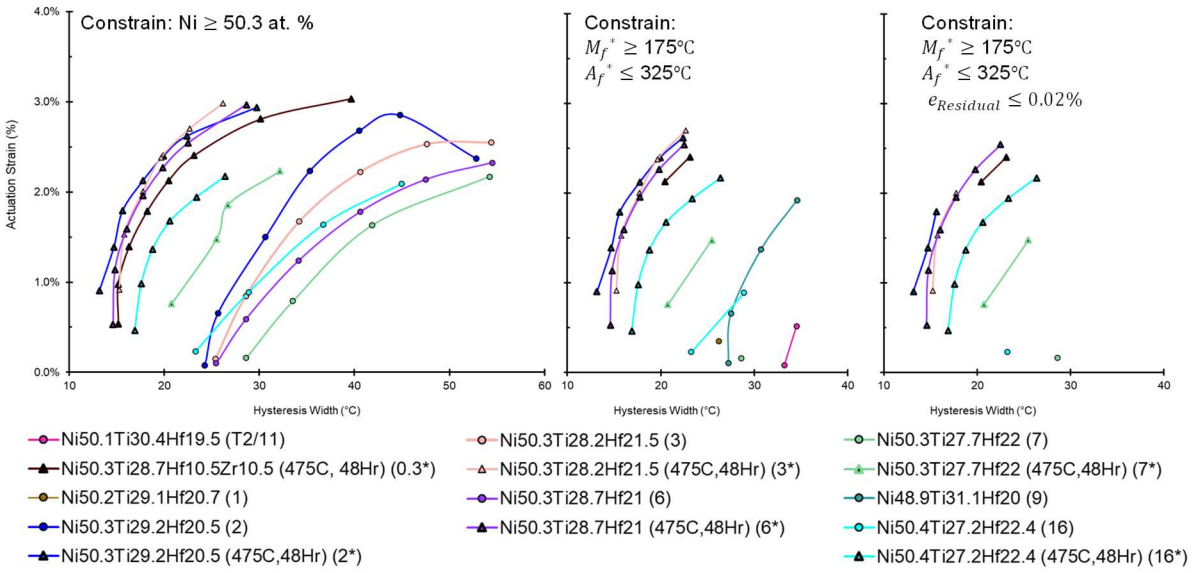

Figure 29: a) Nickel-rich UCFTC data pre and post heat treatment, **b)** down selected for full transformation in selected range, **c)** down selection for fully recoverable stress states

Figure 29 a) shows the performance improvement for UCFTC alloys after heat treatment at 475°C for 48 hrs. It is immediately obvious what previously was study leading became effectively irrelevant after heat treatment. The improvement in hysteresis width puts the compositions in the range of high Cu content NiTiCu system or

NiTiPd/NiTiPt systems while operating at a high temperature. Again, the lag associated with thermocouple placement may be underestimating the thermal hysteresis, but even if accounting for 6°C of error allowed by ASTM 3073, 4 different compositions have mechanically validated hysteresis in tension of <30°C above 200°C without the use of PGMs. Possibly even more exciting is the quaternary alloy $Ni_{50.3}Ti_{28.7}Hf_{10.5}Zr_{10.5}$ which appears to perform nearly in line with the Hf ternary alloys after heat treatment and significantly outperforms any materials as-hot rolled. $Ni_{50.3}Ti_{28.7}Hf_{10.5}Zr_{10.5}$ compared to $Ni_{50.3}Ti_{28.7}Hf_{21}$ at the price paid by Texas A&M for arc melting supply materials would cost $4,425.20/kg and $6,288.37/kg respectively. This is a over 42% reduction in cost for very similar mechanical performance, let alone the savings for an alloy like $Ni_{20}Ti_{50}Pd_{30}$.

When tightly constraining the transformation span, that is using complete transformation values rather than calculated finish temperatures, it becomes apparent that the highly stable and low hysteresis heat treated samples dominate. Under the most stringent requirements for this project, a composition which fully transforms within the thermal window, still returns over 2.5% strain at <20°C hysteresis. Further refinement occurs by looking at fully recoverable strain, that is, when residual strain is for all intents and purposes, zero. Benefan used the value 10^{-3}% however based on the forward and backward backlash that is present in the Texas A&M hydraulic system <0.02% was instead used. With this criterion, the three most optimal compositions found are $Ni_{50.3}Ti_{28.7}Hf_{21}$, $Ni_{50.3}Ti_{28.7}Hf_{10.5}Zr_{10.5}$, and $Ni_{50.4}Ti_{27.2}Hf_{22.4}$.

Depending on the criterion, the 'optimal' composition is different. For low variance to off the shelf composition, to the point it may even be cost effective to purchase $Ni_{50.3}Ti_{28.7}Hf_{21}$ did in absolute terms achieve the best, peaking at just over under 3% fully recoverable strain with a 28°C hysteresis width, and transformation span of 75°C at 400MPa, peaking at 3.2% strain at 500MPa but passing the 0.02% fully recoverable threshold. Notably, the A_f* temp is above 325°C but the slip appears fully managed by precipitates. $Ni_{50.3}Ti_{28.7}Hf_{10.5}Zr_{10.5}$ is extremely similar but at a fraction of the cost. Finally, $Ni_{50.4}Ti_{27.2}Hf_{22.4}$ has even greater Ni content and could be additively manufactured across a wider range of processing parameters and still be above the 50.3% threshold for h-phase formation.

The combination of results herein represents a significant move forward in the mechanical testing literature in novel high temperature shape memory alloys. However, one area of scientific improvement would be the retesting/multi-testing of the alloys. The difficulty in fabricating each alloy along with the relatively small number of tensile specimens and long duration of testing made repeat testing undesirable. However, without multiple tests statistically significant inferences cannot reasonably be made. It would also be valuable to take the absolute peak performing materials and run them for cyclic stability or training potential.

Tension Frame Development

The existing tension frame in Dr. Karaman's laboratory built for testing 26mm (8mm gauge) length samples is also used for testing at controlled temperature. Thermal

control can be static as is the case for pseudoplasticity, or dynamic/cyclic for UCFTC. The samples are centered by a 1mm through pin on grips which have two through bolts which are tightened by nuts to lock the grip faces to the sample face via friction. Heating and cooling are controlled by instrumented controllers corresponding to the top and bottom grips, sample temperature is not directly controlled. Sample temperature is taken via a contact (but not welded) thermocouple, top and bottom grip temperatures are similarly taken via contact thermocouple between the head of the grip and the body, as seen in the isometric projected view in Figure 30. Heating occurs via resistance heating bands, rated at 300W and a max temperature of 900°F. The bands are wrapped around $^1/_8$" copper tube which is wound around a Ø$^1/_2$" bar that makes up the tension grip body. The Ø$^1/_2$" bar body is tightened into a collet which is integrated into the load cell (top) or piston assembly (bottom).

Liquid nitrogen is stored in standing tanks with a capacity of nearly 300lb. The LN2 is released via electronic needle actuators which then flows through the copper tubes to cool the setup and is vented to atmosphere. The grip bodies and thermal control elements are covered with insulation and wire tied. When in use for temperature control the tension specimen and grips are also covered in insulation to minimize heat losses. The 'control volume', i.e. the atmospheric environment between the insulation and sample is less than 1L.

The original setup was rated from -100℃ to 400℃, but rarely saw temperatures above 300℃ before the effort of this testing. Unfortunately, for routine usage at that temperature a number of concerns needed to be addressed and solutions engineered. The

nuts and bolts used to tighten the sample are zinc coated mild steel and do not utilize lock washers, nylok nuts, or other mechanical process of restricting nut loosing. Though vibrational movement is low to extremely low, the temperature cycles the frame is rated for (-100℃ to 400℃) can heat cycle the mechanical fasteners to where friction is no longer a dominant holding force. The holding pins primarily used pins are H13 which are extremely strong at room temperature and resistant to cryogenic temperatures but are heat treated at temperatures above 300℃, and with an inability to track cycles, to an unknown effect. At high cooling rates or low ($\leq -20℃$) control temperatures the LN2 actuators have been known to seize reducing or eliminating stable thermal control. The copper tubing experiences significant oxidation at high ($\leq 300℃$) which can scale and break off reducing the contact and therefore maximum conduction efficiency from the heater bands to the controlled grips. The grip material composition is unknown, meaning a failure associated with heat cycling or weakening could occur. Finally, the location of the thermocouples results in a significant thermal transience (time delay between action and result of interest) as well as controlling temperature on the grip body rather than the grip head which contacts the specimen.

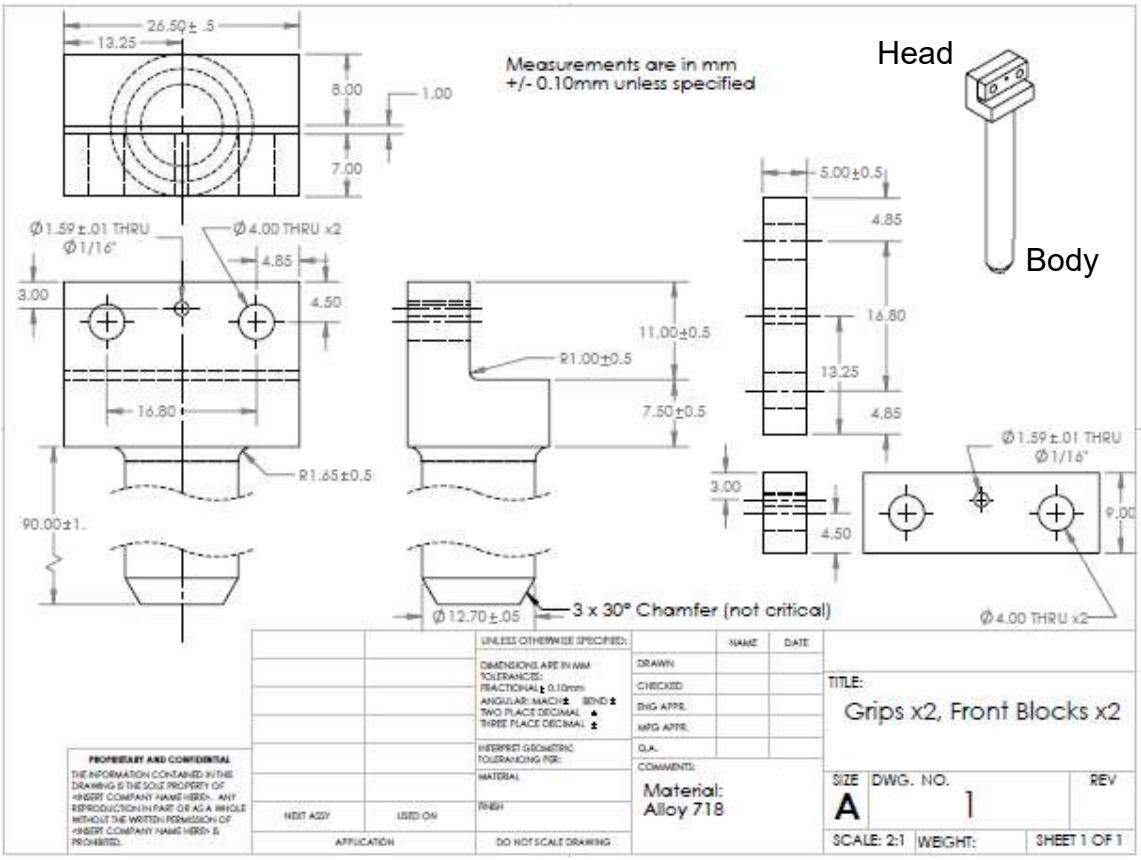

Figure 30: Reverse engineered, alloy 718 tension grip, without thermocouple location

To solve the problem of unknown grip body material the grips were reverse engineered (no accurate previous drawing existed) and fabricated in Ni-alloy 718 which does not experience a ductile to brittle transition like steels and has high strength even at high temperatures and creep resistance above 600℃. The grips were further refined with addition of a $^{1}/_{16}$" thermocouple probe whose tip is as near to the center of mass of the grip head as is practical and includes a backing plate so if the thermocouple breaks off, it is possible to reuse the grip without drilling out the thermocouple. 718 is also used for sample pins in use cases above 150℃. A286 bolts and 316L nuts replace mild steel M4 nuts and are corrosion resistant to 700℃.

LN2 valves are now cleaned regularly and sit on top of a thermally controlled and vibration dampened plate. The 120W heater strip is contained in a sealed (to waterproof against condensed water vapor from LN2 for electronic parts) sandwich of $^{3}/_{16}$" aluminum plates. The plates provide increased stability for solenoids and improved heat transfer. The pad is controlled by a binary controller which activates when the solenoids are detected to be below 5℃. Since installation the system has recovered from rapid cooling where solenoids were below -30℃ with no stuck valves. Insulation was also improved from a low-density fiberglass (like that found in houses) insulation to a high-density fiberglass ceramic insulation which is rated to 700℃

To accommodate ultra-high temperature SMA UCFTC (≤ 700℃) additional changes had to be made. The existing water-cooling was upgraded to separate the load cell, which is temperature sensitive, to a 600℃ testing area. The load cell is wrapped by $^{3}/_{8}$"ID copper tubing (increased from $^{1}/_{8}$") flowing at over 1gpm. The hydraulically controlled piston is now also water cooled with a $^{1}/_{4}$"ID copper tubing line tightly wrapped cooling the plunger between the grip body and piston body to avoid heat soaking the hydraulic fluid. The existing collars are not capable of such high temperatures and have burned out with high temperature requests in the past, likely due to poor conduction and overheating. To aid in the distribution of heat, reduce the workload of the heater, and increase rated temperature a 1.5" ceramic heater rated for 450W is replacing the existing collars. The interior diameter will not change, and will allow emergency replacement using the old heaters should a new one burn out.

The cooling coils made from copper were removed in favor of a bronze (C360) monolith, chosen for its high thermal conductivity, machinability, ductility, strength, and

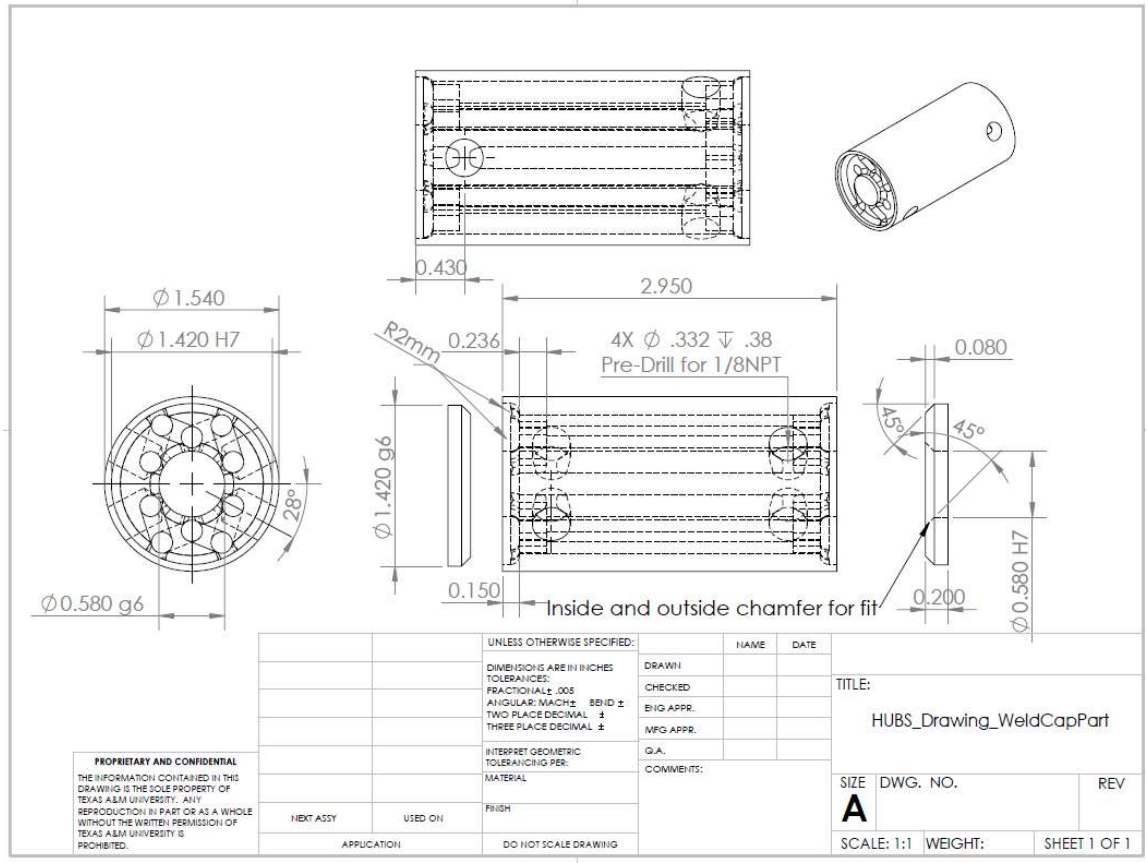

Figure 31: Final technical drawing for grip monolith including caps. Caps and shaft had an engineering fit to aid welding.

low cost. In addition, the material can be torch welded (with some difficulty as the process had not been accomplished by the author or lab managers prior) which allowed for the through drilled and capped design in Figure 31. Without the ability to weld on a cap the through-hole gas design would not have been possible without additive manufacturing which would've significantly increased the price of the retrofit. As designed the deep through holes and thin well features for the caps to sit in were fabricated by an outside CNC shop and the holes would be NPT tapped on site at TAMU

post welding because of an oxide layer that formed from the oxyacetylene welding torch. After tapping the part will be mounted on a lathe and center drilled and reamed for an interference fit on the 718 grips. The C360 has a higher coefficient of thermal expansion so it is important that at 700℃ there is still a tight fit, this will be accomplished by heating the collar, cooling the grip and utilizing a shop press.

In the assembled state, in Figure 32, LN2 enters one of the 4 NPT tapped holes in the side of the body and routed through the monolith 4 times before exiting and being vented outside on the opposite end (top entrance, bottom exit and vise-versa) as the LN2

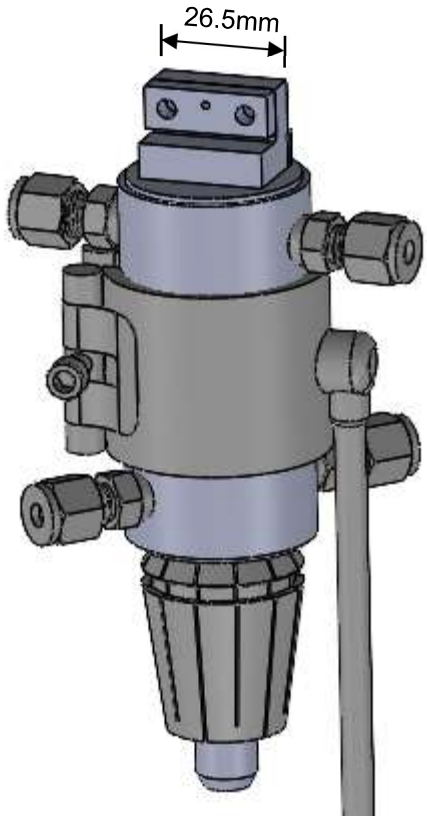

Figure 32: Assembled monolith including copper tube fittings, 1.5” resistance band heaters, and approximate collet for tension frame fitment

entered. The pathways are mirrored on the other half of the monolith to create uniform cooling. This design significantly increases the coolers contact area to the grip body, the pathway of the LN2 to result in maximum cooling energy extracted, and conduction between the grip heater to grip body by way of a large, thermally stable mass. The large mass should enable slower temperature deviation from programmed and therefore reduce sinusoidal overshooting and undershooting of control temperature. A combination of poor thermocouple contact and large insulated (air) pockets often resulted in sub-optimal temperature control in the previous design even after multiple training cycles of the PID controllers.

Testing will include both temperature control from the classic contact thermocouple wire wrapped location and the new center mass thermocouples. Performance will be determined via presence of sinusoidal control noise and how tightly the command temperature matches the lowest point of the sample, measured with a welded touch thermocouple. As of the time of this writing, welding is complete, the monolith needs to be reamed and fit to the longest grips.

Rapid Solidification

The long-term interest for this research is to enable development of materials for additive manufacturing, however without the resources to enable small scale and reasonable cost atomized powder batches, it is not currently possible to assess material viability in the traditional method of single tracks in power, multi-layer density cubes, thin walls, and finally complex geometries. Therefore, through multiple analog methods

this research attempts to determine the failure susceptibility to oxygen and process parameters, as well as non-uniform solidification fronts could make a ternary, quaternary, and more complex SMAs unusable as additive feedstock.

Splat Quenching

Samples for compositions $Ni_{50.3}Ti_{28.7}Hf_{10.5}Zr_{10.5}$, $Ni_{50.3}Ti_{28.7}Hf_{21}$, $Ni_{50.3}Ti_{29.2}Hf_{20.5}$, $Ni_{50.3}Ti_{28.2}Hf_{21.5}$, and $Ni_{50.3}Ti_{27.7}Hf_{22}$ were splat quenched at the University of Alabama at various levels of superheating. Upon receipt at Texas A&M they were mounted using custom fabricated PLA mounts to softly hold the ~45µm splat samples so they could be mounted in slow cure conductive epoxy without impacting the integrity of the sample. $Ni_{50.3}Ti_{28.7}Hf_{10.5}Zr_{10.5}$ and $Ni_{50.3}Ti_{27.7}Hf_{22}$ will be preferentially investigated. The fabricability of $Ni_{50.3}Ti_{29.7}Hf_{20}$ has been highly investigated, however it is of interest to see if increasing Hf content causes h-phase to precipitate out of the matrix during solidification or HfO_2 are present, the latter presenting a significant detriment to the fabrication of these materials. NiTiHfZr is specifically of interest in non-uniform segregation of the alloying elements during solidification, and again, oxide formation.

At the time of this writing, samples are being prepared for BSE imaging which is proving challenging as a combination of the low contrast of martensitic variants in NiTi-based SMAs and the extremely thin nature of the sample. Upon confirmation of SEM results, they will be FIBed and prepared for TEM.

Simulated L-PBF Printability Maps

Testing indicated the most successful materials by all testing metrics were those that were heat treated. In an additive manufacturing context, parts will likely be fabricated from near composition of interest feedstock, ensuring vaporization results in an optimized chemistry profile. Such parameters will also have to lead to high densification. After densification parts will be solution heat treated then aged to promote h-phase formation. Ideally texture control can be manipulated as to optimize for a given device or actuation process, though such control does not currently exist and would require additional knowledge of the effects of directional texture on precipitation kinetics in HTSMAs. In laser powder bed fusion specifically Texas A&M has the capability to develop simulated printability maps to reduce experimental load when determining novel parameter sets. Initial printability maps including criterion for balling, keyholing, and lack of fusion is included in Figure 33. Developed by Sofia Sheikh in Dr. Arroyave's group they take into consideration physical and chemical phenomena associated with each alloy. Of note, $Ni_{50.3}Ti_{29.2}Hf_{20.5}$, $Ni_{50.3}Ti_{28.7}Hf_{21}$, $Ni_{50.3}Ti_{28.2}Hf_{21.5}$, $Ni_{50.3}Ti_{27.7}Hf_{22}$, and $Ni_{50.4}Ti_{27.2}Hf_{22.4}$ appear near identical in zones of printability even though they span a range of Hf content which allows for transformation temperatures to vary by 75°C at 300MPa. If a standardized set of processes could be determined where any variance in Ti/Hf lattice concentration did not affect final densification then the exact desired transformation temperature could be manipulated simply by changing the chemistry of the feedstock with no additional

machine alterations, crucial in an industry where FAA compliance of a process requires no change in machine parameters.

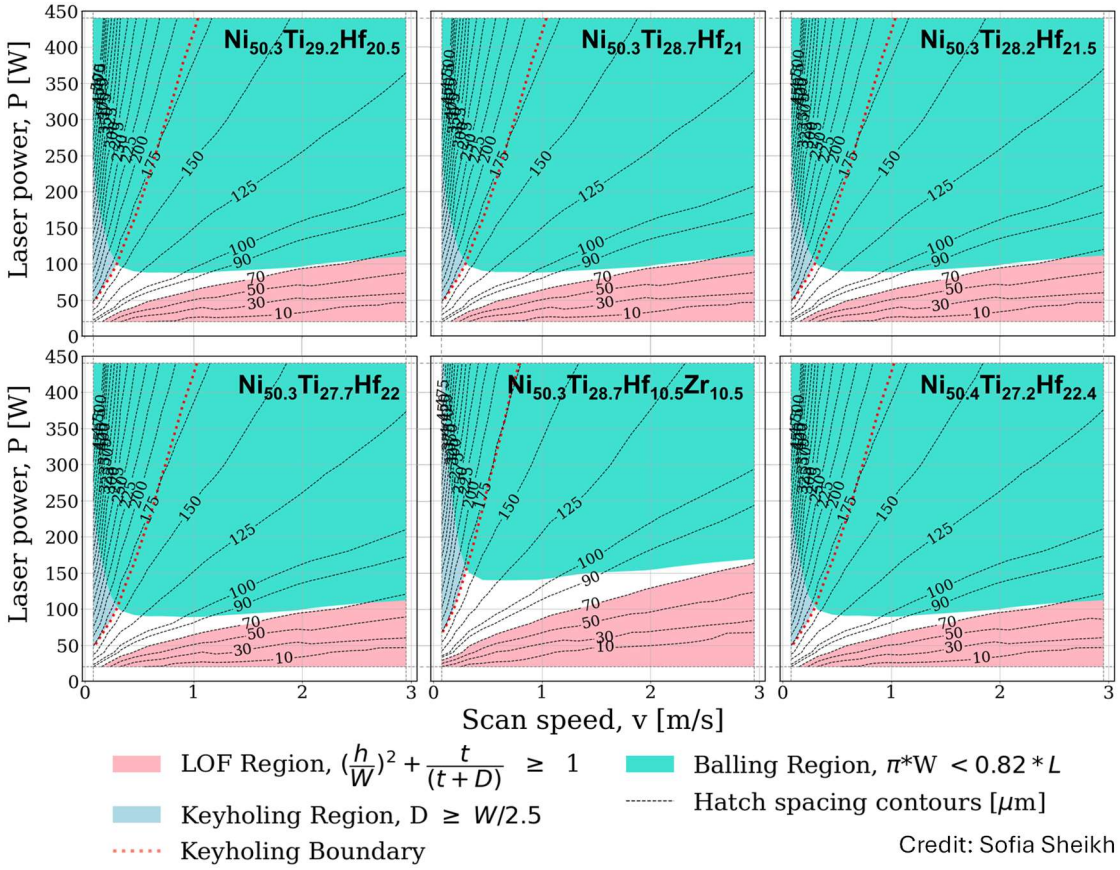

Figure 33: Printability maps for high performance materials as indicated by IBHC

Additionally, the NiTiHfZr composition appears to have a larger operational window than the NiTiHf materials. A quaternary composition has yet to be fabricated by additive manufacturing in the literature, however, if process conditions can be controlled such that conventional challenges to additive are not present, the wider window presents a larger opportunity for variance of VED while maintaining full densification. In this case, not only is the quaternary composition significantly lower cost to procure, but it

also has additional capability to change process parameters in response to localized geometry to avoid non-uniform transformation variation as shown in NiTiHf by Dr. A. Elsayed in the MESAM group. A NiTiHfZr material therefore may be more compliant for serial production allowing for near peer performance, lower cost, and a wider operational window.

CHAPTER IV

CONCLUSIONS AND FUTURE WORK

Conclusions from Current Progress

Based on the current results the first point to note is the guided investigation into a low hysteresis pareto front bounded by temperature was an enormous success. In 2 model iterations, and with less than 150 tested samples, it was possible to develop over 10 novel alloys which met the temperature constraints from the funding agency. In addition, some of these materials have hysteresis values lower than any published data to date. This alone is a significant scientific achievement, but the entire dataset will represent an opportunity to improve modeling in the high temperature shape memory alloy space.

In addition, with scale up and UCFTC testing of materials it becomes apparent that even if compositions can achieve an extremely low hysteresis value, the value of them as solid-state actuating elements hinges on their ease of manufacture. Many single crystal shape memory alloy compositions or novel materials have been created and tested in compression but elements for useful work are tensile or shear loaded. Every composition that has been scaled up has been successfully processed and tested in tension.

Once the performance metrics are finished being measured and put into a format where they can be directly compared there should be additional measurable trends.

Notably, that is above the exciting result of determining a highest performing material from the pareto front, which is also a significant milestone.

It is yet unknown if compositions from this work will exceed that of other published NiTiHf or come close to the theoretical maximums of precipitation alloyed ternary SMAs.

Future Work

The original sponsor development pathway was specifically interested in taking arbitrarily designed material and moving it through the atomization and additive development process. With the cost of powder that became untenable, however, the creative solutions surrounding validation for L-PBF or EB-PBF remains. Fabrication of large slugs that can be EDM sliced to create substrates would enable energy (laser or e-beam) bead and hatch on plate studies to analyze the melt pool characteristics of the material. Custom development of the substrate would also enable rapid turnaround and low cost compared to atomization. Additionally, in-situ monitoring could allow collection of information on the vaporizing radicals for a given alloy, specifically answering questions about the proposed optimum materials like does Ni-richness content affect the vaporization fraction, does Zr or Hf vaporize at greater relative fractions or is it negligible, or dialing in machine vision for a new material. In addition, a rapid investigation on varied nickel contents would allow for stress free transformation temperature information to be gathered giving a ground truth compositional scheme which would not be available using spectroscopy, this would allow rapid analysis of builds with only a DSC as a build artifact.

For splat quenched samples, the solidification microstructure will be compared with literature as well as PBF counterparts. Time permitting, TEM will also be performed on splat quenched parts as it is significantly novel to the literature. Ideally post heat treated samples could also be investigated in TEM to determine the h-phase formation from the 475°C heat treatment which appeared extremely successful across multiple compositions.

Projected future work beyond the scope of what could be accomplished in the author's remaining time at University would be the drive to develop 4-D as built specimens from a proposed material and compare it to a commercially available material conventionally manufactured. It would be optimal to do a design study on a common element and compare efficacy and cost. A high temperature spring for example like those NASA JPL has proposed on it's rovers.

To develop PBF structures a DOE for single tracks will be developed utilizing a combination of parameter space and modeled printability maps then examined under microscopy for features of interest. Depending on available time and resources WDS may be investigated for chemical variation. Chemical variation in solidification has been characterized in analog to transformation temperatures but the author is not aware of a direct measurement in literature on additively manufactured parts. In conjunction with the in-line spectroscopy the radicals could be identified and intensity fractions classified. The ultimate goal being rapid reaction in creating a material to fit a future need and moving to additive manufacturing to minimize lead time, manufacturing and geometry limitations, and simplify supply chains.

Projected Current Work

For the author to graduate in August the final day for defense is June 9th. Author's defense is scheduled for 5/22/2025 with a buffer after to support any requested changes by the committee.

After successful defense, it is the explicit instruction of the committee chair that two first author papers will be submitted to journals before the Author is permitted to leave campus. The first paper will be submitted to Scripta Materialia and contain all information on small scale investigation into transformation temperatures. The second paper will be submitted to Acta Materialia and include the scale up, mechanical processing, UCFTC, heat treatment, and potentially TEM structures of the materials.

Future Research Topics

Based on the immediate findings of this work there are several future pathways for investigation. The most obvious is a continuation of the engineering of a novel HTMSA for additive manufacturing by producing via atomization powdered alloy to confirm the findings of the rapid solidification analog. Beyond this, there is a significant interest in mechanical performance of an additively manufactured part compared to a conventionally fabricated sample, specifically in tension or torsion. The latter is even more interesting because NiTiHf (or other ternary alloys) improved mechanical properties from precipitation alloying should be even more present in shear. Finally,

developing control for geometries in-situ that would allow an as built spring, torque tube, or as-built metasurfaces.

More indirect areas of research and questions to answer are associated with the large variance between theoretical mechanical performance and recovery in polycrystalline or single crystal ternary SMAs and the actual results observed here or in other literature. What is the mechanism that causes an increase in strength via precipitated phases and reduction in residual stress? Is it a function of crystallographic orientation that could be programmed or tuned via processing methods or is it an inherent of the phase? I.e. is it only possible to optimize a NiTiHf material or is there another quarternary or complex alloy not investigated here that improves symmetry even more between the Austenite and Martensite phases. Is there an optimized limit within the NiTi framework, as in, at what point is it saturated and unable to function as a B2-B19' framework? Can it be shifted to B19 where closer to 1 eigenvalues have been found? Finally, what other combinations of alloying elements exist that could improve the austenite martensite symmetry while also increasing their misalignment that do not cost an exorbitant amount, have significant toxicity, or force the material to be so brittle as to be useless outside of a laboratory scale? For the former, in the interest of speed, is there a way to predict unique phase variations when they have not been experimentally validated or confirmed, and rapidly prove or disprove them? Notably when one author proposed a general kinetic equation for SMAs it only applied to the B2 to B19 system and fell apart for NiTiHf/Zr alloys.

For all the questions we answered, and for those we brought into the light; I thank my committee and my mentor Dr. Karaman for helping me become a scientist, not just an engineer.

REFERENCES

[1] J. Ma, I. Karaman, and R. D. Noebe, "High temperature shape memory alloys," (in English), *Int Mater Rev,* vol. 55, no. 5, pp. 257-315, Sep 2010, doi: 10.1179/095066010x12646898728363.

[2] R. Xi *et al.*, "Influence of Nb addition and process parameters on the microstructure and phase transformation behavior of NiTiNb ternary shape memory alloys fabricated by laser powder bed fusion," (in English), *Scripta Materialia,* vol. 222, Jan 1 2023, doi: ARTN 114996 10.1016/j.scriptamat.2022.114996.

[3] C. Haberland, M. Elahinia, J. M. Walker, H. Meier, and J. Frenzel, "On the development of high quality NiTi shape memory and pseudoelastic parts by additive manufacturing," (in English), *Smart Mater Struct,* vol. 23, no. 10, Oct 2014, doi: Artn 104002 10.1088/0964-1726/23/10/104002.

[4] I. Ferretto *et al.*, "Control of microstructure and shape memory properties of a Fe-Mn-Si-based shape memory alloy during laser powder bed fusion," (in English), *Additive Manufacturing Letters,* vol. 3, Dec 2022, doi: ARTN 100091 10.1016/j.addlet.2022.100091.

[5] I. Ferretto, D. Kim, M. Mohri, E. Ghafoori, W. Lee, and C. Leinenbach, "Shape recovery performance of a (V, C)-containing Fe-Mn-Si-Ni-Cr shape memory alloy fabricated by laser powder bed fusion," (in English), *J Mater Res Technol,* vol. 20, pp. 3969-3984, Sep-Oct 2022, doi: 10.1016/j.jmrt.2022.08.143.

[6] D. C. Lagoudas, *Shape memory alloys: modeling and engineering applications*. Springer, 2008.

[7] *Standard Test Method for Mechanical Uniaxial Constant Force Thermal Cycling of Shape Memory Alloys*, Nov. 1, 2017 2017.

[8] C. Williamson, "CHARACTERIZATION OF COMPOSITIONAL VARIATION AND SOLIDIFICATION CONDITION ON RAPID SOLIDIFICATION BEHAVIOR OF BETA STABILIZED TITANIUM " PhD, Department of Engineering The University of Alabama, 2024.

[9] M. Nematollahi *et al.*, "Additive manufacturing of ni-rich nitihf 20: Manufacturability, composition, density, and transformation behavior," *Shape memory and superelasticity,* vol. 5, pp. 113-124, 2019.

[10] S. Liu, B. B. Kappes, B. Amin-ahmadi, O. Benafan, X. Zhang, and A. P. Stebner, "Physics-informed machine learning for composition – process – property design: Shape memory alloy demonstration," *Applied Materials Today,* vol. 22, p. 100898, 2021/03/01/ 2021, doi: https://doi.org/10.1016/j.apmt.2020.100898.

[11] Y. L. Zhang, L. Yang, L. Yu, J. Y. Ma, and J. Liu, "Ni-Ti-Zr ternary alloy with high transition temperature fabricated by laser powder bed fusion," (in English), *J Alloy Compd,* vol. 938, Mar 25 2023, doi: ARTN 168529 10.1016/j.jallcom.2022.168529.

[12] A. Rao, A. R. Srinivasa, and J. N. Reddy, *Design of shape memory alloy (SMA) actuators*. Springer, 2015.

[13] F. T. Calkins, J. H. Mabe, and G. W. Butler, "Boeing's Variable Geometry Chevron: Morphing aerospace structures for jet noise reduction," (in English), *Proc Spie,* vol. 6171, 2006, doi: Artn 61710o 10.1117/12.659664.

[14] J. Mabe, R. Cabell, and G. Butler, "Design and control of a morphing chevron for takeoff and cruise noise reduction," in *11th AIAA/CEAS aeroacoustics conference*, 2005, p. 2889.

[15] S. Thompson, "An overview of nickel–titanium alloys used in dentistry," *International endodontic journal,* vol. 33, no. 4, pp. 297-310, 2000.

[16] G. F. Andreasen and T. B. Hilleman, "An Evaluation of 55 Cobalt Substituted Nitinol Wire for Use in Orthodontics," *The Journal of the American Dental*

Association, vol. 82, no. 6, pp. 1373-1375, 1971/06/01/ 1971, doi: https://doi.org/10.14219/jada.archive.1971.0209.

[17] G. B. Kauffman and I. Mayo, "The Story of Nitinol: The Serendipitous Discovery of the Memory Metal and Its Applications," *The Chemical Educator,* vol. 2, no. 2, pp. 1-21, 1997/06/01 1997, doi: 10.1007/s00897970111a.

[18] B. T. Holschuh and D. J. Newman, "Morphing compression garments for space medicine and extravehicular activity using active materials," *Aerospace medicine and human performance,* vol. 87, no. 2, pp. 84-92, 2016.

[19] A. Elsayed *et al.*, "Active interlocking metasurfaces enabled by shape memory alloys," *Materials & Design,* vol. 244, p. 113137, 2024/08/01/ 2024, doi: https://doi.org/10.1016/j.matdes.2024.113137.

[20] G. Costanza and M. E. Tata, "Shape Memory Alloys for Aerospace, Recent Developments, and New Applications: A Short Review," *Materials,* vol. 13, no. 8, p. 1856, 2020, doi: 10.3390/ma13081856.

[21] R. Granberry, K. Eschen, B. Holschuh, and J. Abel, "Functionally graded knitted actuators with NiTi-based Shape Memory Alloys for topographically self-fitting wearables," *Advanced materials technologies,* vol. 4, no. 11, p. 1900548, 2019.

[22] O. Benafan, M. R. Moholt, M. Bass, J. H. Mabe, D. E. Nicholson, and F. T. Calkins, "Recent Advancements in Rotary Shape Memory Alloy Actuators for Aeronautics," *Shape Memory and Superelasticity,* vol. 5, no. 4, pp. 415-428, 2019/12/01 2019, doi: 10.1007/s40830-019-00260-3.

[23] M. S. Kim *et al.*, "Shape Memory Alloy (SMA) Actuators: The Role of Material, Form, and Scaling Effects," (in English), *Adv Mater,* vol. 35, no. 33, Aug 17 2023, doi: 10.1002/adma.202208517.

[24] J. M. Jani, M. Leary, A. Subic, and M. A. Gibson, "A review of shape memory alloy research, applications and opportunities," (in English), *Materials & Design,* vol. 56, pp. 1078-1113, Apr 2014, doi: 10.1016/j.matdes.2013.11.084.

[25] W. J. Buehler, R. C. Wiley, and J. V. Gilfrich, "Effect of Low-Temperature Phase Changes on Mechanical Properties of Alloys near Composition Tini," (in English), *Journal of Applied Physics,* vol. 34, no. 5, pp. 1475-&, 1963, doi: Doi 10.1063/1.1729603.

[26] K. Otsuka and X. B. Ren, "Recent developments in the research of shape memory alloys," (in English), *Intermetallics,* vol. 7, no. 5, pp. 511-528, May 1999, doi: Doi 10.1016/S0966-9795(98)00070-3.

[27] D. M. Norfleet *et al.*, "Transformation-induced plasticity during pseudoelastic deformation in Ni-Ti microcrystals," (in English), *Acta Materialia,* vol. 57, no. 12, pp. 3549-3561, Jul 2009, doi: 10.1016/j.actamat.2009.04.009.

[28] T. Simon, A. Kröger, C. Somsen, A. Dlouhy, and G. Eggeler, "On the multiplication of dislocations during martensitic transformations in NiTi shape memory alloys," (in English), *Acta Materialia,* vol. 58, no. 5, pp. 1850-1860, Mar 2010, doi: 10.1016/j.actamat.2009.11.028.

[29] A. R. Pelton, G. H. Huang, P. Moine, and R. Sinclair, "Effects of thermal cycling on microstructure and properties in Nitinol," (in English), *Mat Sci Eng a-Struct,* vol. 532, pp. 130-138, Jan 15 2012, doi: 10.1016/j.msea.2011.10.073.

[30] S. W. Robertson, A. R. Pelton, and R. O. Ritchie, "Mechanical fatigue and fracture of Nitinol," (in English), *Int Mater Rev,* vol. 57, no. 1, pp. 1-36, Jan 2012, doi: 10.1179/1743280411y.0000000009.

[31] C. Grossmann, J. Frenzel, V. Sampath, T. Depka, and G. Eggeler, "Elementary Transformation and Deformation Processes and the Cyclic Stability of NiTi and NiTiCu Shape Memory Spring Actuators," (in English), *Metall Mater Trans A,* vol. 40a, no. 11, pp. 2530-2544, Nov 2009, doi: 10.1007/s11661-009-9958-2.

[32] B. Maass, J. Burow, J. Frenzel, and G. Eggeler, "On the influence of crystal defects on the functional stability of NiTi based shape memory alloys," (in English), *Esomat 2009 - 8th European Symposium on Martensitic Transformations,* 2009, doi: ARTN 02022 10.1051/esomat/200902022.

[33] O. Benafan, R. D. Noebe, S. A. Padula, D. W. Brown, S. Vogel, and R. Vaidyanathan, "Thermomechanical cycling of a NiTi shape memory alloy-macroscopic response and microstructural evolution," (in English), *Int J Plasticity,* vol. 56, pp. 99-118, May 2014, doi: 10.1016/j.ijplas.2014.01.006.

[34] S. Miyazaki, Y. Igo, and K. Otsuka, "Effect of Thermal Cycling on the Transformation Temperatures of Ti-Ni Alloys," (in English), *Acta Metallurgica,* vol. 34, no. 10, pp. 2045-2051, Oct 1986, doi: Doi 10.1016/0001-6160(86)90263-4.

[35] K. C. Atli, I. Karaman, R. D. Noebe, G. Bigelow, and D. Gaydosh, "Work production using the two-way shape memory effect in NiTi and a Ni-rich NiTiHf high-temperature shape memory alloy," (in English), *Smart Mater Struct,* vol. 24, no. 12, Dec 2015, doi: Artn 125023
10.1088/0964-1726/24/12/125023.

[36] G. Eggeler, E. Hornbogen, A. Yawny, A. Heckmann, and M. Wagner, "Structural and functional fatigue of NiTi shape memory alloys," (in English), *Mat Sci Eng a-Struct,* vol. 378, no. 1-2, pp. 24-33, Jul 25 2004, doi: 10.1016/j.msea.2003.10.327.

[37] M. Wagner, T. S. Sawaguchi, G. Kausträter, D. Höffken, and G. Eggeler, "Structural fatigue of pseudoelastic NiTi shape memory wires," (in English), *Mat Sci Eng a-Struct,* vol. 378, no. 1-2, pp. 105-109, Jul 25 2004, doi: 10.1016/j.msea.2003.11.058.

[38] Y. Gao, L. Casalena, M. L. Bowers, R. D. Noebe, M. J. Mills, and Y. Wang, "An origin of functional fatigue of shape memory alloys," (in English), *Acta Materialia,* vol. 126, pp. 389-400, Mar 2017, doi: 10.1016/j.actamat.2017.01.001.

[39] B. Kockar, I. Karaman, J. I. Kim, Y. J. Chumlyakov, J. Sharp, and C. J. Yu, "Thermomechanical cyclic response of an ultrafine-grained NiTi shape memory alloy," (in English), *Acta Materialia,* vol. 56, no. 14, pp. 3630-3646, Aug 2008, doi: 10.1016/j.actamat.2008.04.001.

[40] K. Tanaka, F. Nishimura, M. Matsui, H. Tobushi, and P. H. Lin, "Phenomenological analysis of plateaus on stress-strain hysteresis in TiNi shape memory alloy wires," (in English), *Mech Mater,* vol. 24, no. 1, pp. 19-30, Sep 1996, doi: Doi 10.1016/0167-6636(96)00030-0.

[41] K. Tanaka, F. Nishimura, T. Hayashi, H. Tobushi, and C. Lexcellent, "Phenomenological Analysis on Subloops and Cyclic Behavior in Shape-Memory Alloys under Mechanical and or Thermal Loads," (in English), *Mech Mater,* vol. 19, no. 4, pp. 281-292, Feb 1995, doi: Doi 10.1016/0167-6636(94)00038-I.

[42] B. Raniecki, C. Lexcellent, and K. Tanaka, "Thermodynamic models of pseudoelastic behaviour of shape memory alloys," *Archives of Mechanics-Archiwum Mechaniki Stosowanej,* vol. 44, no. 3, pp. 261-284, 1992.

[43] J. G. Boyd and D. C. Lagoudas, "A thermodynamical constitutive model for shape memory materials. Part I. The monolithic shape memory alloy," *Int J Plasticity,* vol. 12, no. 6, pp. 805-842, 1996.

[44] J. G. Boyd and D. C. Lagoudas, "A thermodynamical constitutive model for shape memory materials. Part II. The SMA composite material," *Int J Plasticity,* vol. 12, no. 7, pp. 843-873, 1996.

[45] D. J. Hartl, G. Chatzigeorgiou, and D. C. Lagoudas, "Three-dimensional modeling and numerical analysis of rate-dependent irrecoverable deformation in shape memory alloys," *Int J Plasticity,* vol. 26, no. 10, pp. 1485-1507, 2010.

[46] NASA. "Shape Memory Materials Database (SMMD) Tool." https://shapememory.grc.nasa.gov/ (accessed 2025).

[47] J. Frenzel, A. Wieczorek, I. Opahle, B. Maass, R. Drautz, and G. Eggeler, "On the effect of alloy composition on martensite start temperatures and latent heats in Ni-Ti-based shape memory alloys," (in English), *Acta Materialia,* vol. 90, pp. 213-231, May 15 2015, doi: 10.1016/j.actamat.2015.02.029.

[48] Z. Zhang, R. D. James, and S. Müller, "Energy barriers and hysteresis in martensitic phase transformations," *Acta Materialia,* vol. 57, no. 15, pp. 4332-4352, 2009.

[49] A. Evirgen, I. Karaman, R. Santamarta, J. Pons, C. Hayrettin, and R. Noebe, "Relationship between crystallographic compatibility and thermal hysteresis in Ni-rich NiTiHf and NiTiZr high temperature shape memory alloys," *Acta Materialia,* vol. 121, pp. 374-383, 2016.

[50] A. Evirgen, I. Karaman, R. Santamarta, J. Pons, and R. Noebe, "Microstructural characterization and shape memory characteristics of the Ni50. 3Ti34. 7Hf15 shape memory alloy," *Acta Materialia,* vol. 83, pp. 48-60, 2015.

[51] J. Broucek *et al.*, "Design of high-temperature NiTiCuHf shape memory alloys with minimum thermal hysteresis using Bayesian optimization," *Acta Materialia,* vol. 286, p. 120651, 2025/03/01/ 2025, doi: https://doi.org/10.1016/j.actamat.2024.120651.

[52] O. Benafan, R. Noebe, S. Padula, and R. Vaidyanathan, "Microstructural response during isothermal and isobaric loading of a precipitation-strengthened Ni-29.7 Ti-20Hf high-temperature shape memory alloy," *Metallurgical and materials Transactions A,* vol. 43, pp. 4539-4552, 2012.

[53] O. Karakoc *et al.*, "Role of microstructure on the actuation fatigue performance of Ni-Rich NiTiHf high temperature shape memory alloys," *Acta Materialia,* vol. 175, pp. 107-120, 2019.

[54] F. Yang *et al.*, "Structure analysis of a precipitate phase in an Ni-rich high-temperature NiTiHf shape memory alloy," *Acta Materialia,* vol. 61, no. 9, pp. 3335-3346, 2013.

[55] M. Prasher, D. Sen, J. Bahadur, R. Tewari, and M. Krishnan, "Correlative SANS and TEM investigation on precipitation kinetics of H-phase in Ni50. 3Ti29. 7Hf20 high temperature shape memory alloy," *J Alloy Compd,* vol. 779, pp. 630-642, 2019.

[56] A. Shuitcev *et al.*, "Precipitation and coarsening kinetics of H-phase in NiTiHf high temperature shape memory alloy," *Journal of Materials Science & Technology,* vol. 114, pp. 90-101, 2022.

[57] R. Santamarta *et al.*, "TEM study of structural and microstructural characteristics of a precipitate phase in Ni-rich Ni–Ti–Hf and Ni–Ti–Zr shape memory alloys," *Acta Materialia,* vol. 61, no. 16, pp. 6191-6206, 2013.

[58] E. Kaya and I. Kaya, "Tool wear progression of PCD and PCBN cutting tools in high speed machining of NiTi shape memory alloy under various cutting speeds," (in English), *Diam Relat Mater,* vol. 105, May 2020, doi: ARTN 107810 10.1016/j.diamond.2020.107810.

[59] Y. Kaynak, S. Manchiraju, I. S. Jawahir, and D. Biermann, "Chip formation and phase transformation in orthogonal machining of NiTi shape memory alloy: microstructure-based modelling and experimental validation," (in English), *Cirp Ann-Manuf Techn,* vol. 69, no. 1, pp. 85-88, 2020, doi: 10.1016/j.cirp.2020.04.025.

[60] J. P. Oliveira, N. Schell, N. Zhou, L. Wood, and O. Benafan, "Laser welding of precipitation strengthened Ni-rich NiTiHf high temperature shape memory alloys: Microstructure and mechanical properties," *Materials & Design,* vol. 162, pp. 229-234, 2019/01/15/ 2019, doi: https://doi.org/10.1016/j.matdes.2018.11.053.

[61] Y. Cui *et al.*, "Multi-material additive manufacturing of steel/Al alloy by controlling the liquid/solid interface in laser beam powder bed fusion," *Addit Manuf,* p. 104529, 2024.

[62] K. Safaei, M. Nematollahi, P. Bayati, H. Dabbaghi, O. Benafan, and M. Elahinia, "Torsional behavior and microstructure characterization of additively manufactured NiTi shape memory alloy tubes," (in English), *Eng Struct,* vol. 226, Jan 1 2021, doi: ARTN 111383 10.1016/j.engstruct.2020.111383.

[63] O. Benafan, G. S. Bigelow, and D. A. Scheiman, "Transformation behavior in NiTi-20Hf shape memory alloys – Transformation temperatures and hardness,"

Scripta Materialia, vol. 146, pp. 251-254, 2018/03/15/ 2018, doi: https://doi.org/10.1016/j.scriptamat.2017.11.050.

[64] A. N. Alagha, S. Hussain, and W. Zaki, "Additive manufacturing of shape memory alloys: A review with emphasis on powder bed systems," (in English), *Materials & Design,* vol. 204, Jun 2021, doi: ARTN 109654 10.1016/j.matdes.2021.109654.

[65] E. O. Olakanmi, R. F. Cochrane, and K. W. Dalgarno, "A review on selective laser sintering/melting (SLS/SLM) of aluminium alloy powders: Processing, microstructure, and properties," (in English), *Progress in Materials Science,* vol. 74, pp. 401-477, Oct 2015, doi: 10.1016/j.pmatsci.2015.03.002.

[66] U. S. Bertoli, G. Guss, S. Wu, M. J. Matthews, and J. M. Schoenung, "In-situ characterization of laser-powder interaction and cooling rates through high-speed imaging of powder bed fusion additive manufacturing," *Materials & Design,* vol. 135, pp. 385-396, 2017.

[67] P. A. Hooper, "Melt pool temperature and cooling rates in laser powder bed fusion," *Addit Manuf,* vol. 22, pp. 548-559, 2018/08/01/ 2018, doi: https://doi.org/10.1016/j.addma.2018.05.032.

[68] L. N. Carter, C. Martin, P. J. Withers, and M. M. Attallah, "The influence of the laser scan strategy on grain structure and cracking behaviour in SLM powder-bed fabricated nickel superalloy," *J Alloy Compd,* vol. 615, pp. 338-347, 2014/12/05/ 2014, doi: https://doi.org/10.1016/j.jallcom.2014.06.172.

[69] M. Mahmoudi *et al.*, "On the printability and transformation behavior of nickel-titanium shape memory alloys fabricated using laser powder-bed fusion additive manufacturing," *Journal of Manufacturing Processes,* vol. 35, pp. 672-680, 2018.

[70] K. Safaei, N. T. Andani, M. Nematollahi, O. Benafan, B. Poorganji, and M. Elahinia, "The Build Orientation Dependency of NiTi Shape Memory Alloy Processed by Laser Powder Bed Fusion," *Shape Memory and Superelasticity,* vol. 8, no. 4, pp. 265-276, 2022.

[71] M. Nematollahi *et al.*, "Building orientation-structure-property in laser powder bed fusion of NiTi shape memory alloy," *J Alloy Compd,* vol. 873, p. 159791, 2021/08/25/ 2021, doi: https://doi.org/10.1016/j.jallcom.2021.159791.

[72] C. Zhang *et al.*, "Processing parameters and martensitic phase transformation relationships in near defect-free additively manufactured NiTiHf high temperature shape memory alloys," (in English), *Materials & Design,* vol. 222, Oct 2022, doi: ARTN 110988 10.1016/j.matdes.2022.110988.

[73] M. Y. Sun *et al.*, "Transformation Behavior and Shape Memory Effect of Ni47Ti44Nb9 Alloy Synthesized by Laser Powder Bed Fusion and Heat Treating," (in English), *Metals,* vol. 12, no. 9, Sep 2022, doi: ARTN 1438 10.3390/met12091438.

[74] M. R. da Silva *et al.*, "Laser surface remelting of a Cu-Al-Ni-Mn shape memory alloy," *Materials Science and Engineering: A,* vol. 661, pp. 61-67, 2016/04/20/ 2016, doi: https://doi.org/10.1016/j.msea.2016.03.021.

[75] X. Y. Xi, J. T. Zhang, H. Tang, Y. Cao, and Z. Y. Xiao, "The ultrahigh functional response of CuAlMnNb shape memory alloy by selective laser melting," (in English), *J Mater Res Technol,* vol. 20, pp. 671-680, Sep-Oct 2022, doi: 10.1016/j.jmrt.2022.07.091.

[76] S. Singh *et al.*, "Development of Cu-based shape memory alloy through selective laser melting from elemental powder mixture: Processing and characterization," (in English), *J Alloy Compd,* vol. 961, Oct 25 2023, doi: ARTN 171029 10.1016/j.jallcom.2023.171029.

[77] G. R. Donoso, M. Walczak, E. R. Moore, and J. A. Ramos-Grez, "Towards direct metal laser fabrication of Cu-based shape memory alloys," (in English), *Rapid Prototyping Journal,* vol. 23, no. 2, pp. 329-336, 2017, doi: 10.1108/Rpj-02-2016-0017.

[78] P. Gargarella *et al.*, "Phase Formation, Thermal Stability and Mechanical Properties of a Cu-Al-Ni-Mn Shape Memory Alloy Prepared by Selective Laser

Melting," (in English), *Mater Res-Ibero-Am J,* vol. 18, pp. 35-38, Dec 2015, doi: 10.1590/1516-1439.338914.

[79] J. Tian *et al.*, "Process optimization, microstructures and mechanical properties of a Cu-based shape memory alloy fabricated by selective laser melting," (in English), *J Alloy Compd,* vol. 785, pp. 754-764, May 15 2019, doi: 10.1016/j.jallcom.2019.01.153.

[80] N. Babacan, S. Pauly, and T. Gustmann, "Laser powder bed fusion of a superelastic Cu-Al-Mn shape memory alloy," (in English), *Materials & Design,* vol. 203, May 2021, doi: ARTN 109625 10.1016/j.matdes.2021.109625.

[81] D. Abolhasani, S. W. Han, C. J. VanTyne, N. Kang, and Y. H. Moon, "Enhancing the shape memory effect of Cu-Al-Ni alloys via partial reinforcement by alumina through selective laser melting," (in English), *J Mater Res Technol,* vol. 15, pp. 4032-4047, Nov-Dec 2021, doi: 10.1016/j.jmrt.2021.10.040.

[82] A. Cladera, B. Weber, C. Leinenbach, C. Czaderski, M. Shahverdi, and M. Motavalli, "Iron-based shape memory alloys for civil engineering structures: An overview," (in English), *Constr Build Mater,* vol. 63, pp. 281-293, Jul 30 2014, doi: 10.1016/j.conbuildmat.2014.04.032.

[83] Z. X. Zhang, J. Zhang, H. L. Wu, Y. Z. Ji, and D. D. Kumar, "Iron-Based Shape Memory Alloys in Construction: Research, Applications and Opportunities," (in English), *Materials,* vol. 15, no. 5, Mar 2022, doi: ARTN 1723 10.3390/ma15051723.

[84] I. Ferretto, D. Kim, N. M. Della Ventura, M. Shahverdi, W. Lee, and C. Leinenbach, "Laser powder bed fusion of a Fe-Mn-Si shape memory alloy," (in English), *Addit Manuf,* vol. 46, Oct 2021, doi: ARTN 102071 10.1016/j.addma.2021.102071.

[85] D. Kim, I. Ferretto, C. Leinenbach, and W. Lee, "3D and 4D Printing of Complex Structures of Fe-Mn-Si-Based Shape Memory Alloy Using Laser

Powder Bed Fusion," (in English), *Adv Mater Interfaces,* vol. 9, no. 13, May 2022, doi: ARTN 2200171
10.1002/admi.202200171.

[86] D. Kim, I. Ferretto, C. Leinenbach, W. Lee, and W. Kim, "Effect of direct aging on microstructure, mechanical properties and shape memory behavior of Fe-17Mn-5Si-10Cr-4Ni-(V, C) shape memory alloy fabricated by laser powder bed fusion," (in English), *Materials Characterization,* vol. 197, Mar 2023, doi: ARTN 112705
10.1016/j.matchar.2023.112705.

[87] D. Kim, I. Ferretto, J. B. Jeon, C. Leinenbach, and W. Lee, "Formation of metastable bcc-delta phase and its transformation to fcc- in laser powder bed fusion of Fe-Mn-Si shape memory alloy," (in English), *J Mater Res Technol,* vol. 14, pp. 2782-2788, Sep-Oct 2021, doi: 10.1016/j.jmrt.2021.08.119.

[88] F. C. Ewald, F. Brenne, T. Gustmann, M. Vollmer, P. Krooss, and T. Niendorf, "Laser Powder Bed Fusion Processing of Fe-Mn-Al-Ni Shape Memory Alloy-On the Effect of Elevated Platform Temperatures," (in English), *Metals,* vol. 11, no. 2, Feb 2021, doi: ARTN 185
10.3390/met11020185.

[89] M. P. Caputo, A. E. Berkowitz, A. Armstrong, P. Mullner, and C. V. Solomon, "4D printing of net shape parts made from Ni-Mn-Ga magnetic shape-memory alloys," (in English), *Addit Manuf,* vol. 21, pp. 579-588, May 2018, doi: 10.1016/j.addma.2018.03.028.

[90] M. P. Caputo and C. V. Solomon, "A facile method for producing porous parts with complex geometries from ferromagnetic Ni-Mn-Ga shape memory alloys," (in English), *Mater Lett,* vol. 200, pp. 87-89, Aug 1 2017, doi: 10.1016/j.matlet.2017.04.112.

[91] M. P. Caputo, D. R. Waryoba, and C. V. Solomon, "Sintering effects on additive manufactured Ni-Mn-Ga shape memory alloys: a microstructure and thermal analysis," (in English), *Journal of Materials Science,* vol. 55, no. 12, pp. 5311-5321, Apr 2020, doi: 10.1007/s10853-020-04352-9.

[92] A. Acierno *et al.*, "Characterizing Changes in Grain Growth, Mechanical Properties, and Transformation Properties in Differently Sintered and Annealed Binder-Jet 3D Printed 14M Ni-Mn-Ga Magnetic Shape Memory Alloys," (in English), *Metals,* vol. 12, no. 5, May 2022, doi: ARTN 724 10.3390/met12050724.

[93] A. Mostafaei *et al.*, "Microstructural evolution and magnetic properties of binder jet additive manufactured Ni-Mn-Ga magnetic shape memory alloy foam," (in English), *Acta Materialia,* vol. 131, pp. 482-490, Jun 1 2017, doi: 10.1016/j.actamat.2017.04.010.

[94] A. Mostafaei, P. R. De Vecchis, E. L. Stevens, and M. Chmielus, "Sintering regimes and resulting microstructure and properties of binder jet 3D printed Ni-Mn-Ga magnetic shape memory alloys," (in English), *Acta Materialia,* vol. 154, pp. 355-364, Aug 1 2018, doi: 10.1016/j.actamat.2018.05.047.

[95] V. Laitinen, A. Sozinov, A. Saren, M. Chmielus, and K. Ullakko, "Characterization of as-built and heat-treated Ni-Mn-Ga magnetic shape memory alloy manufactured via laser powder bed fusion," (in English), *Addit Manuf,* vol. 39, Mar 2021, doi: ARTN 101854 10.1016/j.addma.2021.101854.

[96] M. Namvari, V. Laitinen, A. Sozinov, A. Saren, and K. Ullakko, "Effects of 1 at.% additions of Co, Fe, Cu, and Cr on the properties of Ni-Mn-Ga-based magnetic shape memory alloys," (in English), *Scripta Materialia,* vol. 224, Feb 2023, doi: ARTN 115116 10.1016/j.scriptamat.2022.115116.

[97] V. Laitinen, A. Salminen, and K. Ullakko, "First investigation on processing parameters for laser powder bed fusion of Ni-Mn-Ga magnetic shape memory alloy," (in English), *J Laser Appl,* vol. 31, no. 2, May 2019, doi: Artn 022303 10.2351/1.5096108.

[98] V. Laitinen, A. Saren, A. Sozinov, and K. Ullakko, "Giant 5.8% magnetic-field-induced strain in additive manufactured Ni-Mn-Ga magnetic shape memory alloy," (in English), *Scripta Materialia,* vol. 208, Feb 1 2022, doi: ARTN 114324 10.1016/j.scriptamat.2021.114324.

[99] A. Milleret, V. Laitinen, K. Ullakko, N. Fenineche, and M. M. Attallah, "Laser powder bed fusion of (14 M) Ni-Mn-Ga magnetic shape memory alloy lattices," (in English), *Addit Manuf,* vol. 60, Dec 2022, doi: ARTN 103231 10.1016/j.addma.2022.103231.

[100] V. Laitinen, A. Sozinov, A. Saren, A. Salminen, and K. Ullakko, "Laser powder bed fusion of Ni-Mn-Ga magnetic shape memory alloy," (in English), *Addit Manuf,* vol. 30, Dec 2019, doi: ARTN 100891 10.1016/j.addma.2019.100891.

[101] A. Saren, V. Laitinen, M. Vinogradova, and K. Ullakko, "Twin boundary mobility in additive manufactured magnetic shape memory alloy 10M Ni-Mn-Ga," (in English), *Acta Materialia,* vol. 246, Mar 1 2023, doi: ARTN 118666 10.1016/j.actamat.2022.118666.

[102] H. H. He, G. X. Chen, and C. Y. C. Chen, "Machine learning and graph neural network for finding potential drugs related to multiple myeloma," (in English), *New J Chem,* vol. 46, no. 11, pp. 5188-5200, Mar 14 2022, doi: 10.1039/d1nj04935f.

[103] C. Chen, W. K. Ye, Y. X. Zuo, C. Zheng, and S. P. Ong, "Graph Networks as a Universal Machine Learning Framework for Molecules and Crystals," (in English), *Chem Mater,* vol. 31, no. 9, pp. 3564-3572, May 14 2019, doi: 10.1021/acs.chemmater.9b01294.

[104] J. Schmidt, M. R. G. Marques, S. Botti, and M. A. L. Marques, "Recent advances and applications of machine learning in solid-state materials science," (in English), *Npj Comput Mater,* vol. 5, Aug 8 2019, doi: ARTN 83 10.1038/s41524-019-0221-0.

[105] T. Xie and J. C. Grossman, "Crystal Graph Convolutional Neural Networks for an Accurate and Interpretable Prediction of Material Properties," (in English), *Phys Rev Lett,* vol. 120, no. 14, Apr 6 2018, doi: ARTN 145301 10.1103/PhysRevLett.120.145301.

[106] S. M. Moosavi, K. M. Jablonka, and B. Smit, "The Role of Machine Learning in the Understanding and Design of Materials," (in English), *J Am Chem Soc,* vol. 142, no. 48, pp. 20273-20287, Dec 2 2020, doi: 10.1021/jacs.0c09105.

[107] Z. P. Yao *et al.*, "Inverse design of nanoporous crystalline reticular materials with deep generative models," (in English), *Nat Mach Intell,* vol. 3, no. 1, pp. 76-86, Jan 2021, doi: 10.1038/s42256-020-00271-1.

[108] K. T. Butler, D. W. Davies, H. Cartwright, O. Isayev, and A. Walsh, "Machine learning for molecular and materials science," (in English), *Nature,* vol. 559, no. 7715, pp. 547-555, Jul 26 2018, doi: 10.1038/s41586-018-0337-2.

[109] A. Y. T. Wang *et al.*, "Machine Learning for Materials Scientists: An Introductory Guide toward Best Practices," (in English), *Chem Mater,* vol. 32, no. 12, pp. 4954-4965, Jun 23 2020, doi: 10.1021/acs.chemmater.0c01907.

[110] R. Hmede, F. Chapelle, and Y. Lapusta, "Review of Neural Network Modeling of Shape Memory Alloys," (in English), *Sensors-Basel,* vol. 22, no. 15, Aug 2022, doi: ARTN 5610
10.3390/s22155610.

[111] C. O. Kaan Divringi, "Advanced Shape Memory Alloy Material Models for ANSYS ", 2016. [Online]. Available: https://www.ozeninc.com/wp-content/uploads/2016/01/Advanced-Shape-Memory-Alloy-Material-Models-for-ANSYS.pdf

[112] W. Trehern, R. Ortiz-Ayala, K. C. Atli, R. Arroyave, and I. Karaman, "Data-driven shape memory alloy discovery using Artificial Intelligence Materials Selection (AIMS) framework," (in English), *Acta Materialia,* vol. 228, Apr 15 2022, doi: ARTN 117751
10.1016/j.actamat.2022.117751.

[113] A. Solomou *et al.*, "Multi-objective Bayesian materials discovery: Application on the discovery of precipitation strengthened NiTi shape memory alloys through micromechanical modeling," (in English), *Materials & Design,* vol. 160, pp. 810-827, Dec 15 2018, doi: 10.1016/j.matdes.2018.10.014.

[114] U. M. H. U. Kankanamge, J. Reiner, X. J. Ma, S. C. Gallo, and W. Xu, "Machine learning guided alloy design of high-temperature NiTiHf shape memory alloys," (in English), *Journal of Materials Science,* vol. 57, no. 41, pp. 19447-19465, Nov 2022, doi: 10.1007/s10853-022-07793-6.

[115] X. P. Zhao, H. Y. Huang, C. Wen, Y. J. Su, and P. Qian, "Accelerating the development of multi-component Cu-Al-based shape memory alloys with high elastocaloric property by machine learning," (in English), *Comp Mater Sci,* vol. 176, Apr 15 2020, doi: ARTN 109521
10.1016/j.commatsci.2020.109521.

[116] A. A. Catal, E. Bedir, R. Yilmaz, and D. Canadinc, "Design of a NiTiHf shape memory alloy with an austenite finish temperature beyond 400? utilizing artificial intelligence," (in English), *J Alloy Compd,* vol. 904, May 25 2022, doi: ARTN 164135
10.1016/j.jallcom.2022.164135.

[117] D. Z. Xue, P. V. Balachandran, J. Hogden, J. Theiler, D. Q. Xue, and T. Lookman, "Accelerated search for materials with targeted properties by adaptive design," (in English), *Nat Commun,* vol. 7, Apr 2016, doi: ARTN 11241
10.1038/ncomms11241.

[118] S. H. Zadeh *et al.*, "An interpretable boosting-based predictive model for transformation temperatures of shape memory alloys," (in English), *Comp Mater Sci,* vol. 226, Jun 25 2023, doi: ARTN 112225
10.1016/j.commatsci.2023.112225.

[119] O. A. Mohamed, S. H. Masood, and W. Xu, "Nickel-titanium shape memory alloys made by selective laser melting: a review on process optimisation," (in English), *Adv Manuf,* vol. 10, no. 1, pp. 24-58, Mar 2022, doi: 10.1007/s40436-021-00376-9.

[120] L. Xue *et al.*, "Controlling martensitic transformation characteristics in defect-free NiTi shape memory alloys fabricated using laser powder bed fusion and a process optimization framework," (in English), *Acta Materialia,* vol. 215, Aug 15 2021, doi: ARTN 117017
10.1016/j.actamat.2021.117017.

[121] G. T. Li, T. Y. Yu, P. Wu, and M. J. Chen, "Molecular Dynamics Simulation of NiTi Shape Memory Alloys Produced by Laser Powder Bed Fusion: Laser Parameters on Phase Transformation Behavior," (in English), *Materials,* vol. 16, no. 1, Jan 2023, doi: ARTN 409
10.3390/ma16010409.

[122] M. Mehrpouya, A. Gisario, M. Nematollahi, A. Rahimzadeh, K. S. Baghbaderani, and M. Elahinia, "The prediction model for additively manufacturing of NiTiHf high-temperature shape memory alloy," (in English), *Mater Today Commun,* vol. 26, Mar 2021, doi: ARTN 102022
10.1016/j.mtcomm.2021.102022.

[123] J. N. Zhu *et al.*, "Controlling microstructure evolution and phase transformation behavior in additive manufacturing of nitinol shape memory alloys by tuning hatch distance," (in English), *Journal of Materials Science,* vol. 57, no. 10, pp. 6066-6084, Mar 2022, doi: 10.1007/s10853-022-07007-z.

[124] Y. Hu *et al.*, "Multi-physics modeling for laser powder bed fusion process of NiTi shape memory alloy," *J Alloy Compd,* vol. 954, p. 170207, 2023/09/05/ 2023, doi: https://doi.org/10.1016/j.jallcom.2023.170207.

[125] P. Fernandez-Zelaia, M. M. Kirka, S. N. Dryepondt, and M. N. Gussev, "Crystallographic texture control in electron beam additive manufacturing via conductive manipulation," *Materials & Design,* vol. 195, p. 109010, 2020/10/01/ 2020, doi: https://doi.org/10.1016/j.matdes.2020.109010.

[126] S. Z. Uddin, L. E. Murr, C. A. Terrazas, P. Morton, D. A. Roberson, and R. B. Wicker, "Processing and characterization of crack-free aluminum 6061 using high-temperature heating in laser powder bed fusion additive manufacturing," *Addit Manuf,* vol. 22, pp. 405-415, 2018/08/01/ 2018, doi: https://doi.org/10.1016/j.addma.2018.05.047.

[127] C. J. Williamson, "Characterization of Compositional Variation and Solidification Condition on Rapid Solidification Behavior of Beta Stabilized Titanium," Ph.D., The University of Alabama, United States -- Alabama, 31335243, 2024. [Online]. Available: http://proxy.library.tamu.edu/login?url=https://www.proquest.com/dissertations-

theses/characterization-compositional-variation/docview/3102311341/se-2?accountid=7082
https://linkresolver.tamu.edu/tamu?url_ver=Z39.88-2004&rft_val_fmt=info:ofi/fmt:kev:mtx:dissertation&genre=dissertations&sid=ProQ:ProQuest+Dissertations+%26+Theses+Global&atitle=&title=Characterization+of+Compositional+Variation+and+Solidification+Condition+on+Rapid+Solidification+Behavior+of+Beta+Stabilized+Titanium&issn=&date=2024-01-01&volume=&issue=&spage=&au=Williamson%2C+Christopher+J.&isbn=9798384072560&jtitle=&btitle=&rft_id=info:eric/&rft_id=info:doi/

[128] Z. A. Hasenbusch, A. Deal, B. Brown, D. Wilson, L. Nastac, and L. N. Brewer, "A Comparison of Solidification Structures and Submicroscale Cellular Segregation in Rapidly Solidified Stainless Steels Produced via Two-Piston Splat Quenching and Laser Powder Bed Fusion," *Microscopy and Microanalysis,* vol. 29, no. 4, pp. 1328-1349, 2023, doi: 10.1093/micmic/ozad065.

[129] Z. A. Hasenbusch *et al.*, "Investigation of the Effect of Chrome and Nickel Concentrations During Two-Piston Splat Quenching of Austenitic Stainless Steels," *Metallurgical and Materials Transactions A,* vol. 54, no. 11, pp. 4253-4271, 2023/11/01 2023, doi: 10.1007/s11661-023-07160-3.

[130] Z. A. Hasenbusch, A. Deal, B. Brown, L. Nastac, and L. N. Brewer, "Microstructural and Nanostructural Evolution in Splat Quenched Stainless Steels," *Microscopy and Microanalysis,* vol. 29, no. Supplement_1, pp. 1426-1427, 2023, doi: 10.1093/micmic/ozad067.733.

[131] Z. A. Hasenbusch, "Use of Two-Piston Splat Quenching to Investigate and Characterize the Impact of Compositional Variations on Rapid Solidification Microstructures and Sub-Microscale Features in Stainless Steel Alloys," Ph.D., The University of Alabama, United States -- Alabama, 29254075, 2022. [Online]. Available: http://proxy.library.tamu.edu/login?url=https://www.proquest.com/dissertations-theses/use-two-piston-splat-quenching-investigate/docview/2728138981/se-2?accountid=7082
https://linkresolver.tamu.edu/tamu?url_ver=Z39.88-2004&rft_val_fmt=info:ofi/fmt:kev:mtx:dissertation&genre=dissertations&sid=ProQ:ProQuest+Dissertations+%26+Theses+Global&atitle=&title=Use+of+Two-Piston+Splat+Quenching+to+Investigate+and+Characterize+the+Impact+of+Compositional+Variations+on+Rapid+Solidification+Microstructures+and+Sub-Microscale+Features+in+Stainless+Steel+Alloys&issn=&date=2022-01-

01&volume=&issue=&spage=&au=Hasenbusch%2C+Zachary+Arthur&isbn=9798351447308&jtitle=&btitle=&rft_id=info:eric/&rft_id=info:doi/

[132] *Standard Test Method for Transformation Temperature of Nickel-Titanium Alloys by Thermal Analysis*, ASTM, West Conshohocken, PA, USA, 2017.

[133] J. Frenzel, E. P. George, A. Dlouhy, C. Somsen, M. F. X. Wagner, and G. Eggeler, "Influence of Ni on martensitic phase transformations in NiTi shape memory alloys," (in English), *Acta Materialia,* vol. 58, no. 9, pp. 3444-3458, May 2010, doi: 10.1016/j.actamat.2010.02.019.

APPENDIX A

MECHANICAL PERFORMANCE RESULTS

For purposes of the currently un-published nature of the work; compiled results noted in the paper are not included here in full. In the full submitted defense they will be included as a supplementary file.

APPENDIX B

HEAT TREATMENT ANALYSIS

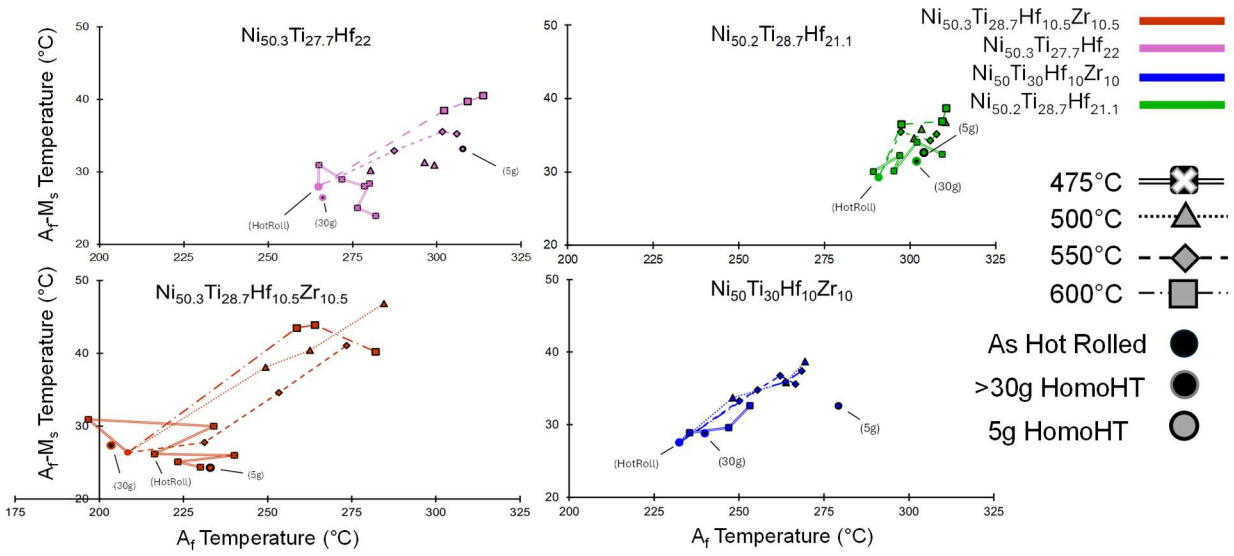

Figure 35: Hysteresis dependence on austenite finish temperature across heat treatment space

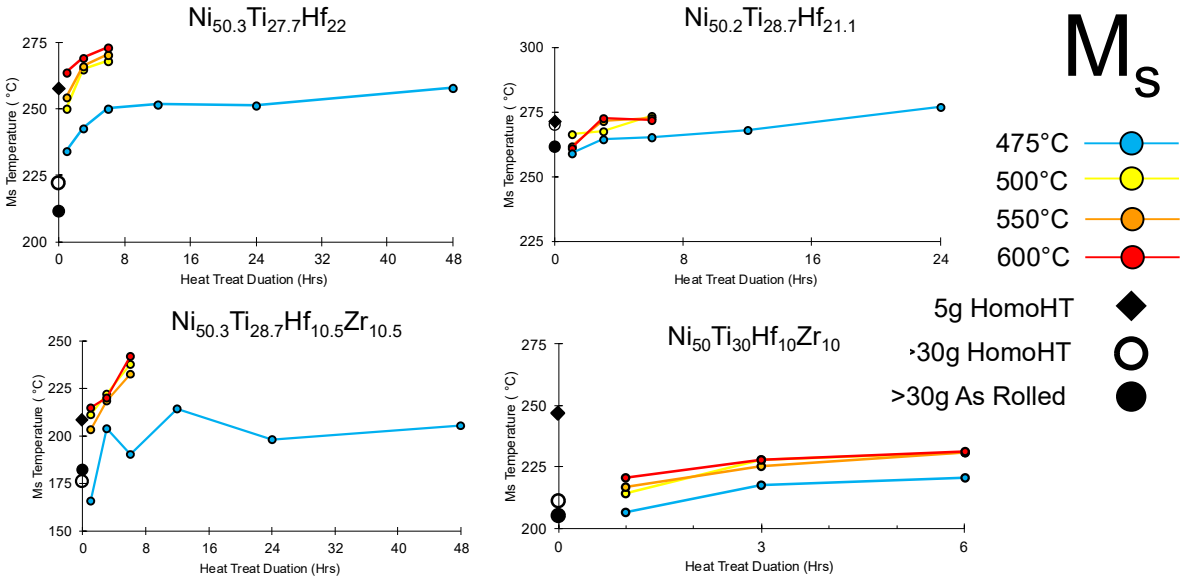

Figure 34: M_s temperature evolution, heat treatment temperature and duration

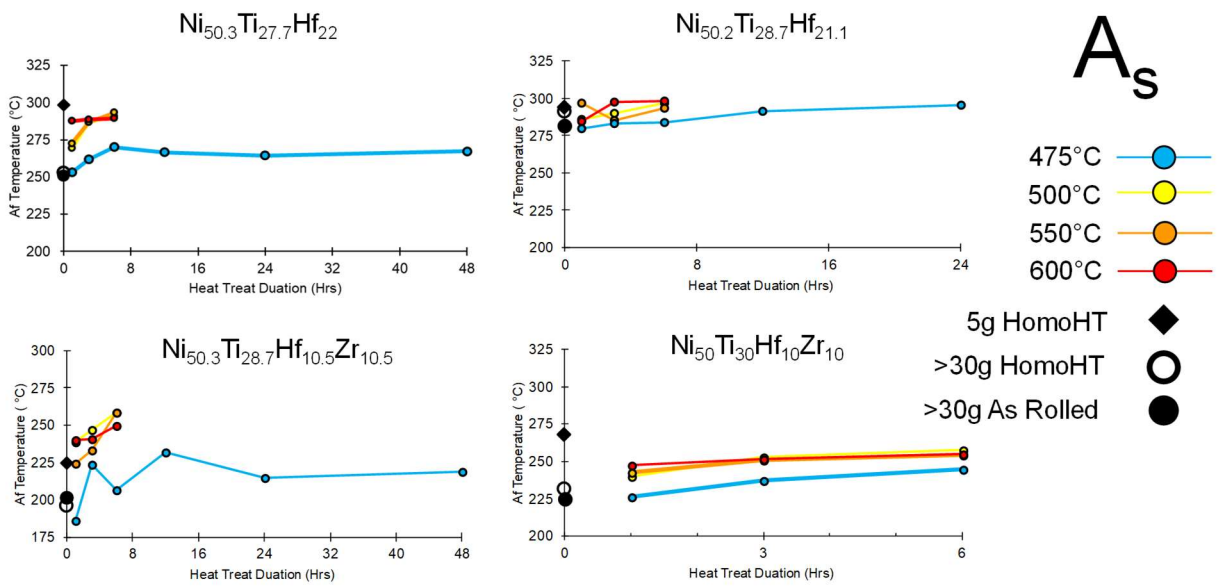

Figure 37: A_s temperature evolution, heat treatment temperature and duration

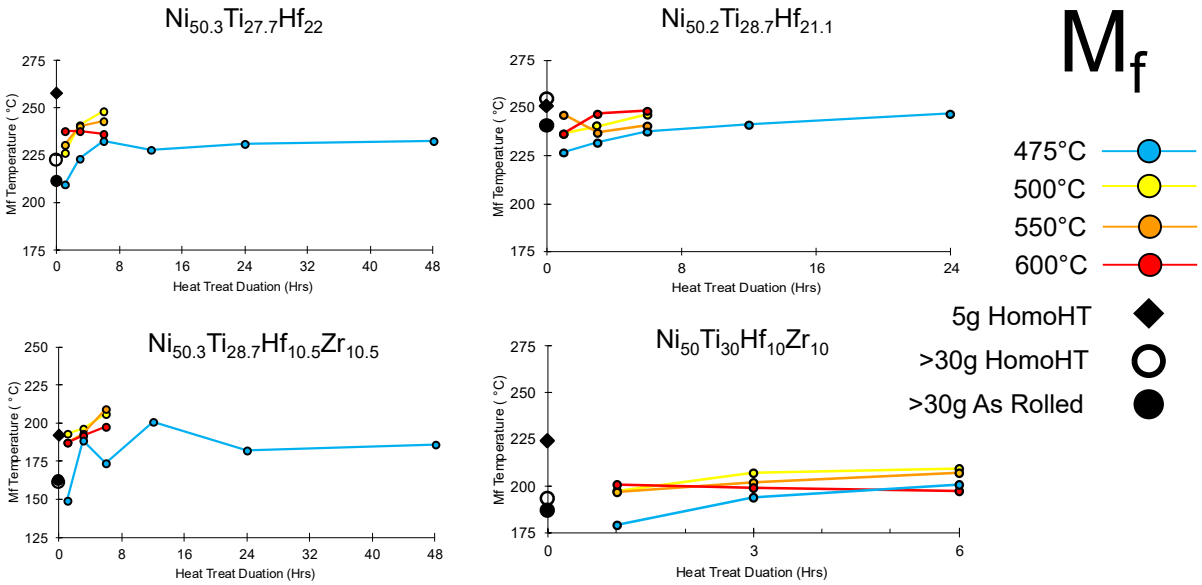

Figure 36: M_f temperature evolution, heat treatment temperature and duration

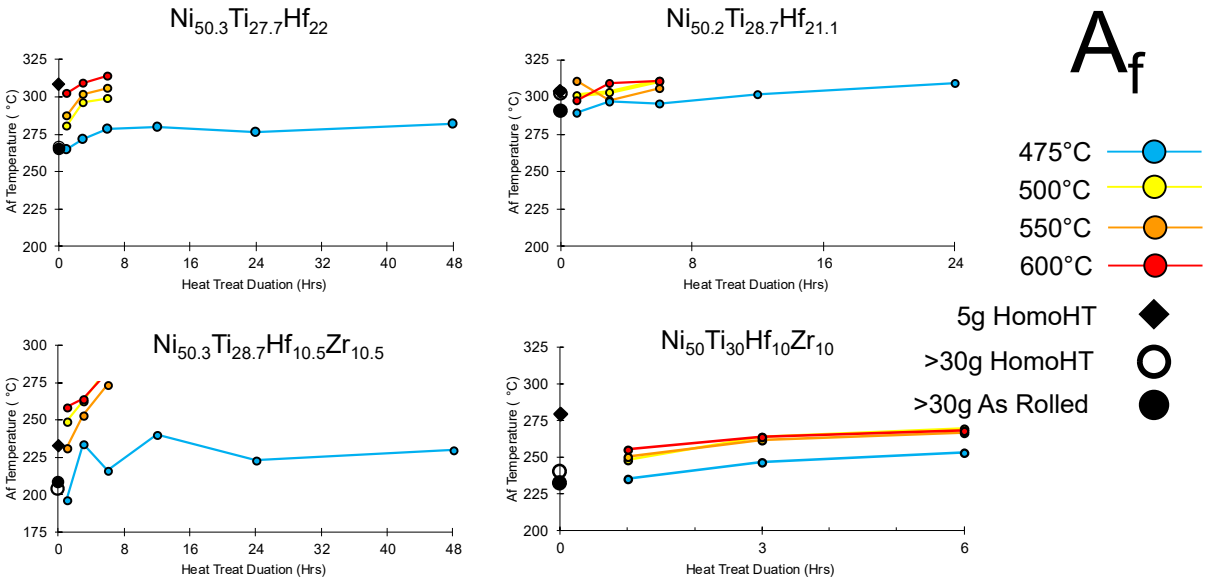

Figure 39: A_f temperature evolution, heat treatment temperature and duration

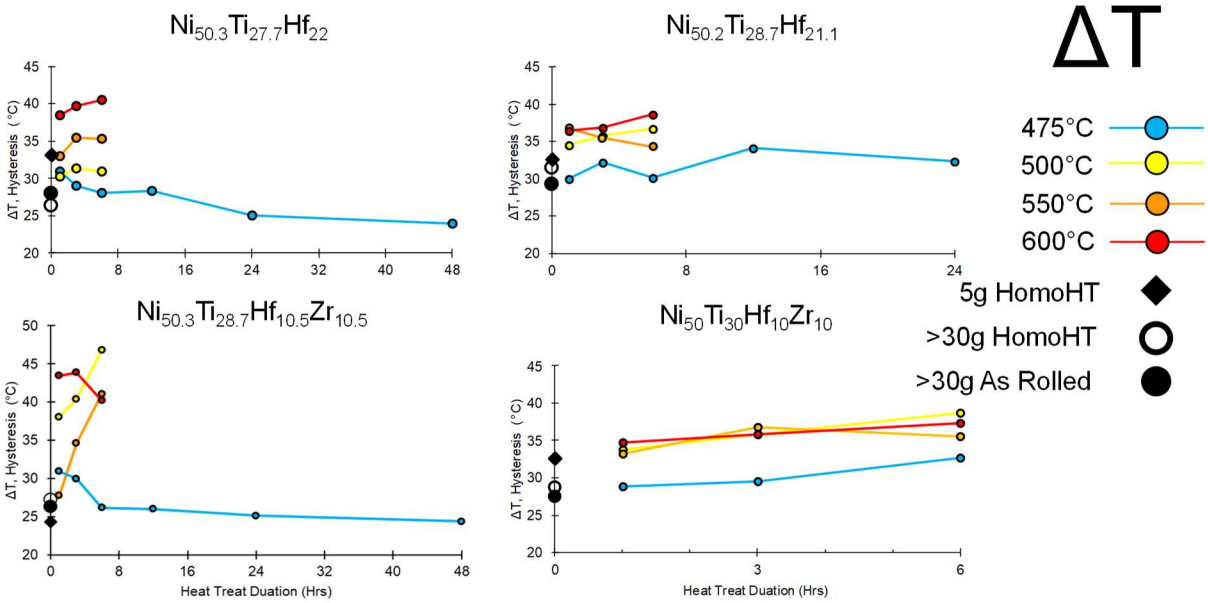

Figure 38: Hysteresis temperature evolution, heat treatment temperature and duration

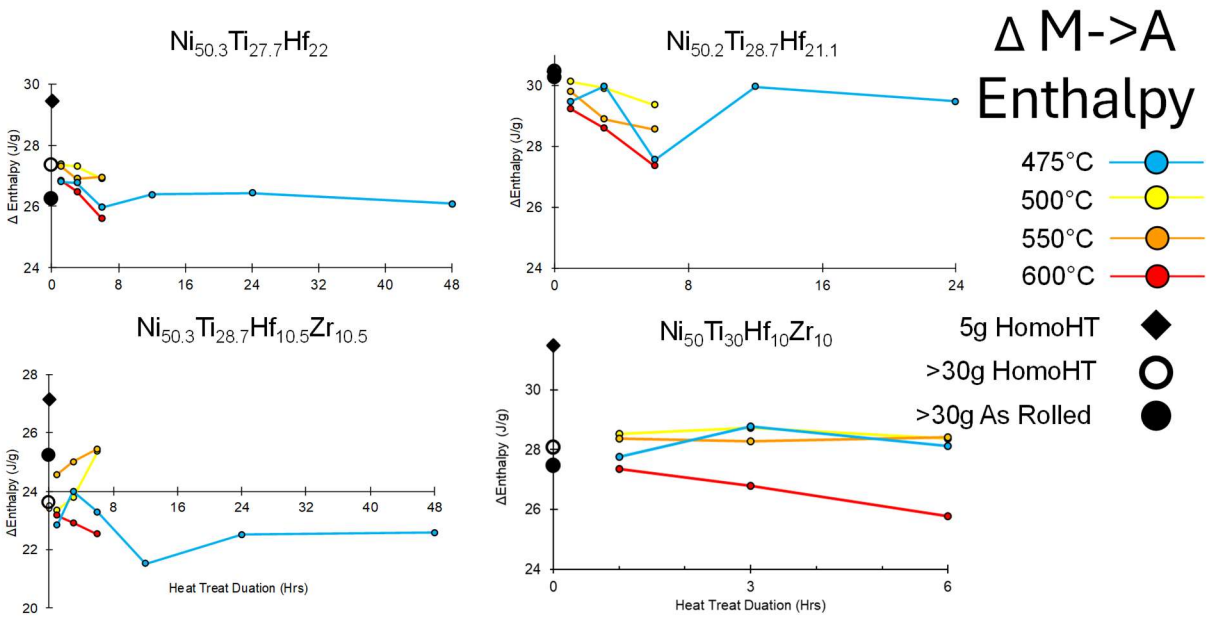

Figure 41: Martensite to austenite enthalpy variation, heat treatment temperature and duration

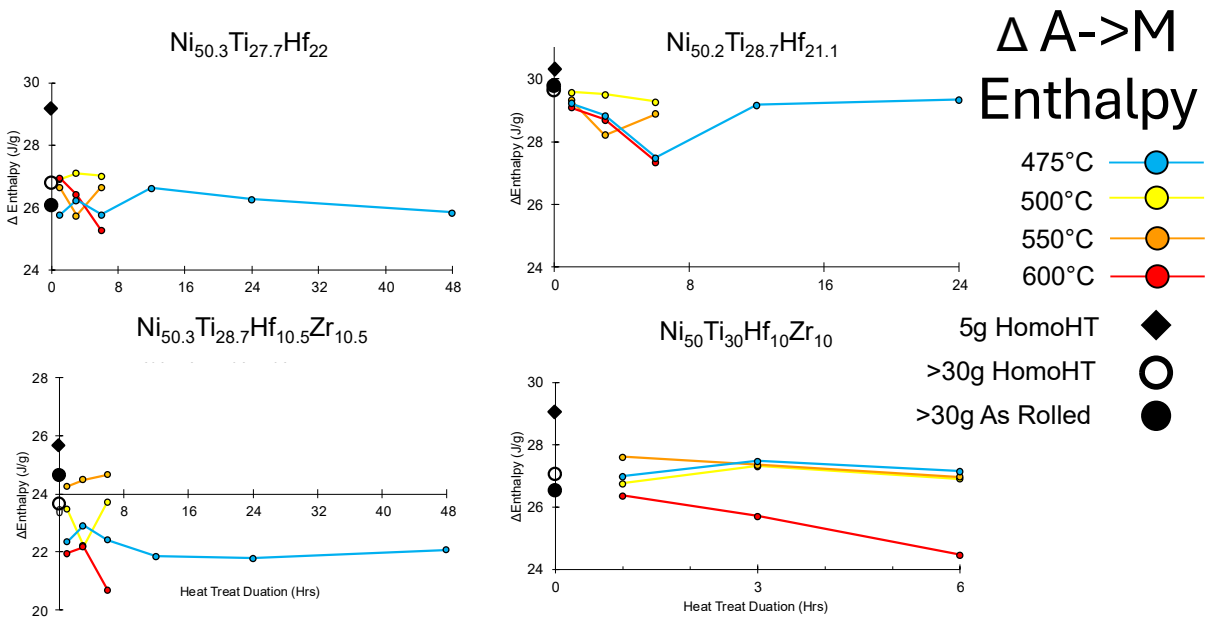

Figure 40: Austenite to martensite enthalpy variation, heat treatment temperature and duration

APPENDIX C

ML PREDICTION AND I1/I2 DATA TABLES

For purposes of the currently un-published nature of the work; compiled results noted in the paper are not included here in full. In the full submitted defense they will be included as a supplementary file.